DEVELOPMENT OF AN INTERFEROMETRIC TECHNIQUE FOR MEASURING THE PROFILES OF THIN LIQUID FILMS

A THESIS SUBMITTED TO
THE GRADUATE SCHOOL OF NATURAL AND APPLIED SCIENCES
OF
MIDDLE EAST TECHNICAL UNIVERSITY

BY

YİĞİT ATA AĞARTAN

IN PARTIAL FULFILLMENT OF THE REQUIREMENTS
FOR
THE DEGREE OF DOCTOR OF PHILOSOPHY
IN
MECHANICAL ENGINEERING

MARCH 2024

Approval of the thesis:

DEVELOPMENT OF AN INTERFEROMETRIC TECHNIQUE FOR MEASURING THE PROFILES OF THIN LIQUID FILMS

submitted by **YİĞİT ATA AĞARTAN** in partial fulfillment of the requirements for the degree of **Doctor of Philosophy in Mechanical Engineering Department, Middle East Technical University** by,

Prof. Dr. Halil Kalıpçılar
Dean, Graduate School of **Natural and Applied Sciences** _____

Prof. Dr. M. A. Sahir Arıkan
Head of Department, **Mechanical Engineering** _____

Prof. Dr. Zafer Dursunkaya
Supervisor, **Mechanical Engineering, METU** _____

Assoc. Prof. Dr. Barbaros Çetin
Co-supervisor, **Mech. Eng., Bilkent University** _____

Examining Committee Members:

Assoc. Prof. Dr. Özgür Bayer
Mechanical Engineering Dept., METU _____

Prof. Dr. Zafer Dursunkaya
Mechanical Engineering Dept., METU _____

Prof. Dr. Murat Köksal
Mechanical Engineering Dept., Hacettepe University _____

Assist. Prof. Dr. Hüseyin Kurtuldu
Bio5medical Engineering Dept., Başkent University _____

Assist. Prof. Dr. Altuğ Özçelikkale
Mechanical Engineering Dept., METU _____

Date: 04.03.2024

I hereby declare that all information in this document has been obtained and presented in accordance with academic rules and ethical conduct. I also declare that, as required by these rules and conduct, I have fully cited and referenced all material and results that are not original to this work.

Name, Surname: YİĞİT ATA AĞARTAN

Signature :

ABSTRACT

DEVELOPMENT OF AN INTERFEROMETRIC TECHNIQUE FOR MEASURING THE PROFILES OF THIN LIQUID FILMS

AĞARTAN, YİĞİT ATA
Ph.D., Department of Mechanical Engineering
Supervisor: Prof. Dr. Zafer Dursunkaya
Co-Supervisor: Assoc. Prof. Dr. Barbaros Çetin

March 2024, 115 pages

The development of electronic devices with higher performance in a smaller volume with advancing technology has increased the heat fluxes generated in the device. This problem has increased the use of passive cooling devices such as heat pipes, which contain liquid-gas equilibrium flow, have high heat transfer efficiency and do not require additional energy. Numerical modeling of the liquid-gas flow in such devices requires the determination of the liquid pressure directly related to the liquid geometry at the desired cross sections. In this thesis an interferometric measurement technique that can be used in measuring the profiles of thin liquid films encountered in grooved heat pipes is developed. The approach involves recording and analysis of the interferometric data obtained by passing a fiber optic probe over the liquid cross-section to determine the shape of the liquid-gas interface. This is achieved by simulating the propagation, reflection and refraction of the emitted laser beam through the test media and the interference with the reference beam to form the interference fringes, which is then compared to the experimentally observed counterpart to calculate the

liquid shape. The experimental method followed to determine the liquid film profile, the details of the software used to generate the simulation data and the criteria used to determine the level of agreement between the experimental and simulated data are explained.

Keywords: liquid film profile, fiber optic interferometer, measurement of radius of curvature, liquid geometry detection, interferometry

ÖZ

İNCE SIVI FİLMLERİN PROFİLİNİ ÖLÇMEK İÇİN İNTERFEROMETRİK BİR TEKNİK GELİŞTİRİLMESİ

AĞARTAN, YİĞİT ATA
Doktora, Makina Mühendisliği Bölümü
Tez Yöneticisi: Prof. Dr. Zafer Dursunkaya
Ortak Tez Yöneticisi: Doç. Dr. Barbaros Çetin

Mart 2024 , 115 sayfa

İlerleyen teknoloji ile daha küçük hacimde daha yüksek performansa sahip elektronik cihazların geliştirilmesi, cihaz içerisinde oluşan ısı akılarını arttırmıştır. Bu sorun sıvı-gaz denge akışını içeren, ısı transfer verimi yüksek ve ek enerji gerektirmeyen ısı boruları gibi pasif soğutma cihazlarının kullanımını artırmıştır. Bu tür cihazlardaki sıvı-gaz akışının sayısal olarak modellenmesi, istenen kesitlerde sıvı geometrisiyle doğrudan ilişkili sıvı basıncının belirlenmesini gerektirir. Bu tezde, yivli ısı borularında karşılaşılan ince sıvı filmlerinin profillerinin ölçülmesinde kullanılabilecek interferometrik bir ölçüm tekniği geliştirilmiştir. Yaklaşım, sıvı-gaz arayüzünün şeklini belirlemek için sıvı kesiti üzerinden bir fiber optik prob geçirilerek elde edilen interferometrik verilerin kaydedilmesini ve analizini içerir. Bu, yayılan lazer ışınının test ortamı boyunca yayılması, yansıması ve kırılması ve girişim saçaklarını oluşturmak için referans ışınla girişimin benzetimi ile elde edilir ve daha sonra sıvı şeklini hesaplamak için deneysel olarak gözlemlenen karşılığı ile kıyaslanır. Sıvı film profilini belirlemek için izlenen deneysel yöntem, benzetim verilerini oluşturmak için kullanılan yazılımın ayrıntıları ile

deneysel ve benzetim verileri arasındaki uyum düzeyini belirlemek için kullanılan kriterler açıklanmaktadır.

Anahtar Kelimeler: sıvı film profili, fiber optik interferometre, eğrilik yarıçapı ölçümü, sıvı geometri tespiti, interferometri

To my parents and my wife...

ACKNOWLEDGMENTS

First and foremost, I express my deepest gratitude to my supervisor, Prof. Dr. Zafer Dursunkaya. I am profoundly thankful for his expert guidance, both academically and psychologically, his unwavering support, encouragement, and understanding throughout my journey. He generously dedicated his valuable time to advise me on my academic development. Without his continuous support, I would not have been able to complete this PhD thesis.

In addition to my supervisor, I would like to acknowledge my co-supervisor, Assoc. Prof. Dr. Barbaros Çetin, for his steadfast support and valuable insights during my PhD studies.

Furthermore, I extend my gratitude to the members of my dissertation committee, Prof. Dr. Murat Köksal, Assoc. Prof. Dr. Özgür Bayer, Assist. Prof. Dr. Hüseyin Kurtuldu, and Assist. Prof. Dr. Altuğ Özçelikkale, for their attentive review and valuable feedback.

I would like to extend my gratitude to Prof. Dr. Halil Kamil Öge for his significant contribution to the equipment utilized in my study. Additionally, I express my appreciation to Prof. Dr. Çağatay Candan, Prof. Dr. Tolga Çiloğlu, and Prof. Dr. A. Aydın Alatan for their invaluable assistance during the critical stages of my research.

I want to express my appreciation to my manager, Bengi Demirçivi, and director, Dr. Akif Türker Gürer, of ASELSAN A.Ş. for supporting my graduate studies.

I want to thank my family—my mother, Mahi Ülker Ağartan; my father, Şeref Ağartan; and my brother, Mehmet Alp Ağartan—who always support me. Without them, none of my successes would be possible. I would also like to thank my aunt, Türkan Nacak; my uncle, Şirzat Nacak, and my cousins, Nihan Nacak and Oğuzhan Nacak, for always being ready to help at any time.

My deepest and sincerest gratitude is extended to my wife, Özge Elcan-Ağartan. It is difficult to articulate the unwavering support she provided during this challenging period. Her constant presence and unwavering trust in me are immensely valuable. I am truly fortunate to have her by my side, and I express my heartfelt appreciation for her.

I am also deeply grateful to Dr. Yiğit Akkuş for his enthusiastic support and encouragement. I extend my thanks to Mustafa Yalçın for his efforts in establishing the experimental setup, and to Hatice Dilara Uslu, whose assistance was invaluable at every stage of my thesis work. Furthermore, I would like to express my sincere appreciation to Nadir Akik for his insightful guidance and contributions throughout the study.

TABLE OF CONTENTS

ABSTRACT v

ÖZ vii

ACKNOWLEDGMENTS x

TABLE OF CONTENTS xii

LIST OF TABLES xv

LIST OF FIGURES xvii

LIST OF ABBREVIATIONS xxiii

CHAPTERS

1 INTRODUCTION 1

1.1 Literature Review 3

1.2 Objective, Originality and Outline of the Thesis 12

2 THEORETICAL BACKGROUND 15

2.1 Types of Interferometers 18

2.2 Fiber Optic Interferometer 21

2.3 Refractive Index of Materials 23

3 EXPERIMENTATION 25

3.1 Experimental Setup 25

3.1.1 Optical Unit 25

3.1.2 Mechanical Stage 29
3.1.3 Data Acquisition System 32
3.1.4 Optical Table and Camera 32
3.1.5 Reflective Test Pieces 32
3.2 Experimental Procedure 33
3.2.1 Determination of the Height of the FOP 34
3.2.2 Detection of Intensity Distribution of Laser Beam 38
4 MODELING OF LIQUID PROFILE *VIA* INTERFEROMETRY . . . 43
4.1 Thin Liquid Film Modeling 43
4.2 Interference Simulations 47
5 DATA ANALYSIS AND RESULTS 57
5.1 Comparison of Experimental and Simulated Data 63
5.1.1 FFT 63
5.1.2 Zero Crossing Method 65
5.1.3 Optimum Resolution for FFT Analysis 70
5.2 Determination of Liquid Film Profile 77
5.2.1 Effect of the Height of the FOP 83
5.2.2 Effect of Height of Liquid 85
5.2.2.1 Engine oil on gold-coated silicon wafer 85
5.2.2.2 IPA on gold-coated silicon wafer 87
5.2.2.3 Engine oil on gauge block 88
5.2.3 Effect of Inclination of Reflective Surface 90
5.3 Determination of Height of Liquid Film for Validation 94

6 CONCLUDING REMARKS 97

APPENDIX

A SPECIFICATIONS OF EXPERIMENTAL DEVICES AND TOOLS . 107

B COMPARISON TABLE FOR DIFFERENT HEIGHTS OF THE FOP 111

CURRICULUM VITAE 115

LIST OF TABLES

TABLES

Table 5.1 Summary table for comparison of the height of the FOP of 3.45 mm, 3.49 mm, 3.50 mm, 3.51 mm and 3.55 mm 82

Table 5.2 The simulation results for the experiments which is performed with the engine oil on the gold-coated silicon wafer for different heights of the FOP 85

Table 5.3 The simulation results that best fit the experimental data with different heights of the engine oil on the gold-coated silicon wafer . . 86

Table 5.4 The simulation results that best fit the experimental data with different heights of IPA on the gold-coated silicon wafer 87

Table 5.5 Simulation results for the experiments with the engine oil on the gauge block analyzed for different widths of the liquid film . . . 89

Table A.1 Specifications of the laser source [38] 107

Table A.2 Specifications of the fiber optic isolator [38] 108

Table A.3 Specifications of the fiber 0ptic beam splitter [38] 108

Table A.4 Specifications of the circulator [38] 109

Table A.5 Specifications of the photo detector [38] 109

Table A.6 Specifications of the fiber optic cable [38] 110

Table A.7 Specifications of step motor [38] 110

Table B.1 The comparison table for the height of the FOP of 3.45 mm, 3.49 mm, 3.50 mm, 3.51 mm and 3.55 mm, the height of the liquid film of twelve values equally spaced between 0.40 mm and 0.62 mm and the width of the liquid film of 5.04 mm. Additionally the simulation results covers the cases with the height of the liquid film of 0.64 mm for different probe heights. 111

LIST OF FIGURES

FIGURES

Figure 2.1 Interference colors on soap bubble [26] 16

Figure 2.2 Interference: (A) Constructive and (B) destructive [26] . . 17

Figure 2.3 Two point sources 18

Figure 2.4 Mach-Zehnder interferometer [29] 19

Figure 2.5 (A) Michelson interferometer [30], (B) Fabry-Perot interferometer [31], and (C)Sagnac interferometer [31] 20

Figure 2.6 Types of fiber optic interferometers: (A)Fabry-Perot, (B) Mach-Zehnder, (C)Michelson and (D)Sagnac [32] 21

Figure 2.7 (A) Structure of a fiber optic cable [34], (B) types of fiber optic cores [35], and (C) types of optic fiber signal index [35]. . . . 22

Figure 2.8 Schematic view of transmission, reflection, and absorption [37] 23

Figure 3.1 Fiber optic interferometer setup 26

Figure 3.2 Schematic representation of the experimental setup 27

Figure 3.3 Components of the experimental setup: (A) Fiber optic isolator, (B) fiber optic beam splitter, (C) circulator, (D) photodetector, (E) connector, and (F) fiber optic cable and fiber optic probe. 28

Figure 3.4 Mechanical stage 30

Figure 3.5 Step motor and micrometer controlled lateral motion carriages 31

Figure 3.6 Optical table 33

Figure 3.7 Reflective test pieces 34

Figure 3.8 FOP holder: The FOP can be positioned in a specific range in the vertical direction which the probe holder allows. 35

Figure 3.9 Recorded experimental data over engine oil on the gold-coated silicon: (A) High slope, (B) medium slope, and (C) no slope 36

Figure 3.10 The procedure for adjusting the location of the FOP to zero height: (A) The reflective piece is brought to a nearly horizontal position and positioned at a height near the tip of the FOP. (B) The FOP is lowered and positioned to make contact with the reflective surface. (C) The reflective piece is positioned with the help of micrometers to maintain its horizontal position at a known distance from the tip of the FOP. (D) The experimental liquid is added onto the reflective surface. 37

Figure 3.11 A focused photograph of the liquid film from the lateral view. The photograph was taken in two conditions, when the lightening panel is on and off. 38

Figure 3.12 Sample experimental data collected by the stationary receiving probe: (A) Intensity distribution of the FOP, and (B) Gaussian fit to the experimental data 40

Figure 3.13 Beam radius vs probe height 41

Figure 4.1 Schematic view of the test section 47

Figure 4.2 Beam coming out from the FOP and the path it follows where the FOP is at a location over the semicircular shaped liquid on the reflective test piece 48

Figure 4.3 A schematic view of the beams coming out from the slices from the surface of the FOP tip in one position of the FOP 50

Figure 4.4 Gaussian distribution of intensity and the slices at the FOP tip [43] 51

Figure 4.5 Three beams creating the interference at the FOP tip . . . 52

Figure 5.1 (A) Schematic view of aimed position of the observation by the camera. Perspective view may cause a deviation between the actual and observed dimensions. Schematic view of the position deviated from the aimed position of the camera. Positioning the camera (B) above or (C) below the targeted position causes an extra difference between the observed and actual values of the FOP and liquid heights. 58

Figure 5.2 Schematic view of the incorrect positioning of the micro-lens camera in the horizontal direction. This case causes the width of the reflective test piece which determines the liquid width, being observed larger than the actual value. 59

Figure 5.3 Experimental data of the engine oil on the gold-coated silicon wafer 60

Figure 5.4 Dimensions of the test section covering the probe height, the height and the width of the liquid film 61

Figure 5.5 The variable width slices used in FFT analysis for the right side of the experimental data collected with the engine oil on the gold-coated silicon wafer 63

Figure 5.6 Data filtered using Moving Average Method with the window size of 150 on the normalized raw experimental data 65

Figure 5.7 Frequencies obtained from zero crossing points of the filtered experimental data 66

Figure 5.8 Data section with low noise level used in the analysis to compare the experimental and simulation data in terms of frequencies 67

Figure 5.9 Experimental and simulation data overlapped by their midpoints 68

Figure 5.10 Frequency distributions of the experimental and the simulation data 68

Figure 5.11 Frequencies of the experimental and the simulation data in the equalized range 69

Figure 5.12 Data points to determine the midpoint of the experimental data for the engine oil on the gold-coated silicon wafer 70

Figure 5.13 Simulation data for the liquid film with a width of 5.04 mm, probe height of 1.49 mm, and height of 0.62 mm fitted on the experimental data by overlapping the midpoints of them. Simulated liquid film shape is shown with yellow. 71

Figure 5.14 Right side of the experimental data for the engine oil on the gold-coated silicon wafer 72

Figure 5.15 FFT analysis of the right part of the experimental data: (A) Slices of 4000 data points and (B) slices of 7000 points data . . . 73

Figure 5.16 FFT analysis the experimental and simulation data with a step size of 0.9 μm: (A) 100 beams, (B) 200 beams, (C) 400 beams, (D) 600 beams and (E) 800 beams. 75

Figure 5.17 FFT analysis the experimental and simulation data for 800 beams with a step size of (A) 4.5 μm, (B) 3.6 μm, (C) 2.7 μm, (D) 1.8 μm and (E) 0.9 μm. 76

Figure 5.18 The dimensions of the test section. The range of the height of the liquid film is obtained by using the dimensions read on the photograph with the help of the parametric drawing tool. The width of the liquid film is the width measured by a caliper of the gold-coated silicon wafer on which the liquid film is placed. The height of the FOP is arranged by using the micrometers in the experimental setup with an accuracy of ±0.01 mm. 77

Figure 5.19 Comparison of FFT of the experimental and simulation data for different step sizes 78

Figure 5.20 The frequencies obtained in the slices for the experimental and the simulation data with the number of the slices of 14 and the size of the slices of 3700 79

Figure 5.21 The low noise region of the frequencies of the experimental data 80

Figure 5.22 The frequency ranges with the equalized limits for the experimental and the simulation data 81

Figure 5.23 Rough experimental data for different FOP height (liquid width: 5.04 mm): (A) 1.5 mm, (B) 3.5 mm, (C) 5.5 mm and (D) 7.5 mm. 84

Figure 5.24 Photograph of the test section with engine oil on gauge block with rounded corners 88

Figure 5.25 Schematic view of the situation with inclined reflective surface 90

Figure 5.26 Experimental raw data of the cases in the horizontal position and the position inclined with 0.0225°. The zero point of the horizontal axis is aligned with the midpoint of the experimental data of the case in the horizontal position. Also the schematic view of the test section of the inclined case aligned with the is shown with an exaggerated angle. 91

Figure 5.27 Experimental raw data of the cases in the horizontal position and the position inclined with 0.0225° focused on the region with the optical signal 92

Figure 5.28 Frequency distribution graph obtained by superimposing the midpoints determined from the experimental data of the horizontal and the inclined cases 93

Figure 5.29 Schematic view of liquid addition on the reflective surface and change of the height of liquid (engine oil) and gas (air) under the probe 94

Figure 5.30 Raw experimental data collected during adding liquid on the reflective surface 95

LIST OF ABBREVIATIONS

ABBREVIATIONS

a	Amplitude of light wave, V/m
BNC	Bayonet Neill–Concelman
c	The speed of light in vacuum, m/s
CCD	Charge-coupled device
d	Actual path length, m
DC	Direct current
DFB	Distributed feedback
E	Electric wave field, V/m
f	Wave frequency, Hz
FC/APC	Fiber connector with angled physical contact
FC/PC	Fiber connector with physical contact
FFT	Fast Fourier Transform
$FOTP$	Fiber optic thickness probe
FOP	Fiber optic probe
g	Gravity, m/s^2
GO	Graphene oxide
h	Height, m
HCF	Hollow core fiber
$HIFOSS$	Highly stable laser diode source
IPA	Isopropyl alcohol
J	Jacobian
LCI	Low-coherence interferometry

n	Refractive index
N	Number of beams
$N_{fringes}$	Number of fringes
OCT	Optical coherence tomography
OPL	Optical path length, m
P	Pressure, Pa
PIC	Peripheral interface controller
r	Distance between source and point, m
R	Reflectance
$\mathcal{R}$	Radius of curvature, m
RTA	Ray-tracing-assisted
$RK4$	4th–order Runge-Kutta
S	Source
$SMF\text{-}HCF\text{-}SMF$	Single mode-hollow core-single mode fiber
t	time, s
$UERMF$	Ultrasonic echo resonance main frequency
v	The speed of light in medium, m/s
w	Width, m

Greek Symbols

λ	Wavelength, m
ϵ_0	Permittivity of free space, $C^2/(N \cdot m^2)$
θ	Angle, radians or degrees
σ	Surface tension, N/m
Δ	Delta
δ	Liquid film thickness, m

ρ	Density, kg/m^3
ϕ	Phase angle, radians or degrees

Subscripts

c	Capillary
exp	Experiment
FFT	Fast Fourier Transform
g	Gravitational
i	Incident
j	Index number
l	Liquid
r	Reflected
rtn	Returning beam
sim	Simulation
t	Refracted transmitted
v	Vapor

CHAPTER 1

INTRODUCTION

Today, the number of transistors in microchips of electronic components and consequently the amount of heat dissipation in the electronic devices are increasing with the developing technology. These transistors are also packed into smaller volumes for production of high-performance devices in smaller sizes. This situation causes an increase in heat generation within electronic components and creates the need to develop more effective cooling methods. In such cases, single- or two-phase liquid cooling comes to the fore as one of the effective cooling methods. Heat pipes, which are one of the passive liquid cooling methods, contain a fluid in liquid gas balance in a metal body with capillary or grooved structures. The liquid movement in the heat pipe is realized by the liquid surface tension created by the capillary structures. In order to simulate this motion numerically, it is necessary to determine the pressure distribution in the liquid resulting from the liquid surface tension, which is directly related to the liquid profile. The starting point of this study is to present a measurement technique for applications where such liquid profile detection is essential.

Interferometry is indeed one of the most sensitive and accurate techniques for measuring various physical quantities. Its sensitivity and precision stem from the ability to exploit interference patterns to make extremely precise measurements of light, radio waves, and other waves. Here are some reasons why interferometry is highly sensitive and accurate [1]:

- **High-precision:** Interferometric measurements can achieve high precision due to the ability to measure small phase differences or changes in wavefronts. This precision allows for accurate determination of distances,

wavelengths, and other quantities.

- **Interference enhancement:** Interference patterns can enhance the measurable signal, especially when combining multiple waves constructively. This enhancement allows for the detection of weak signals that might be difficult or impossible to measure with other methods.

- **High-resolution:** Interferometry can achieve high spatial resolution, especially in imaging applications, by utilizing the wave nature of light. For example, in optical interferometry, it is possible to resolve fine details in astronomical objects that would be challenging to observe using conventional telescopes.

- **Non-destructive nature:** In many cases, interferometry is a non-destructive measurement technique, allowing scientists and engineers to study and analyze samples without altering or damaging them.

- **Wide range of applications:** Interferometry has applications in various fields, such as astronomy, metrology, remote sensing, optical testing, geodesy, seismology, and more. Its versatility makes it a valuable tool in diverse scientific and engineering domains.

- **Calibration capabilities:** Interferometers can be accurately calibrated, ensuring that the measurements are traceable to standardized units and improving the overall accuracy of the technique.

- **Interferometric fiber optic sensors:** In recent years, interferometric fiber optic sensors have become increasingly popular due to their high sensitivity and accuracy in measuring physical parameters such as temperature, pressure, strain, and refractive index.

Among different types of interferometers, the fiber optic interferometer offers compactness, small size, lightweight, and robustness against vibration and environmental factors. It is also ideal for applications where EMI is a concern due to its immunity to electromagnetic interference. Furthermore, it is suitable for measuring a wide range of optical path lengths and typically cost-effective

compared to other types of interferometers, which leads to an affordable option for a wide range of applications.

1.1 Literature Review

In this section, the methods employed for the measurement of liquid film thickness, determination of the shapes of the liquid films, and the studies conducted with fiber optic interferometers are explained.

Park et al. [2] discussed the principles and applications of optical interferometry for measuring the thickness of thick transparent layers in various industrial fields. The paper explores different interferometry techniques, including monochromatic laser interferometry, low-coherence interferometry, and spectral interferometry. Specifically, spectrally resolved and wavelength-scanning interferometry techniques were analyzed within the context of spectral interferometry. The working principle of interferometry was explained by analyzing the interference patterns created by the interaction of light waves reflected from different surfaces of a sample. The challenges and limitations of interferometry, such as the 2π ambiguity problem and the need for accurate wavelength scanning were also discussed. Various strategies to overcome these challenges and limitations were presented, including phase unwrapping techniques and customized phase measurement algorithms. Key parameters and characteristics of different interferometry techniques were also presented.

Tibiriçá *et al.* [3] conducted a comparative analysis of techniques outlined in existing literature that pertain to the quantification of liquid film thickness within systems of both macro and micro scales. These methodologies can be categorized according to distinct physical principles governing their operation. Among these categories, electrical approaches center on the measurement of electrical conductance or the potential difference occurring across electrodes as a means to ascertain the thickness of the film. This technique is simple and widely used in macro-scale systems. As an alternative, optical methods utilize light-based techniques to measure the film thickness. Examples include total internal reflection

of light, laser focus displacement, and interferometry. These methods are non-intrusive and can provide accurate measurements. Nucleonic techniques involve the use of radioactive isotopes or other nuclear-based techniques to measure the film thickness. These techniques are less commonly used and may have limitations in terms of safety and practicality. Every method possesses its unique strengths and constraints, and the selection of a particular method is depends on the specific conditions and requirements of the experiment.

Israelachvili [4] utilized multi-beam interferometry for the determination of film thickness (ranging between zero and a few angstroms) and refractive index. The methodology involved entrapping a slender film between two flexible and transparent sheets, which were coated with a layer of silver on their outer surfaces. Illuminating one of the silver-coated surfaces with white light resulted in the transmission of specific wavelengths. These wavelengths underwent separation and manifested as an arrangement of patterns in a spectrogram. Introduction of a thin film amid the two sheets led to a displacement of the patterns towards longer wavelengths. The extent of these displacements facilitated the measurement of film thickness with a precision of approximately $\pm 1\mathring{A}$, and the calculation of its refractive index with an accuracy of around ± 0.01.

Laser interferometry was implemented to measure the instantaneous thickness or shape of the liquid film flowing at small Reynolds numbers [5]. This technique involved measuring the interference pattern created by two interfering rays reflected from the inner and outer surfaces of the film. By analyzing this interference pattern, the thickness and shape of the film was determined. The method was noninvasive and provided information about the film at a specific point in a horizontal cross section. With this technique, the typical accuracy of the thickness measurement was between 4% and 8%, and the maximum thickness of the liquid film presented was 365 μm.

Shabana [6] assessed the dimensions and contours of thin polypropylene films with transparency employing interferometric techniques. Interferometry encompassed the examination of patterns of interference fringes generated either within an air wedge or in accordance with the principles of two-beam interference. The

technique of air wedge interference involved in deducing film thickness through the analysis of fringe displacement data in conjunction with knowledge of the film's refractive index and the refractive index of the immersion medium. Moreover, Pluta microscope and the Michelson interferometer were employed to extract the requisite data pertaining to film thickness and refractive index by scrutinizing the configurations of interference fringe patterns. The investigated thickness of the liquids were below 50 μm.

Low-Coherence Interferometry (LCI) is a non-disruptive approach employing optical components like a low-coherent light source, a beam splitter, and a sensor to deduce the variation in optical path between two segments of an interferometer. Borgetto et al. [7] suggested LCI method to measure the thickness of a liquid film with thermal gradient. LCI involved using a low-coherence light source and an interferometer to measure the optical path length (OPL) of the light passing through the liquid film. By subtracting the OPL values before and after passing through the liquid film, the thickness of the film could be determined. This technique was based on the interference of light waves and could provide accurate measurements of the film thickness.

Borgetto *et al.* [8] also implemented LCI to evaluate the dimensions or contours of a liquid film . By analyzing the interference patterns produced by the reflected light, the film thickness and wall temperature was bale to be determined. The film thickness was calculated based on the group refractive index of the liquid film and the measured optical path length, while the wall temperature was determined by measuring the amplitude of the electromagnetic fields in the interferometer arms. They determined an uncertainty of 3.5% for the 146 μm thickness of the liquid film of heptane.

Interforemetry was also utilized for the measurement of the thickness or shape of thin liquid crystal films [9]. In this methodology, a single-wavelength phase shifting interferometry technique was implemented. The measurements obtained from this technique generated 3D topographical images. For films with thicknesses greater than 1 μm, two independent measurements were performed on the upper surface of the film and the film-substrate interface. For films with thick-

nesses less than 1 μm, only one fringe pattern was observed, which corresponded to the metal surface. The methodology was corrected for the difference in height between the coated and uncoated regions of the substrate and calculated the film thickness based on the height of the step in the corrected image.

The study performed by Gao et al. [10] employed wavelength scanning interferometry which integrated a halogen light source and an acousto-optic tunable filter. This integration served to produce a series of filtered light pulses within a Linnik interferometer, facilitating the assessment of the thickness of a transparent film. The outcome was a sequence of interferograms captured through a CCD camera. By utilizing frequency-domain analysis, the interference signals originating from both the upper and lower surfaces of the film, as well as the multiple reflection signals occurring between these surfaces, were disentangled. This disentanglement was accomplished through an optimized Fourier Transform Technique (FTT). The measurement setup encompassed two interferometers that shared a common optical path, enabling the reconstruction of surface and thickness information by combining the acquired signals with the refractive index of the thin film.

Shang and Chen [11] employed an approach termed partial coherent interferometry as a non-intrusive method for evaluating the evolving thickness pattern of a moving liquid sheet. This technique exploited the linear correlation between the degree of coherence and the optical path difference to ascertain the sheet's thickness. In an interferometer, by utilizing a partially coherent laser, interference patterns were digitally captured prior to and subsequent to the insertion of the liquid sheet. The proportional thickness distribution was deduced by applying a phase unwrapping process to the acquired interference pattern. By gauging alterations in the degree of coherence prompted by the sheet, the absolute thicknesses at reference points were established. Through alignment of the relative thickness with absolute thicknesses at distinct locations, the complete distribution of absolute thickness was extracted.

Ultra-thin film interferometry to measure the thickness of very thin lubricant films was utilized in the study of Glovnea et al. [12]. This technique involved

placing a reflective ball against a rotating transparent disc, with the ball partially immersed in a lubricant reservoir. The interference of light was used to determine the film thickness. In the modified method, a multiple-beam interference analysis was implemented to determine the wavelength of maximum constructive interference, providing a more accurate measurement of film thickness. The thickness distribution changing from 26 μm to 38 μm for static ethanol film were measured with an uncertainity of 2.1 μm.

Dipresa [13] described the use of interferometric fringe projection and fluorescence stimulated emission for the measurement of optical thin films in his PhD thesis. The technique of interferometric fringe projection entailed casting a pattern of fringes onto the film's surface and quantifying the phase alteration in the reflected light as a means of deducing the film's dimensions or thickness. Fluorescence stimulated emission employed the absorption and re-emission of fluorescent dyes, providing a precise means of gauging film thickness while mitigating discrepancies arising from fluctuations in illumination intensity and surface reflectance.

Beisswanger et al. [14] focused on utilizing interferometric radius of curvature assessments and puts forward an approach to reduce temporal fluctuations that could affect measurements. This strategy aimed to attain extremely accurate measurements even in environments with less stringent controls. The study employed a fiber optic interferometer to gauge minute deviations in the geometry of spherical surfaces, achieving precision at the sub-nanometer scale. The primary objective was to ascertain the radius of the sphere under examination. The researchers introduced an approach to counteract the impact of drift, substantiating its efficacy through practical experiments. They additionally explore common sources of errors and strategies to diminish their influence. The study encompassed measurements conducted in challenging environmental scenarios and deliberate extensions of measurement durations. The outcomes illustrated that this method curtailed the variability in measurements, enabling accurate interferometric radius determination without stringent environmental regulations. A comparison between two prevalent setup configurations demonstrated close agreement in results, differing by only 16 nm when measuring a sample with a

radius of curvature of 20 mm.

A common-path tandem interferometer was proposed by Lin and Le [15] as a method to measure thin-film thickness. The interferometer utilized a white light laser, an optical path difference modulation module, and an interference module. The measurement process involved illuminating the sample with a laser beam and capturing the interference pattern generated by the multireflection interference at the sample surface. The interference pattern contained information about the sample thickness, which could be extracted by analyzing the period or lateral shift of the interference pattern. The interferometer offered non-contact, high-resolution, and full-field measurements with high repeatability and tolerance to environmental disturbance.

Buffone *et al.* [16] used a fiber optic probe to measure the film thickness on a curved surface. The sensor was comprised of a pair of fibers: (i) an emitting fiber for illuminating the object, and (ii) a receiving fiber to gather the light reflected by the object. This non-intrusive probe was successful at gauging film thickness even on curved surfaces. The method offered a large bandwidth and notable spatial precision (resolutions of 150 μm and 300 μm, respectively). The film thickness was measured at two different locations along the curved surface.

A method based on reflection-type fiber-optic sensors was applied to measure the thickness or shape of a liquid film [17]. The sensors consisted of a single-mode or multi-mode optical fibers that were fixed in a sleeve and mounted flush with the plate on which the liquid film flows. The probe radiation from a radiation source, such as a laser or a halogen incandescent lamp, was fed into the optical fiber and emerged from it as a conic beam. Part of the probe radiation was reflected by the film surface and returned into the optical fiber. The intensity of the reflected beam depended on the distance to the reflecting surface and the angle of its tilt. By analyzing the intensity of the reflected beam, the thickness or shape of the liquid film was able to be determined.

Huang et al. [18] evaluated the advancements achieved in the field of Fabry-Perot interferometric fiber-optic sensors. The paper explored the substantial range of applications these sensors find utility in, spanning magnetic fields, stress and

strain analysis, vibration monitoring, humidity detection, current measurement, gas analysis, and pressure evaluation. The study introduced a comprehensive model elucidating the fundamental operating principle of these sensors. This includes an examination of phenomena like the Gouy effect and the divergence of the light beam within a Fabry-Perot cavity. Moreover, the paper delved into the diverse designs and uses of these sensors, encompassing tasks such as temperature measurement, determining the refractive index of liquids and solids, and gauging small displacements. The research culminated with a prospective exploration of potential avenues for the application of these sensors.

Wu et al. [19] introduced a technique for thickness measurement based on a unique configuration comprising a single-mode–hollow core–single-mode fiber structure. The method involved applying a fine layer of material onto the exterior of the hollow core optical fiber. The subsequent measurement of this coating's thickness was facilitated using this specific fiber arrangement. Theoretical analysis suggested that this structure hold the capability to gauge coating thickness at an ultra-fine scale approaching sub-nanometer dimensions. Empirical outcomes, utilizing a thin graphene oxide layer on the surface of a hollow core optical fiber, reveal that the fiber sensor arrangement could detect even the thinnest layers, with a minimum thickness of 0.21 nm.

Mizushima [20] introduced a novel approach, termed the ray-tracing-assisted (RTA) technique, to calibrate a fiber-optic thickness probe (FOTP) for quantifying liquid film thickness in flowing conditions. This method revolved around investigating the emission characteristics of a multi-mode optical fiber using ray tracing. The evaluation revealed superiority of step-index multi-mode fibers concerning thickness precision and mitigating uncertainties. The validation of the RTA calibration technique was performed for simulated thickness measurement in motionless scenarios and compared with visualization outcomes.A numerical confirmation through computer-simulated liquid-film flow was also presented. The study delved into the operational range of thickness and discusses the associated measurement uncertainties of the FOTP.

Shedd and Newell [21]employed an automated optical methodology for the quan-

tification of liquid film thickness or shape. This approach involved the utilization of light that is reflected from the surface of a liquid film as it moved over a transparent barrier. The resultant reflected light shaped an image on the external surface of the barrier, which was subsequently captured and digitized through the implementation of a charge-coupled device (CCD) camera and framegrabber card integrated into a desktop computer. The image was post-processed to ascertain the positions of the reflected light beams. These positions served as the basis for computing the actual film thickness. The entire process was characterized by automation, enabling the acquisition of an extensive dataset comprising 600 data points in approximately 4 min, all achievable with the aid of a personal computer equipped with a 486 microprocessor. Notably, this technique was able to accurately determine film thicknesses at the scale of about 0.01 mm, using cost-effective components. Furthermore, the potential for enhanced precision exists when employing more advanced imaging tools. Remarkably, an automated calibration procedure facilitates the determination of essential physical parameters, obviating the need for *a priori* knowledge of the refractive index of the test fluid or the wall of the test section.

Wang *et al.* [22] introduced ultrasonic echo resonance main frequency (UERMF) technique, a novel approach for the precise measurement of micrometer-scale liquid film thickness within gas-liquid flows. This method effectively surpassed the constraints associated with conventional ultrasonic pulse echo and thin film resonance techniques. Employing the ultrasonic echo resonance approach, the UERMF method identified the primary frequency within the spectrum waveform of the reflection coefficient and utilized this information to compute the thickness of the liquid film. Notably, the capibility of UERMF method was demonstrated for the accurate measurement of liquid film thickness across both static and dynamic experimental scenarios. The relative error between the measurements made by the particle image and UERMF methods was found to be below 2.7%.

Several methods for measuring the thickness of thin liquid films are available in the literature [23]. There are mainly two groups: image-based and capacitance-based techniques. Image-based method entails employing a high-resolution, high-speed camera to acquire visuals of the liquid film. Subsequently, the scale

of the imagery is established by referencing a recognized standard object within the camera's view, enabling computation of the liquid film's thickness with respect to the determined scale. This method is contactless and does not affect the flow field of the liquid film. It offers high measurement accuracy but requires several processing steps, including image capture, gray value acquisition, scale solution, and thickness calculation [23]. The capacitance-based technique, on the other hand, is based on the dielectric constant of the liquid film. It involves using probes to measure the capacitance of the liquid film, which is then used to determine the thickness. This approach is convenient and offers precise discernment of both gas-liquid and liquid-solid boundaries. It proves effective for extensive data collection when measuring liquid film thickness. Nevertheless, the probes employed in this technique can exert an impact on the liquid film's flow dynamics, presenting a drawback. Additional techniques discussed in the article encompass the ultrasonic method, which employs ultrasonic pulse echo technology and signal processing approaches to gauge film thickness within annular geometries [23].

Cherdantsev et al. [24] presents an approach for assessing film thickness through laser-induced fluorescence. In this technique, fluorescence intensity was integrated along the optical path and subsequently transformed into film thickness employing the Lambert-Beer law. This method facilitated exceptional spatial resolution, expansive coverage, the ability to capture three-dimensional film thickness data, and simultaneous investigation of waves, droplets, and bubbles. The authors acknowledged that optical distortions might arise due to sharp gradients and pronounced curvature of the interface, potentially constraining the method's applicability.

Confocal microscopy was also used to measure the thickness or shape of the dynamic thin liquid films [25]. This technique analyzed the reflection intensity of the film interface as a function of the objective lens location to precisely determine the film thickness. The confocal microscope captured images of the film interfaces by scanning at a speed of 200 frames per second during the experiments. The scanning speed was able to potentially be increased up to 3000 frames per second to improve accuracy. Another method mentioned was

eliminating the physical motion of the scanning galvometer, which would allow for faster imaging using a high-speed camera.

1.2 Objective, Originality and Outline of the Thesis

In numerical modelling of the liquid flow occurring in heat pipes, it is necessary to know the pressure distribution on the liquid surface. For this purpose, this study aimed to develop a technique for the measurement of liquid profile, which is directly related to the pressure distribution on the liquid surface by using a fiber optic interferometer. With this method, it is possible to determine the profiles of all liquids that can spread on surfaces and are sufficiently transparent to the laser beam employed. The only restriction of the current method is that the surface on which the liquid spreads needs to be reflective with sufficiently low scattering.

In the proposed method, a fiber optic probe traverses a liquid interface, and gathers interferometric intensity data along the entire cross-section of the liquid. A simulation tool based on beam tracing is also developed which generates interforemetric data for a given interface geometry by calculating (i) the optical paths of the laser beams coming out of the fiber optic probe, (ii) intensity change due to expansion of the beams and difference in the refractive indices of the mediums which the beams pass through, and (iii) intensity values created by the interference of the beams. This simulation tool is utilized to match the experimental intensity data to determine the exact shape of the liquid interface. The simulation model also extrapolates the shape of the interface for regions where intensity data could not be collected along the path of motion of the fiber optic probe. In contrast to other alternative methods documented in the literature, the proposed method involves passing the fiber optic probe across the entire cross-section, rather than obtaining measurements from a narrow area. This method enables the acquisition of intensity data containing information about the cross-sectional geometries of static liquid films with widths ranging from millimeters and above, all in a single operation. In addition, the proposed technique only requires standard, relatively low-cost optical components includ-

ing laser source, circulator, photodetector and fiber optic cables together with mechanical motion carriages.

In this thesis, Chapter 2 briefly summarizes the background information about the theory of optical interference and the types of main interferometers. The benefits of the fiber optic interferometers and potential application areas are also explained. Chapter 3 describes the experimental setup for fiber optic interferometer which is utilized to detect the interface geometry of the liquid film on a reflective surface. The experimental procedure is also discussed in detail. Chapter 4 provides the details of simulation model implemented to determine the shape of the interface. Chapter 5 demonstrates the analysis of simulation data aimed at determining the fluid profile geometry, which corresponds to the experimental data obtained. Finally, a summary of the main findings is presented in Chapter 6.

CHAPTER 2

THEORETICAL BACKGROUND

In this section, brief information about the theory of interferometry, different types of interferometers, the working principles of fiber optic interferometers, the structure of the fiber optic cables and the refractive index of materials are explained.

The interference of light waves can be observed in numerous everyday objects, such as oil slicks and soap films. When white light impinges on these objects, different wavelengths of light interfere with each other, creating a colorful pattern that has colored fringes. An example of colored fringes on a soap bubble is shown in Figure 2.1. An increase in the thickness of the film leads to less visible fringes due to the increase in the optical path length difference between interfering wavefronts. In contrast with white light, monochromatic light can create visible fringes even in the case of thick films. The short wavelength of visible light enables the measurement of minute changes in the optical path difference, which makes optical interferometry a highly accurate measurement technique.

Optical interferometry has been employed for over a century, but it has become even more powerful with several new developments. The invention of laser light, which is capable of generating monochromatic light with high intensity, has enabled the generation of very coherent light, which has opened up new possibilities for the development of new interferometric techniques. The introduction of single-mode optical fibers has also extended the applications of interferometry. Interferometry has been utilized for a wide variety of measurements, including the accurate measurement of distances, displacements, and vibrations. It has been also utilized to test optical systems, study gas flows and plasmas, in the

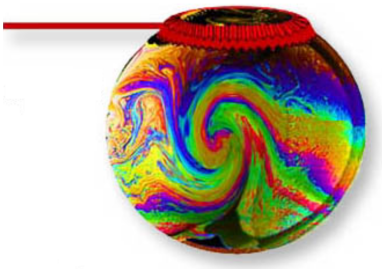

Figure 2.1: Interference colors on soap bubble [26]

measurement of temperature, pressure, and electrical and magnetic fields, and sense rotation. In recent years, interferometry has also been applied to high-speed all-optical logic and the detection of gravitational waves[27].

Light is commonly understood as a transverse electromagnetic wave that travels through space. The electric and magnetic fields of light are interconnected and propagate together. When we try to understand the interference of light, first we need to understand constructive and destructive interference. Let's consider a pair of light waves that originate from the same source propagating in a certain direction (say in direction D in Figure 2.2). The light waves may interfere with one another if the vibrations, which are perpendicular to the direction of propagation (direction C in Figure 2.2), are parallel to one another, and also parallel with respect to the direction of vibration. The vibrations cannot interfere with one another if they are vibrating in different planes and at right angles to one another. If the aforementioned conditions are satisfied, the waves may interfere with one another either positively or negatively. The amplitudes are additive if the crests of one wave coincide with the crests of the other. The resultant amplitude doubles if the amplitudes of the two waves are equal. Keeping in mind that the square of the amplitude determines how much light is present. Therefore, doubling amplitude results in a quadrupling of the intensity. Constructive interference is the name given to such additive interference. As seen in Figure 2.2B, the resulting amplitude is reduced or may even be totally cancelled if the crests of one wave coincide with the troughs of the other wave, which is called as destructive interference. As a result, the intensity reduces, or in the case of absolute cancellation, it may results in darkness [26].

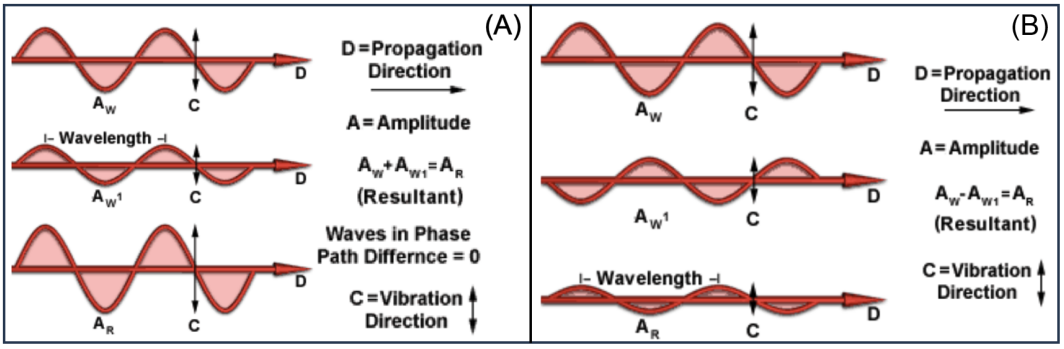

Figure 2.2: Interference: (A) Constructive and (B) destructive [26]

The electric and magnetic fields of light are interconnected and propagate together. Therefore, it is often satisfactory to focus solely on the electric field at a given point. For a mathematical modeling of interference where two point light sources (S_1 and S_2) create in the location P (as shown in Figure 2.3), let us consider the electric field measured at point P from source S_1 due to a light wave [27]:

$$E_1(P,t) = a_1(P)\sin\left(2\pi ft - \frac{2\pi}{\lambda}r_1\right) \tag{2.1}$$

where $E_1(P,t)$ is the electric field at point P at any given time (t). a_1 is the amplitude of the light wave, f is the frequency of the wave, λ is the wavelength, and r_1 is the distance between source S_1 and point P. Similarly, the electric field measured at point P from source S_2 can be written as:

$$E_2(P,t) = a_2(P)\sin\left(2\pi ft - \frac{2\pi}{\lambda}r_2\right) \tag{2.2}$$

Equation 2.1 and Equation 2.2 can be recast in terms of their amplitudes and phases as:

$$\begin{aligned} E_1(P,t) &= a_1(P)\sin\left(2\pi ft - \phi_1(P)\right), \\ E_2(P,t) &= a_2(P)\sin\left(2\pi ft - \phi_2(P)\right) \end{aligned} \tag{2.3}$$

The total electric field can be obtained as:

$$E_{total}(P,t) = a_1(P)\sin\left(2\pi ft - \phi_1(P)\right) + a_2(P)\sin\left(2\pi ft - \phi_2(P)\right) \tag{2.4}$$

The magnitude of the total electric filed can be written as:

$$\mid E_{total}(P,t) \mid^2 = a_1a_2\cos\left(\phi_1 - \phi_2\right) - a_1a_2\cos\left(4\pi ft - \phi_1 - \phi_2\right) \tag{2.5}$$

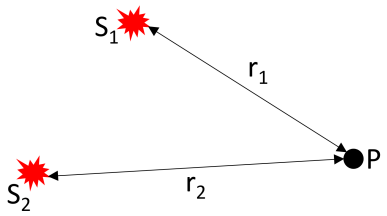

Figure 2.3: Two point sources

The intensity is proportional to the time-average of the square of the magnitude of the electric field. Note that, time-average of $\sin(t)$ (and $\cos(t)$) becomes zero, and the time-average of $\sin^2(t)$ becomes 0.5. Therefore, time-average of Equation 2.5 can be obtained as:

$$\left\langle \mid E_{total}(P,t) \mid^2 \right\rangle = \frac{a_1^2(P)}{2} + \frac{a_2^2(P)}{2} + a_1(P)a_2(P)\cos\Big(\phi_1(P) - \phi_2(P)\Big) \quad (2.6)$$

where $\langle\cdot\rangle$ denotes time-averaged quantity. Total intensity (which has a unit of $[\mathrm{W/m^2}]$) can be written as:

$$I_{total}(P) \equiv \epsilon_0 c\left\langle \mid E_{total}(P,t) \mid^2 \right\rangle = I_1 + I_2 + 2\sqrt{I_1 I_2}\cos(\phi_1 - \phi_2) \quad (2.7)$$

where ϵ_0 is the permittivity of free space, and c is the speed of light at vacuum. Equation 2.7 is known as two-beam interference equation.

2.1 Types of Interferometers

Due to their high level of precision and relatively simple construction, interferometers are one of the most widely used optical devices. An interferometer divides incoming light (often a laser beam) into two beams: a reference and a measurement beam. Through an optical channel, the reference beam moves without modification. A change in the optical route has an impact on the measurement beam since it follows a different path. Physical parameters aimed to be measured (such as temperature, pressure, distance or refractive index of transparent mediums are the cause of the change. The two beams are then recombined on a screen, where their interference results in an interference pattern of interference fringes. Different types of interferometers exist for specific pur-

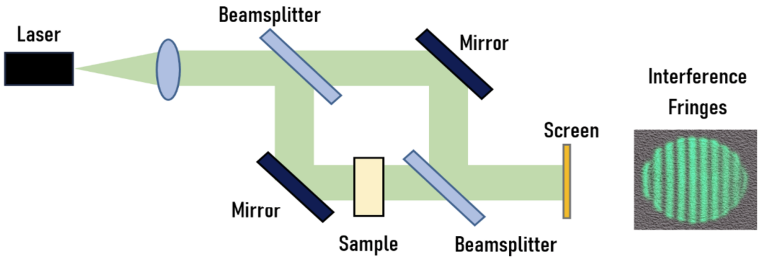

Figure 2.4: Mach-Zehnder interferometer [29]

poses; however, more commonly used ones are the Mach-Zehnder, Michelson, Fabry-Perot and Sagnac interferometers, or derivatives of them [28].

(i) **Mach-Zehnder Interferometer:** In Mach-Zehnder Interferometer, a coherent light like a laser is divided into two beams by beam splitters, and then the divided beams are recombined and the resulting interference pattern is projected on a screen or a light intensity sensitive detector with the help of the mirrors and beam splitters, as shown in Figure 2.4. The Mach-Zehnder Interferometer has been applied in various areas, including the measurement of minute displacements, determining the refractive index of transparent materials, analysing air flow in wind tunnels [29].

(ii) **Michelson Interferometer:** In Michelson Interferometer, a coherent light is split into two beams by a beam splitter, and then the divided beams are reflected back and recombined to create an interference pattern on a screen with the help of two mirrors, as shown in Figure 2.5A. Michelson Interferometer has been implemented in various applications in interferometry and precision measurements, spectroscopy, testing optics, laser frequency stabilization, optical coherence tomography (OCT), fringe pattern visualization, motion detection and vibration analysis, surface profiling, quantum optics and fundamental research, and gravitational wave detection [30].

(iii) **Fabry-Perot Interferometer:** The Fabry-Perot Interferometer operates on the principle of multiple beam interference, as shown in Figure 2.5B. It consists of two partially reflecting mirrors, known as the Fabry-Perot etalons, arranged in parallel with a small separation. A monochromatic

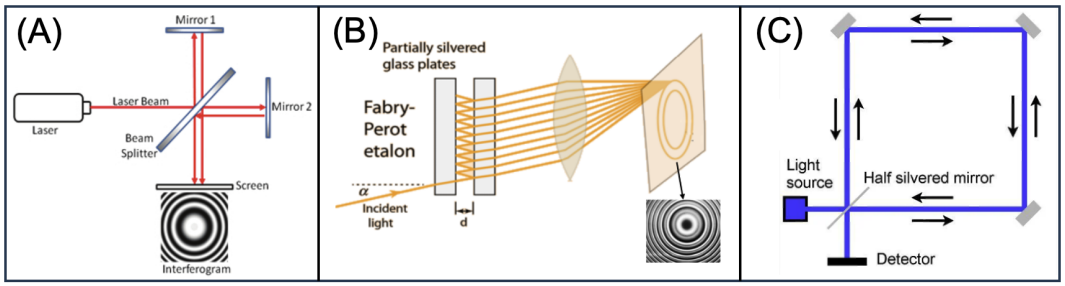

Figure 2.5: (A) Michelson interferometer [30], (B) Fabry-Perot interferometer [31], and (C)Sagnac interferometer [31]

light source is directed towards these mirrors. When the light wave enters the interferometer, it is in part reflected from the first mirror and is in part transmited through it. The transmitted light is then reflected by the second mirror and goes back to the first mirror, where it is again partially reflected and transmitted. This process continues, causing multiple reflections between the mirrors. Due to the constructive and destructive interference of these reflected beams, certain wavelengths of light are enhanced (constructive interference) and others are suppressed (destructive interference). The transmission pattern, or interference pattern, is observed as a series of sharp peaks and deep valleys in the intensity of the transmitted light. The Fabry-Perot Interferometer has been utilized in spectroscopy, laser frequency analysis, tunable filters, fiber optic sensors, atomic and molecular physics, airborne remote sensing, interferometric imaging, optical communication, astronomical observations, and vibration and displacement sensing [31].

(iv) Sagnac Interferometer: In Sagnac Interferometer, light is divided into two beams, which then travel along the same path but in opposite directions. Upon returning to the starting point, both beams exit the system and undergo interference, as shown in Figure 2.5C. When the interferometer is stationary, both light beams travel at the same speed, resulting in maximum detector output due to the absence of a phase difference. However, when the interferometer is rotated, one beam lags behind the other, causing a phase difference that alters the detector output. Sagnac Inter-

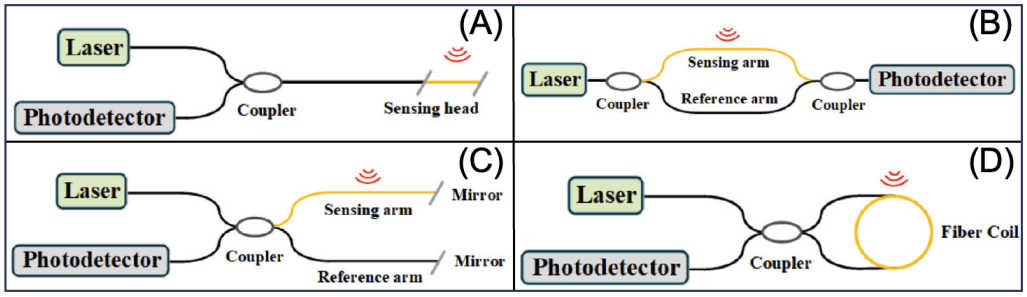

Figure 2.6: Types of fiber optic interferometers: (A)Fabry-Perot, (B) Mach-Zehnder, (C)Michelson and (D)Sagnac [32]

ferometer has been applied in navigation and inertial sensing, geodesy and Earth rotation studies, quantum optics and fundamental research, fiber optic gyroscopes, rotation sensors in industrial applications, seismic and vibrational monitoring, testing of fundamental physics theories, and enhancements in gravitational wave detection setups [31].

2.2 Fiber Optic Interferometer

In each of these interferometric techniques, the pattern of fringes generated depends on both the optical path difference and characteristics of the light source. Optical waveguides and fibers offer control over the optical path, enabling the creation of highly compact and cost-effective devices. By employing optical fibers, these instruments can be designed to be exceptionally small and efficient. In addition, optical fibers provides numerous advantages, such as minimizing the impact of atmospheric turbulence on wave front distortion and the provision of compact beam-splitting and combining functions. These attributes render optical fibers as a well-suited medium for light transmission in extended baseline interferometers, which have diverse applications encompassing the detection of gravitational waves, intrusion sensing, monitoring structural well-being, and extensive-range leak detection setups [33]. Fiber optic arrangements can be utilized for the aforementioned interferometer types. In the fiber optic interferometers, the light paths are formed by the fiber optic cables. Four types of the fiber optic interferometers are demonstrated in Figure 2.6.

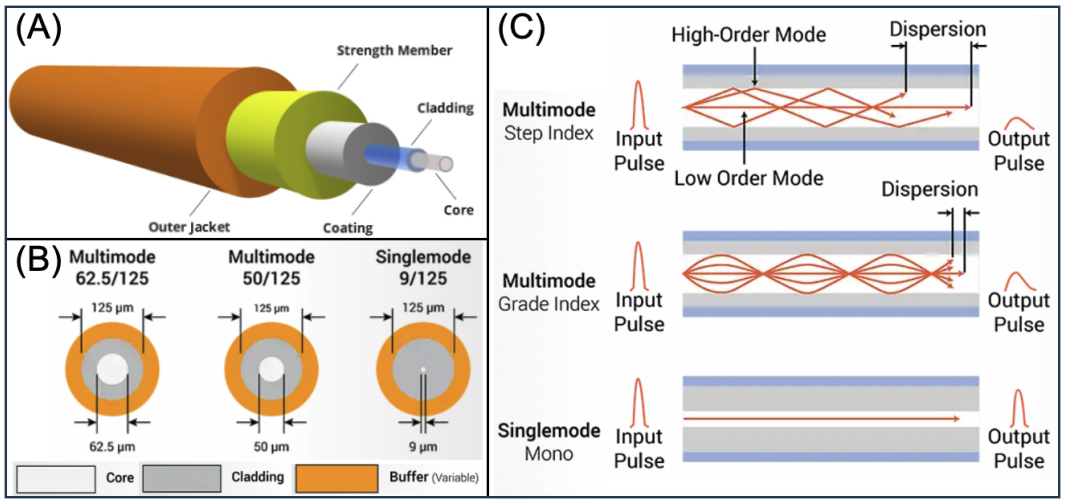

Figure 2.7: (A) Structure of a fiber optic cable [34], (B) types of fiber optic cores [35], and (C) types of optic fiber signal index [35].

One of the important components of the fiber optic interferometers is the fiber optic cable. Light travels along the centerline of the fiber optic cable which is called as the *core*. Surrounding the core, there is a layer of cladding which confines the light to the inside of the core along the fiber optic cable. The material of the core and the cladding is generally ultra-pure glass. The fiber is enveloped in a safeguarding plastic layer known as the *primary buffer coating* shielding it against moisture and physical damage. An additional protection is provided by a layer having strength members and the fibers. There is also a jacket covering all layers. This structure is shown in Figure 2.7A [36]. Fiber optic cables can be categorized into two groups as single-mode and multi-mode fiber optic cables, as illustrated in Figure 2.7B. Multi-mode optical fibers consist of a relatively larger core diameter (in general 50 µm or 62.5 µm) surrounded by 125 µm of cladding. This larger core allows light to propagate through the cable in multiple modes, resulting in various line spreads and reflection angles. As a consequence of the numerous reflections and refractions, the light in multi-mode fibers experiences a longer effective distance travelled than the physical length of the fiber itself. This phenomenon leads to a delay in signal delivery known as *dispersion*. On the other hand, single-Mode optical fibers also usually have a cladding diameter of 125 µm, but their core diameter is significantly smaller, measuring only 9 µm. This thin core diameter permits the transmission of a single-mode of

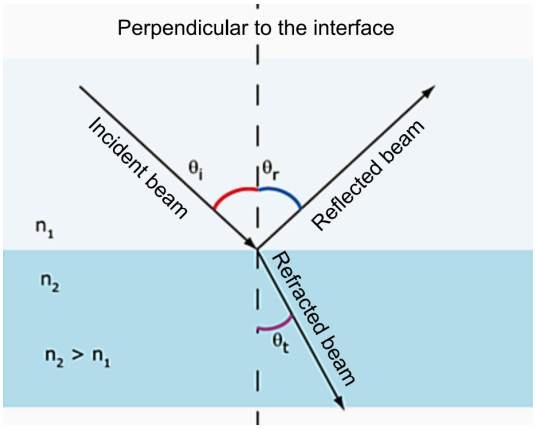

Figure 2.8: Schematic view of transmission, reflection, and absorption [37]

light, restricting it to a solitary path. Due to the thinness of the core, light travels through the cable with minimal refraction angles, resulting in the light covering the same distance as the actual fiber length. Consequently, single-mode fibers offer quicker signal transmission compared to multi-mode fibers and experience less dispersion delay [35]. Figure 2.7C demonstrates how the light travels through single and multi-mode fiber optic cables and how the dispersion occurs for different index types of fiber optic cables. The end of fiber optic cables may have different connector terminations or flat or rounded ferrule finishes.

2.3 Refractive Index of Materials

Light, as well as other electromagnetic radiation, travel at a constant speed of 299,792.458 km/s in a vacuum, where no material medium is present. Speed of light in vacuum, c), is a universal constant and represents the maximum speed at which an electromagnetic wave can propagate. However, when light passes through a transparent medium, there occurs an interaction which leads to decrease in the speed of light. Refractive index (n) is a dimensionless parameter that quantifies the extent to which the speed of light in a vacuum exceeds its speed in a given medium. It is expressed as the ratio of the speed of light in a vacuum (c) to the speed of light in the medium (v):

$$n = \frac{c}{v} \tag{2.8}$$

It is essential to acknowledge that refractive index varies across different wavelengths constituting electromagnetic radiation. This variability is dependent on the specific electromagnetic radiation involved. This occurrence is commonly referred to as scattering. When light travels through one medium, such as air (refractive index of approximately 1), and encounters a different medium, such as glass (with a refractive index of approximately 1.5 in the visible range), this abrupt change in the refractive index results in various phenomena, including transmission, reflection, and absorption. When the light comes from a medium having low refractive index and transmits into a medium with higher refractive index as shown in Figure 2.8, the optical path of the incident light is determined by the Snell's Law shown in Equation 2.9.

$$n_1 \sin\theta_i = n_2 \sin\theta_t \tag{2.9}$$

where θ_i and θ_t are the angles of incident and refracted transmitted beams with respect to the axis perpendicular to the interface between two mediums, respectively.

Reflection can be quantified and assessed using a parameter called *reflectance*, which represents the ratio between the intensity of the reflected radiation and the incident radiation. Fresnel Equations provide a means to connect the reflectance with the refractive index in accordance with a specific relationship as floows [37].

$$R = \left(\frac{n_1 \cos\theta_i - n_2 \cos\theta_t}{n_1 \cos\theta_i + n_2 \cos\theta_t} \right)^2 \tag{2.10}$$

CHAPTER 3

EXPERIMENTATION

3.1 Experimental Setup

An experimental setup is constructed for the detection of the shaped of the liquid-gas interface. Consistent with the numerical study, a fiber optic interferometric setup is employed for this purpose. The fiber optic interferometer in this thesis is a modified version of an existing setup which was originally designed and constructed to measure clearances of the order of micrometers covered with thin engine oil films, encountered in piston-cylinder configurations [38]. The system consists of (i) optical unit containing the optical components of the fiber optic interferometer, (ii) mechanical stage covering the test region which gas-liquid interface is investigated, (iii) data acquisition system which records the experimental data, (iv) optical table, (v) camera and (vi) reflective test pieces on which films of liquid are spread. Figure 3.1 shows the overall view of the fiber optic interferometer setup. All the optical components, the data acquisition system, except the computer recording the experimental data, and the mechanical stage (except the DC power supply) are located on an optical table to avoid external vibration effects.

3.1.1 Optical Unit

In the optical unit, the fiber optic interferometer uses a laser source which provides monochromatic light at the wavelength of 1550 nm, a fiber optic isolator positioned at the laser source's outlet, aimed at diminishing the occurrence of back-reflected beams originating from the other optical elements towards the

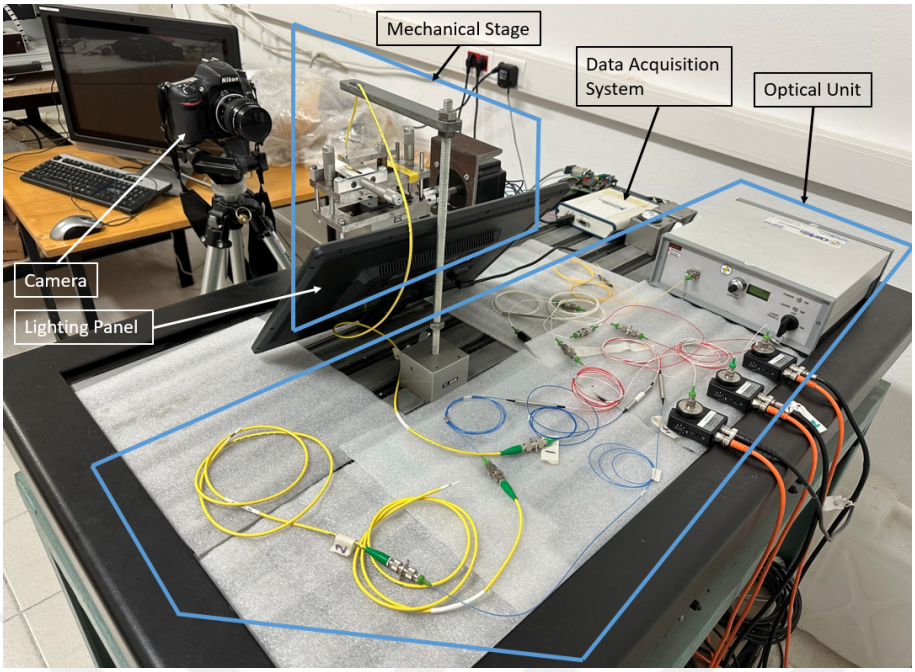

Figure 3.1: Fiber optic interferometer setup

laser source, three fiber optic beam splitters responsible for partitioning the optical intensity of the laser into four identical beams, three circulators, which are used for guiding the laser beam from the laser source to the mechanical stage and then directing the recombined interference beam from the mechanical stage to the photodetectors, three photodetectors that convert the optical output into electrical signals and send the signals to the data acquisition system, fiber optic cables operating in the wavelength range of 1300–1550 nm, and connectors between the optical components. The schematics of the experimental setup is illustrated in Figure 3.2. The details of the optical components are given below:

(1) Laser source: A 1550 nm laser, Oz Optics HIFOSS (highly stable laser diode source) distributed feedback (DFB) laser is employed in the experimental setup. One end of this laser source has a flat connector, and the other end has an angled polished connector, known as FC/APC receptacle. This receptacle serves the purpose of minimizing transmission loss that may occur when connecting the laser source to a fiber optic cable. Further details regarding the laser source's specifications can be found in Appendix A.1.

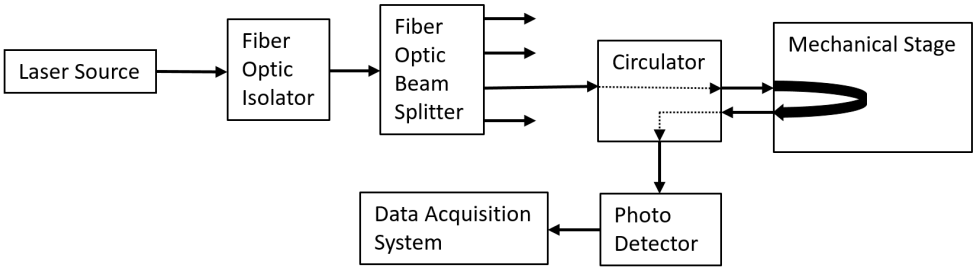

Figure 3.2: Schematic representation of the experimental setup

(2) Fiber optic isolator: A 1550 nm Oz Optics polarization insensitive fiber optic isolatori as shown in Figure 3.3A is used in the setup. The isolator is equipped with angle FC/PC connectors on both ends to minimize the transmission loss. The isolator is employed with the aim of reducing the extent of laser beam reflections from other optical elements that might otherwise return to the laser source. The specifications of the fiber optic isolator are given in Appendix A.2.

(3) Fiber optic beam splitter: An Oz Optics single-mode fiber pigtailed beam splitter is utilized (please see Figure 3.3B). The fiber optic beam splitter possesses a single input port and four output ports, enabling the division of the laser beam's optical intensity into four equivalent portions. Furthermore, it is furnished with angled FC/APC connectors on both terminations. For detailed specifications of the fiber optic beam splitter, please refer to the Appendix A.3.

(4) Circulator: The setup has Oz Optics fiber optic miniature circulators, which fulfilled dual primary roles: firstly, directing laser beams from the laser source to the mechanical stage, and secondly, guiding laser beams from the mechanical stage to the photodetectors, as seen in Figure 3.3C. These circulators are designed with a single input port and two output ports. The circulators are outfitted with angled FC/APC connectors on all of their ports. For detailed specifications of the circulators, please consult the Appendix A.4.

(5) Photodetector: In the setup, Thorlabs switchable gain detectors having a wavelength range of 800–1800 nm are integrated as the photo-detectors.

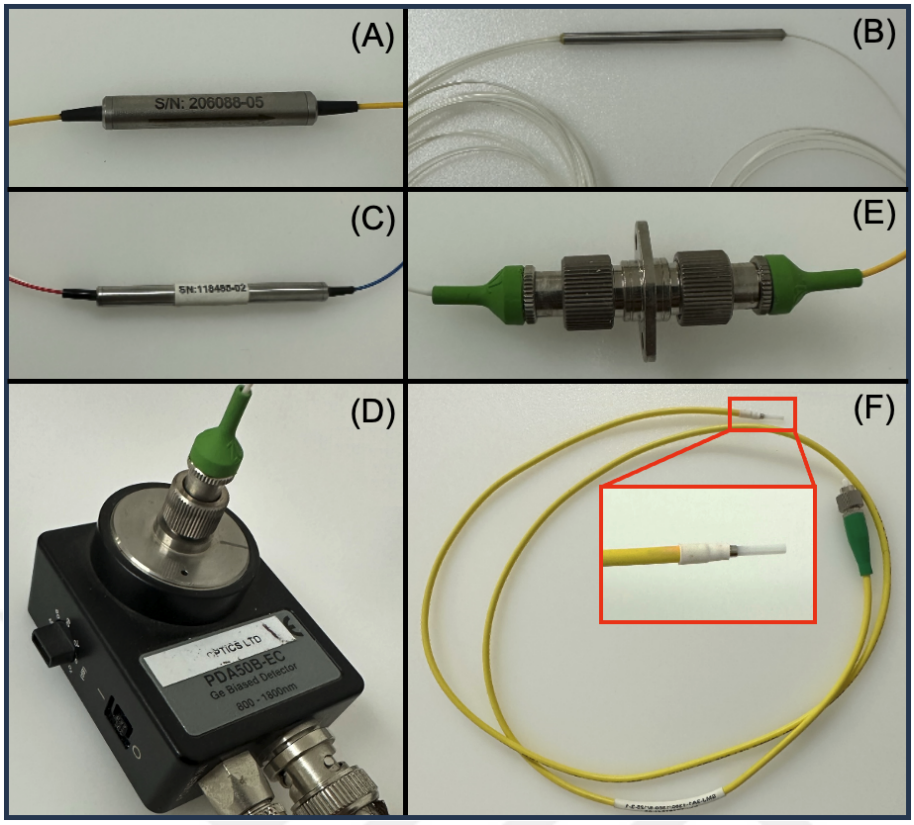

Figure 3.3: Components of the experimental setup: (A) Fiber optic isolator, (B) fiber optic beam splitter, (C) circulator, (D) photodetector, (E) connector, and (F) fiber optic cable and fiber optic probe.

The feature of switchable gain obviates the necessity for an amplifier circuit to enhance the optical outputs. These detectors transform the optical outputs obtained from the circulators into electrical signals, ranging from -10 to 10 V. Additionally, they are equipped with FC/APC adapters to ensure compatibility with fiber optic cables. For conveying the electrical signals from the photodetectors to the data acquisition system, BNC (Bayonet Neill-Concelman) connectors are utilized. Figure 3.3D shows the photograph of the photodetector. Detailed specifications of the photodetector can be found in the Appendix A.5.

(6) Connectors: This study employs flanged sleeve through connectors for polarization maintaining from Oz Optics. These connectors feature FC/PC connectors on both ends and serve the purpose of linking various optical

components through which the laser beams pass. The photograph of the connector is given in Figure 3.3E.

(7) Fiber optic cable: In this study, specialized single-mode fiber optic cables having the core to cladding diameter ratio of 9 μm to 125 μm from Oz Optics which operates within the wavelength range of 1300–1550 nm, are employed. One end of the cables features angled FC/PC connectors, while the other end has a flat polished ferrule. These ferrules are placed over the test pieces in the setup, which is referred as *fiber optic probe (FOP)* herein after. The fiber optic cable and the FOP can be seen in Figure 3.3D. Comprehensive details outlining the specifications of the fiber optic cable are provided within the Appendix A.6.

3.1.2 Mechanical Stage

The mechanical stage of the setup has a step motor, a DC power source supplying power to the step motor, a driver and a PIC card for step motor control, a lateral motion carriage providing lateral motion of the FOPs on the plate which carries the test object, a coupling for transmission of rotational motion of the step motor to the shaft of the lateral motion carriage, three magnetic bases fixing the step motor with the help of the step motor casing and the lateral motion carriage. The lateral motion carriage carries a FOP holder. Two micrometers are implemented to adjust the slope of the plate which carries the test object with the help of the clearance holes on the stationary plate.

The mechanical stage mainly consists of a step motor, a DC power source providing power to the step motor, a driver and a PIC card for controlling the step motor, a coupling transferring the rotational motion of the shaft of the step motor to the horizontal motion stage, test parts having reflective surface and different widths and the parts carrying the reflective test part and the FOP. To be able to move the reflective test part in the direction perpendicular to the probe motion in horizontal plane, there is also a second carrier controlled by a micrometer which is located on a horizontal motion slide activated by the step motor and operating in the perpendicular direction in the horizontal plane. The

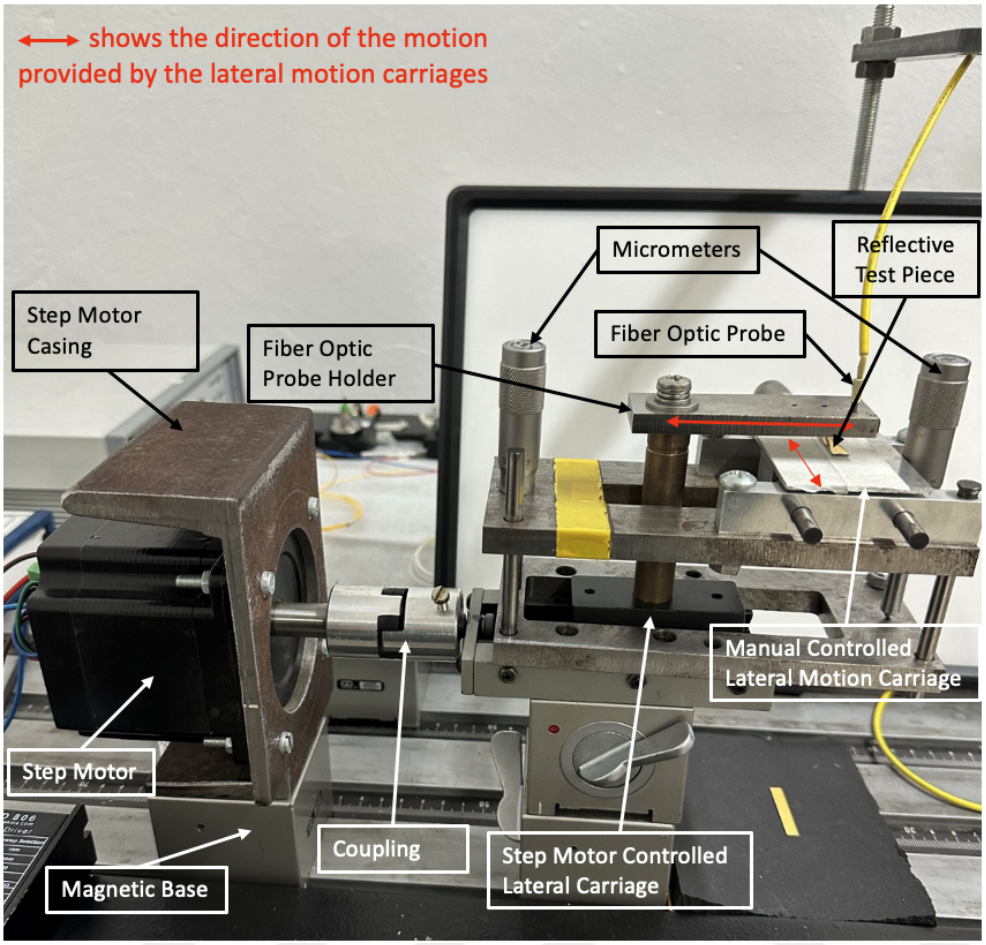

Figure 3.4: Mechanical stage

section covering the parts providing the motion of the FOP and test parts are shown in Figure 3.4.

(1) Step Motor: In the setup, lateral movement is attained by a step motor that produces a steady rotational motion. This motor is affixed to the optical table's magnetic base by ensuring stability through its casing. To transfer the rotational motion from the step motor's shaft to the lateral motion carriage, a coupling mechanism is utilized. Additionally, a rubber component is interposed between the coupling parts to mitigate the extent of transmitted vibrations. The step motor and its casing, magnetic base and coupling are demonstrated in Figure 3.4. The specifications of the step motor are given in Appendix A.7.

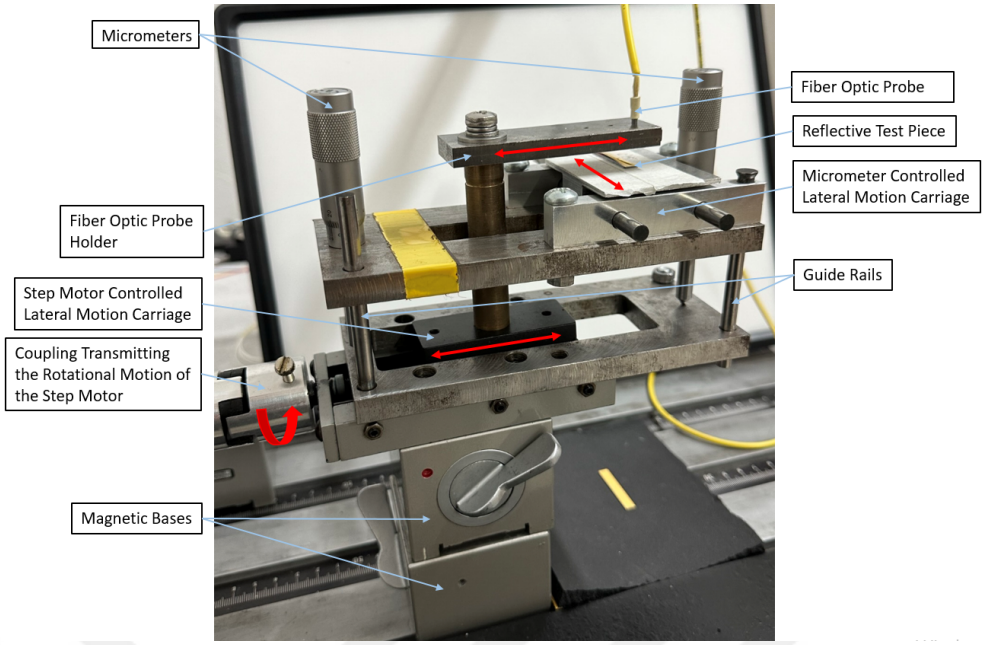

Figure 3.5: Step motor and micrometer controlled lateral motion carriages

(2) Power Source, Motor Driver and PIC Card: The power is provided to the step motor by a DC power source. A driver, which is controlled through a software installed in the computer with the help of a PIC card, is used to drive the step motor. The software enables the users to set the number of revolutions and the direction of the motion.

(3) Lateral Motion Carriages: The rotational motion of the motor is transmitted to the shaft of the lateral motion carriage with the help of the coupling, as shown in Figure 3.5. The lateral motion carriage controlled by the step motor moves the FOP holder forward and backward *via* the control software. Reflective test pieces are placed under the FOP on lateral motion carriage controlled by the micrometer. This carriage is located on a base whose tilt angle can be arranged by two vertical micrometers. The angle of this base can be changed with the help of the clearances of the guide rails located at its corners in a limited range. The lateral motion carriage controlled by micrometers can move the reflective test pieces in the direction perpendicular to the direction in which FOP moves. The directions of the motion of the components are indicated in Figure 3.5 with red arrows. The entire carriage structure is located on the magnetic bases

on the optical table.

3.1.3 Data Acquisition System

The data acquisition system covers a computer, a data logger sending the experimental data coming from the photodetectors to the computer to record, BNC connectors and data acquisition cables. The data coming from the photodetectors are transferred to the NI USB-4431 sound and vibration device via BNC cables. It has four input ports and one output port, and has simultaneous sampling rate capacity up to 102.4 kS/s. The signals coming from the photodetectors are digitized and sent to the desktop computer to be stored. The control of NI USB-4431 is realized by using MATLAB (2018b) software.

3.1.4 Optical Table and Camera

All the devices in the optical section and the mechanical stage are placed on an optical table whose dimensions are 70 cm $\times$ 120 cm $\times$ 20 cm. With the help of four pads on its corners, the vibrational effects are minimized. Figure 3.6 shows the photograph of the optical table. To be able to capture the photograph of the liquid profile during the experiments, a digital camera (Nikon D600 Digital SLR) together with an optical lens (Nikon micro-Nikkor 55 mm f/2.8) for acquiring for high-resolution photographs are used.

3.1.5 Reflective Test Pieces

Fiber optic interferometers are based on the theory of interference of light beams. In an interferometric setup, a reflective surface is an essential ingredient to create interference with the the beam reflected from the FOP tip. Therefore, a reflective test piece needs to be positioned under the FOP. In the experiments, the following reflective pieces are used: silicon wafer, gold-coated silicon wafer and polished stainless steel. To create a semi-cylindrical liquid, except for the minute deformation due to the effect of gravity, section in the direction of the



Figure 3.6: Optical table

motion of the FOP, the geometry of the reflective test pieces is generally selected as rectangular, with one side being sufficiently longer than the other one. The reflective test pieces used in the experiments are shown in Figure 3.7.

3.2 Experimental Procedure

As a first step, the computer is turned on and the control software programs are activated to control the data acquisition device and step motor. Then, the data acquisition device, DC power source, PIC card, the laser source and the photodetector are turned on. The reflective parts are placed on the mechanical stage, and positioned under the FOP holder. The short side of the reflective part is located in the direction of the motion of the FOP. The position of the camera used to observe the liquid shape is adjusted to see the liquid from the side view exactly. The purpose of usage of the camera is only for validation of compatibility of the numerical simulations with the experimental case. The camera is made ready to shoot before the step motor is activated to rotate by the specified number of turns to move the FOP over the whole section of the liquid on the reflective part. The number of turns of the step motor is controlled

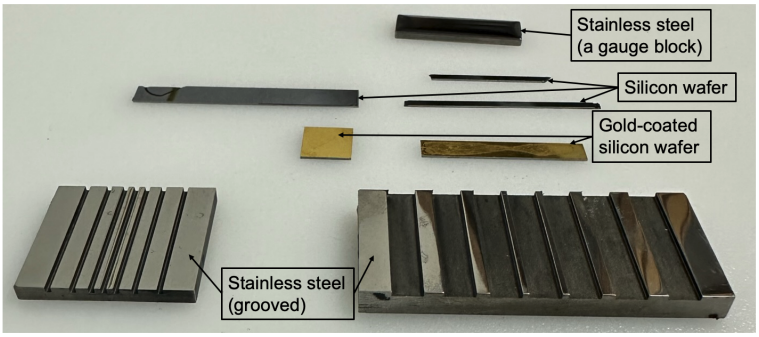

Figure 3.7: Reflective test pieces

by software. One turn of the step motor moves the FOP exactly 900 μm in the horizontal direction.

3.2.1 Determination of the Height of the FOP

The distance between the reflective test piece (positioned under the FOP) and the FOP tip can be adjusted with the help of two micrometers carrying the lateral motion carriage. Additionally, the FOP can be located at any point in a specific range in the vertical direction which the probe holder allows as shown in Figure 3.8. To accurately determine the distance between the tip of the FOP and the reflective surface, the experimental procedure begins with positioning the FOP at a high elevation, for example the FOP is moved upwards by reducing the distance between the tip of the FOP and the bottom surface of the FOP holder from d_1 to d_2 as shown in Figure 3.8. The reflective surface is then positioned in a close proximity to the FOP, such that the probe holder permits the FOP to make contact with the reflective surface upon its descent. After positioning the reflective surface near the FOP at a high elevation, and before starting to collect data, one needs to be sure that the FOP is outside one edge of the reflective surface so that along its movement, the FOP passes all over the liquid section.

The reflective test pieces need to be positioned in an almost exact horizontal position to realize the cases in the simulations. Therefore first, the FOP is moved horizontally over the reflective test piece by activating the step motor,

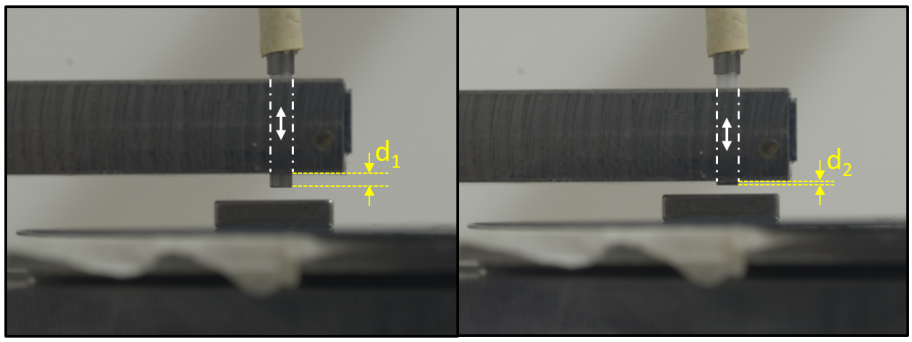

Figure 3.8: FOP holder: The FOP can be positioned in a specific range in the vertical direction which the probe holder allows.

aiming to establish a motion of the probe parallel to the top surface of the reflective piece and during which the data are recorded. To ensure a parallel alignment, two micrometers are utilized to control the lateral motion carriage, thereby enabling adjustments to the inclination of the reflective surface. Then, one of the micrometers which allows the reflective component to be positioned at different angles is adjusted to a slightly different setting than the initial one. The FOP is moved again over the reflective part and the data are recorded. The recorded data are analyzed and the fringe numbers are compared between the consecutive trials. The trial having lesser number of fringes is the one closer to the horizontal position. For different angles of inclination, the procedure is repeated until the case having the least number of fringes is achieved. It is known that while the optical path of the beam reflected from the FOP tip does not change, any increase in the distance between the tip and the reflective part also increases the optical path of the beam returning to the tip after reflection. Consequently, the interference of the beam reflected from the probe tip and the reflective part creates constructive and destructive interference patterns. These patterns are seen as fringes in the data. More fringes on the data mean more changes in the distance between the FOP tip and the reflective piece. An example of the experimental data collected at the beginning of the experiments while trying to obtain the horizontal position of the reflective part placed under the FOP is given in Figure 3.9. As it is seen in Figure 3.9, while in the case of high slope there are a lot of fringes, as the slope decreases, the number of fringes in the collected experimental data decreases. If no significant fringe occurs in

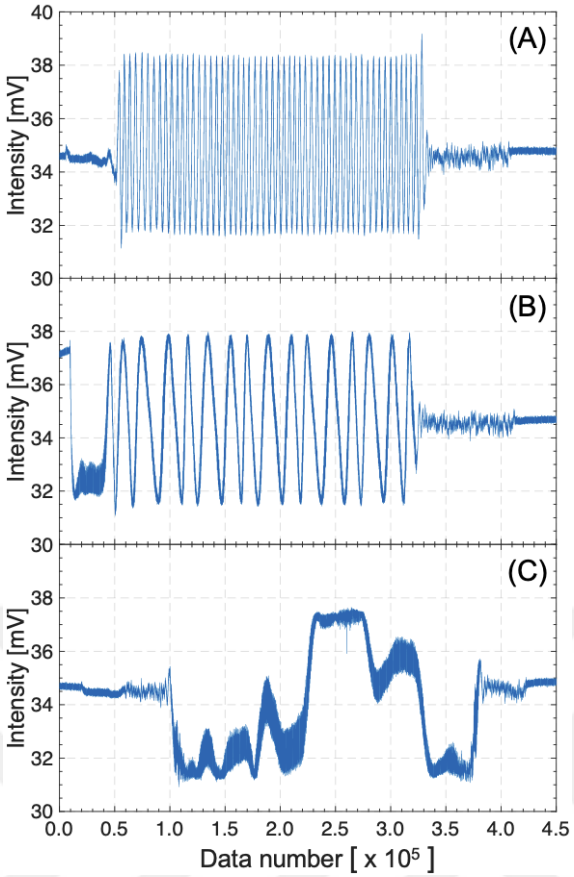

Figure 3.9: Recorded experimental data over engine oil on the gold-coated silicon: (A) High slope, (B) medium slope, and (C) no slope

the experimental data as in Figure 3.9C, the reflective surface is considered as in an almost exact horizontal position.

Actually, during the experiments, it is assumed that the FOP movement is exactly horizontal and at the beginning of the experiments the reflective part is adjusted such that it is positioned in a setting parallel to the direction of motion of the FOP. Once the parallel position is achieved, the FOP is lowered and positioned to make contact with the reflective surface as shown in Figure 3.10B. This setting is accepted as the zero reference point of the FOP height. Subsequently, the reflective piece is lowered to a lower elevation with an equal distance change in each micrometer controlling the lateral motion carriage. As a result, the distance between the tip of the FOP and the reflective surface is determined based on the distance change provided by the micrometers. The scale step of

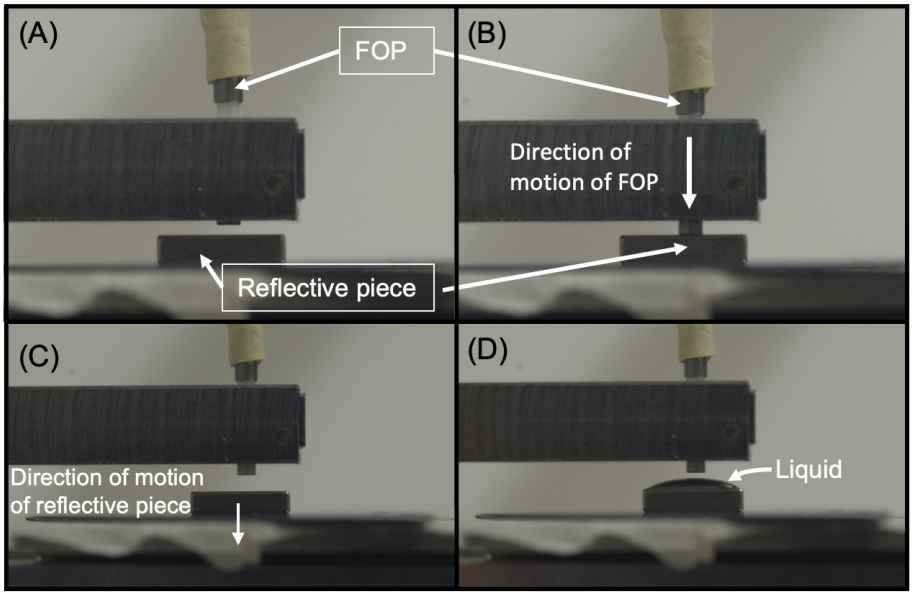

Figure 3.10: The procedure for adjusting the location of the FOP to zero height: (A) The reflective piece is brought to a nearly horizontal position and positioned at a height near the tip of the FOP. (B) The FOP is lowered and positioned to make contact with the reflective surface. (C) The reflective piece is positioned with the help of micrometers to maintain its horizontal position at a known distance from the tip of the FOP. (D) The experimental liquid is added onto the reflective surface.

the micrometers is 10 μm, representing the accepted resolution for the accuracy of probe height in the experiments. Once the reflective surface is positioned at a known distance from the tip of the FOP, the experimental liquid is added onto it. This procedure is shown in Figure 3.10.

Depending on the type of liquid, the initial amount is determined. For example, when using IPA, which is highly volatile, it is preferable to apply a large amount onto the reflective surface initially. This is because IPA evaporates quickly during experiments, causing the interface shape between the liquid and air to change between each experiment. This variability allows for obtaining different interface shapes in each experiment. However, when using engine oil, which is much less volatile, changing the interface shape requires adjusting the amount of oil in each experiment by adding or removing it. In the case of less volatile

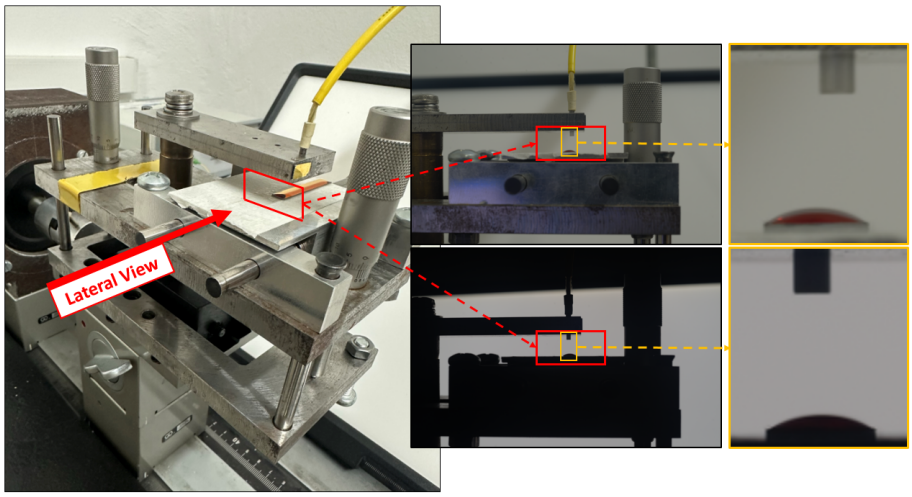

Figure 3.11: A focused photograph of the liquid film from the lateral view. The photograph was taken in two conditions, when the lightening panel is on and off.

liquids, applying a smaller amount, which is enough to wet the entire reflective surface initially, is preferable because adding liquid is an easier process than removing it from the reflective surface.

In Figure 3.11, a photograph of the liquid loaded on the reflective piece can be seen from the lateral view. As from the figure, the FOP passes over liquid which has a semi-circular cross-section in the direction of the motion of the FOP. To be able to capture the best contrast of the liquid film to detect the liquid profile, the photograph was taken in two conditions during the experiments, when the lightening panel is on and off.

3.2.2 Detection of Intensity Distribution of Laser Beam

To detect the intensity distribution of the laser beam leaving the FOP, the probe is moved horizontally, and the laser beam leaving the FOP is collected by another probe which is stationary and located under the moving FOP but this FOP is not connected to the laser source so that it only receives the laser beam and the intensity is measured by the photodetector. To be able to be sure that the probe moves over the center of the probe receiving the laser beam which

leaves the moving probe, the new designed horizontal slide carrying the droplet is moved by adjusting by the micrometer with 10 μm steps just before each experiment. When the experimental data are analyzed following the experiments, the experiment with highest intensity value is accepted as the one where the moving probe have passed over the center of the receiving probe. This procedure is repeated for the different distances between the moving probe and the stationary receiving probe. To arrange the distance between the probes, the level of two micrometers carrying the stage is changed equally, and hence the emitting angle of the laser beam leaving the probe is detected. Sample experimental data collected can be seen in Figure 3.12. It is can be clearly seen from the figure that there exists a Gaussian distribution in the intensity of the laser beam at the exit of the FOP. To determine the diameter of the laser beam at the distance where the data is taken by the receiving probe, it should be determined the left and right points of this distribution. According to the six sigma in statistics, in a Gaussian distribution three sigma deviation from the mean of the Gaussian distribution includes 99.73 % [39]. Therefore, six sigma range is an appropriate approach in our case to determine the limits of the experimental data.

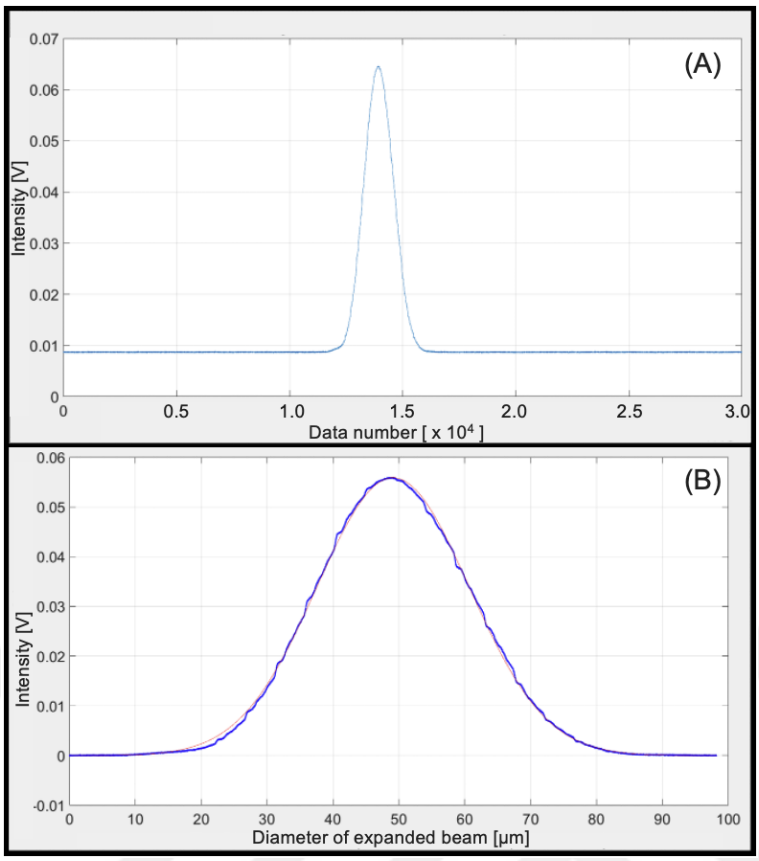

Figure 3.12: Sample experimental data collected by the stationary receiving probe: (A) Intensity distribution of the FOP, and (B) Gaussian fit to the experimental data

Once the limits of the data are detected and data number (i.e. the $x-$axis of Figure 3.12A) is converted to the distance value in µm by knowing the horizontal speed of the slide carrying the probe. A Gaussian distribution function given as:

$$f(x) = a \exp\left(- \frac{(x-b)^2}{2c^2} \right) \tag{3.1}$$

can be utilized to fit the data, where x is the distance travelled by the probe, a is the highest intensity value, b is the mean value of the distribution and c is the sigma value. The Gaussian curves fitted to the experimental data has R-squared values of 0.993 in the worst case scenario. An example of the curve fitted to the experimental data is shown in Figure 3.12B.

The resulting table presenting the probe height and beam diameter obtained

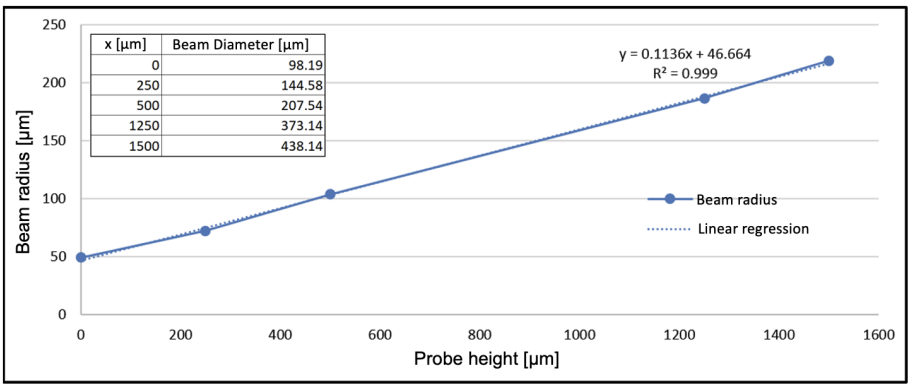

Figure 3.13: Beam radius vs probe height

from the experiments, along with the linear curve fit to the beam radius versus probe height, is shown in Figure 3.13. The lowest distance between the probes is considered as zero, with other distances evaluated relative to this reference position. Furthermore, the distances between the probes are now referred to as probe height. In this graph, it can be seen that a linear curve fits the data quite well, indicating the linear propagation of the laser beam. Additionally, the exit angle of the laser beam leaving the probe is calculated as 6.48° relative to the normal to the probe surface according to the linear fit. The acceptance angle is calculated as 7.47° by using the numerical aperture value of 0.13 specified in the technical data sheet of the FOP. This experimental results showed that the exit angle of the probe is not equal to the acceptance angle of the probe.

CHAPTER 4

MODELING OF LIQUID PROFILE *VIA* INTERFEROMETRY

In this section,how a fiber optic interferometer is implemented and how the experimental data are evaluated for the detection of liquid profile is explained in detail.

4.1 Thin Liquid Film Modeling

Interference simulations are realized for the detection of the profile of the thin liquid film on reflective test pieces. Interference data is collected as the FOP moves over the reflective test pieces. In order to handle the thin liquid film in interference simulations, the thin liquid film needs to be modelled numerically. For this purpose, a computer code was developed and implemented in MATLAB environment.

Surface tension induces a curvature at the interface between the liquid and the gas, leading to a pressure difference known as capillary pressure. In three-dimensional scenarios, surface tension generates two curvature radii. The capillary pressure is mathematically described by the Young-Laplace equation:

$$P_c = \sigma \left(\frac{1}{\mathcal{R}_1} + \frac{1}{\mathcal{R}_2} \right) \tag{4.1}$$

where σ is the surface tension, $\mathcal{R}_1$ and $\mathcal{R}_2$ are the principal radii of curvature. For a semi-circular cylinder one of radii goes to infinity so Equation 4.1 can be simplified as:

$$P_c = \frac{\sigma}{\mathcal{R}} \tag{4.2}$$

where $\mathcal{R}$ is the radius of curvature. Radius of curvature is:

$$\mathcal{R} = \frac{|1 + ((\delta')^2|^{\frac{3}{2}}}{|\delta''|} \tag{4.3}$$

Capillarity and gravity, in combination with surface tension, are the two phenomena that collectively influence the morphology of droplets or thin films. The Young-Laplace equation allows the expression of capillary pressure by substituting the term for the radius of curvature into Equation 4.2.

$$\Delta P = \frac{\sigma\delta''}{\left[1 + (\delta')^2\right]^{\frac{3}{2}}} \tag{4.4}$$

where the pressure jump at the interface is:

$$\Delta P = P_v - P_\ell \tag{4.5}$$

where P_v is the vapor pressure, P_ℓ is the liquid pressure, and δ .... To include the effect of gravity, the pressure jump term can be modified. In addition, the second derivative is observed to be negative for regular droplets. Hence, Equation 4.2 can be revised as:

$$\Delta P = -\frac{\sigma\delta''}{\left[1 + (\delta')^2\right]^{\frac{3}{2}}} + \rho g\delta \tag{4.6}$$

Equation 4.6 can be re-arranged as:

$$\delta'' = -\frac{\Delta P}{\sigma}\left[1 + (\delta')^2\right]^{\frac{3}{2}} + \frac{\rho g}{\sigma}\left[1 + (\delta')^2\right]^{\frac{3}{2}}\delta \tag{4.7}$$

This second-order boundary conditions requires two boundary conditions. Following boundary conditions can be applied [40]:

$$\begin{aligned} \delta(0) &= 0 \\ \frac{\partial\delta(0)}{\partial x} &= v(0) = \tan(\alpha) \end{aligned} \tag{4.8}$$

The first boundary condition dictates a zero film thickness at the initial point, and the second equation assigns the first derivative of the film thickness at the initial point as a contact angle. Using the method of reduction of order, the non-linear second-order ordinary differential equation given in Equation 4.7 can be solved. By assigning $\delta' = v$ and $\delta'' = v'$, one can obtain the two first-order coupled ordinary differential equations as:

$$\begin{aligned} \delta' &= v \equiv g\left(x, \delta, v\right) \\ v' &= -\frac{\Delta P}{\sigma}\left[1+v^2\right]^{\frac{3}{2}} + \frac{\rho g}{\sigma}\left[1+v^2\right]^{\frac{3}{2}}\delta \equiv f\left(x, \delta, v\right) \end{aligned} \tag{4.9}$$

These two equations can be integrated using available integration schemes in the literature. In this study, 4th–order Runge-Kutta (RK4) method is applied due to its superior accuracy. The numerical scheme of the RK4 method is implemented in a standard manner by specifying the desired height (h) which is the maximum film thickness, δ_{max}, and the width (w) of the liquid film, with the specified boundary conditions at Equation 4.8. The desired values of the height and width of the liquid represent the dimensional parameters of the gas-liquid interface geometry to be simulated. RK4 scheme is employed to iteratively integrate the set of equations until a specific criterion is met. For liquid film modeling, the numerical integration end when the film thickness reaches or falls below zero. An initial guesses are specified for the radius of curvature at the initial point to calculate corresponding unknown pressure and the contact angle. At the end of the first iteration, the difference of the height and the horizontal length of the liquid film with the desired values is checked for the specified max error values (10^{-6}) for both of these parameters. If the calculated error value exceeds the specified maximum error value for any of these parameters, a new combination of the radius of curvature term and the contact angle term is determined using the Newton-Raphson method in higher dimensions. Here, the system comprises two equations with two variables. The set of functions used to approximate the zero can be expressed as:

$$F(x,y) = \begin{pmatrix} f_1(x,y) \\ f_2(x,y) \end{pmatrix} = \begin{pmatrix} w_{\text{cal}} - w_{\text{des}}(x,y) \\ h_{\text{cal}} - h_{\text{des}}(x,y) \end{pmatrix} \tag{4.10}$$

where w_{cal} and w_{des} are the calculated and the desired value of the horizontal length of the liquid film shaped like semi-cylinder, respectively. In addition, h_{cal} and h_{des} are the calculated and the desired value of the height of the liquid film. In our case, x and y are the radius of curvature and the contact angle at the initial point, respectively. To find a better guess, x_{i+1} for the next iteration by using the current guess x, first-order Taylor-expansion of f_1 and f_2 around x

and y can be used:

$$\begin{aligned} f_1(x_{j+1}, y_{j+1}) =& f_1(x_j, y_j) + \frac{\partial f_1}{\partial x}(x_{j+1} - x_j) + \frac{\partial f_1}{\partial y}(y_{j+1} - y_j) = 0 \\ f_2(x_{j+1}, y_{j+1}) =& f_2(x_j, y_j) + \frac{\partial f_2}{\partial x}(x_{j+1} - x_j) + \frac{\partial f_2}{\partial y}(y_{j+1} - y_j) = 0 \end{aligned} \tag{4.11}$$

where x_{i+1} and y_{i+1} are the next iterations and the solutions of the following set of linear equations:

$$\begin{pmatrix} f_1(x_j, y_j) \\ f_2(x_j, y_j) \end{pmatrix} + J(x_j, y_j) \begin{pmatrix} x_{j+1} - x_j \\ y_{j+1} - y_j \end{pmatrix} \tag{4.12}$$

where J is the Jacobian:

$$J(x_j, y_j) = \begin{bmatrix} \frac{\partial f_1}{\partial x} & \frac{\partial f_2}{\partial x} \\ \frac{\partial f_1}{\partial y} & \frac{\partial f_2}{\partial y} \end{bmatrix} \tag{4.13}$$

By rearranging Equation 4.12, the next iteration, which represents the solution of the set of equations, is found as:

$$\begin{pmatrix} x_{j+1} \\ y_{j+1} \end{pmatrix} = \begin{pmatrix} x_j \\ y_j \end{pmatrix} - J(x_j, y_j)^{-1} \begin{pmatrix} f_1(x_j, y_j) \\ f_2(x_j, y_j) \end{pmatrix} \tag{4.14}$$

At the end of the iterations when the differences between the iterations for both the parameters of the radius of curvature and the contact angle decreases up to the specified max error, the iterations are finalized and a 4th–order polynomial is fit to the obtained liquid film shape. Additionally the polynomial constants and the fitting errors are calculated. The 4th–order polynomial provides a good fit with an R-squared value of 0.999 and higher.

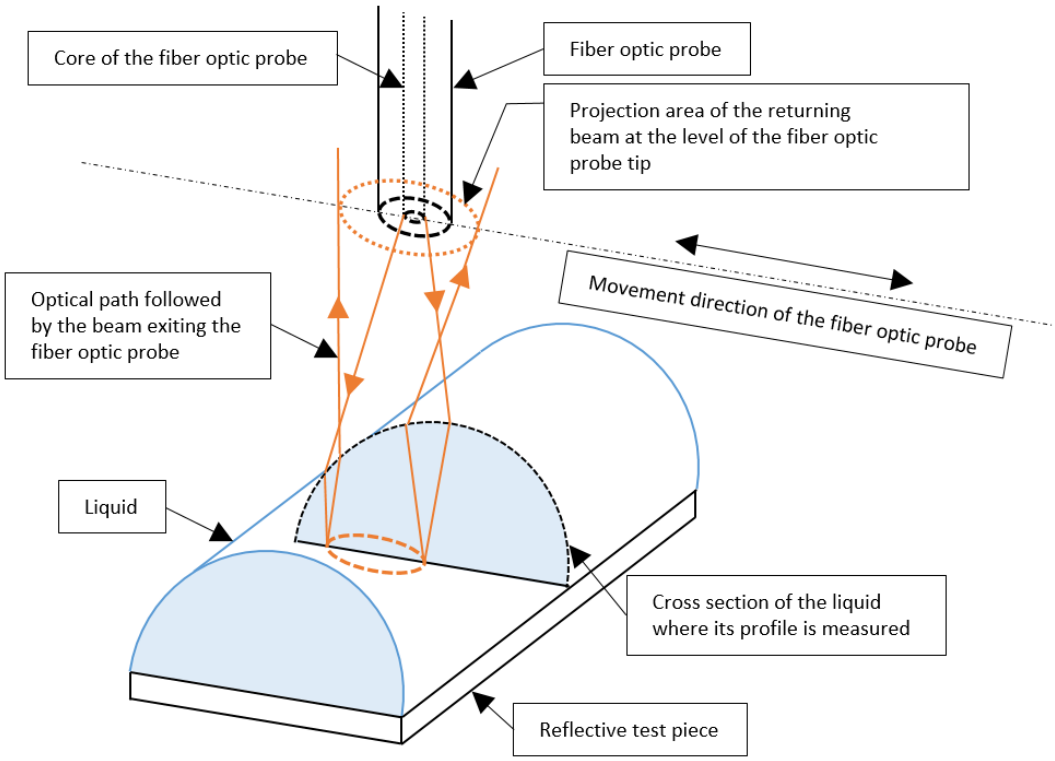

Figure 4.1: Schematic view of the test section

4.2 Interference Simulations

A fiber optic interferometer similar to Mach-Zehnder interferometer in terms of optical path structure is utilized for detection a liquid profile.Beam splitters and mirrors in Mach-Zehnder interferometer is replaced with the FOP tip in this experimental setup. The details of the experimental setup is already given in Chapter 3. Using the fiber optic interferometer, an interference phenomena is created with two beams having different optical paths. One beam is reflected from the FOP tip, another beam exits out from the FOP tip and returns back after passing through the liquid and reflecting from the reflective surface. During its path, the beam refracts and changes its direction due to the different refractive indices of the air and liquid. The FOP is moved along the liquid profile continuously. The interference pattern caused by the difference of the optical paths of two beams gives us the information about the liquid profile. Figure 4.1 shows the test section schematically. As seen in Figure 4.1, the light leaving the FOP has an exit angle and propagates conically. In this study, to simplify

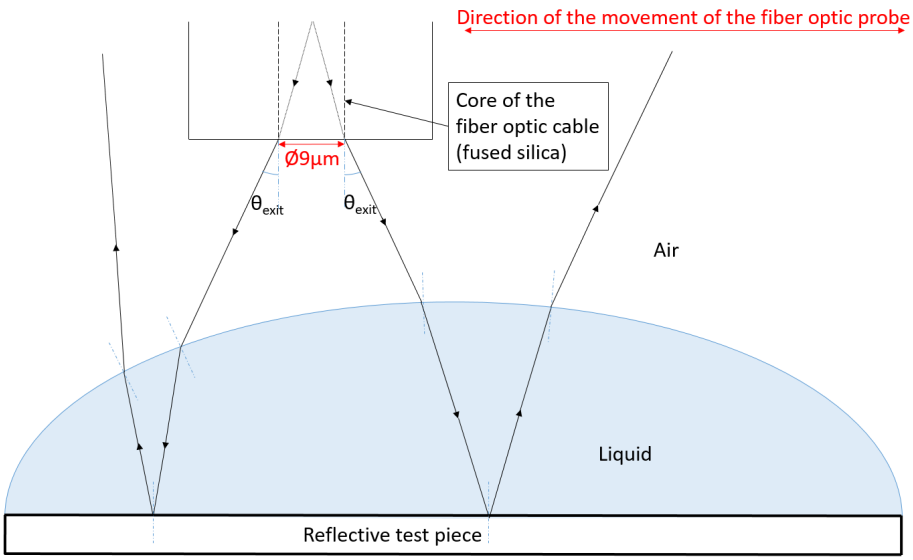

Figure 4.2: Beam coming out from the FOP and the path it follows where the FOP is at a location over the semicircular shaped liquid on the reflective test piece

the simulations, the interference phenomena is handled in 2-D cross-section in the movement direction of the FOP. Contribution of the beams reflecting in the other directions to the total intensity is accepted as ineffective due to the semi-cylindrical liquid geometry.

Single-mode fiber optic cables have a numerical aperture (NA) value provided by the manufacturer. However, when the NA value is used to calculate the angle of the cone of the light emitted from the FOP, a significant error can occur. Gaussian beam distribution approach at the exit of the FOP gives much more better results [41]. According to the specified numerical aperture value of 0.13, the acceptance angle of the FOP is 7.47° (NA=sin$\theta \longrightarrow \theta = \sin^{-1}(0.13) = 7.47°$). The experimental study which is performed to find the exit angle is explained in Chapter 3. The core of the fiber optic cable through which the light passes, used in this study, has a diameter of 9 µm (d_{probe}). The core material of the fiber optic cable is fused silica. Each material and air have different refractive indices.

Interference phenomena occurs with the beam reflected from the FOP tip and the beams coming out the FOP and returns back to the FOP after passing through

the liquid on the reflective test peace and reflecting from its surface. Figure 4.2 illustrates the schematic view of the path followed by the beams coming out from the FOP and the path it follows (note that the FOP is at a location over the semicircular shaped liquid on the reflective test piece in the figure). The beams come out from the core of the FOP whose diameter is 9 μm with an exit angle. The difference in the refractive indices of the media along the optical path causes the refraction. The core material of the fiber optic cable is fused silica which has a refractive index of 1.444 [42] for the wavelength of 1550 nm which is the wavelength of the laser used in this study. For the same wavelength, the air, the engine oil (Shell Risella X430) and IPA as a liquid on the reflective test piece have refractive indices of 1.0003, 1.4600 and 1.3738, respectively. Deionized water is also tested, but it failed to create a semi-circular cross sectional shape due to its low wettability with the reflective pieces used. The paths followed by the beams with the exit angle, located at the far left and right of the FOP, can be seen in the figure. They refracts at the interface of the liquid and air, and also from the reflective surface of the reflective test piece, and finally reach to the level of the FOP tip. Please note that Figure 4.2 only demonstrates a single location of the FOP over the liquid. The interference pattern necessary for identifying the interface shape between air and the liquid is achieved by displacing the FOP along the liquid section unidirectionally either to the left or right. To simplify the analysis of interference pattern, the movement of the FOP is kept in the direction exactly parallel to the surface of the reflective test piece, since the movement of the FOP with an angle with the reflective test piece creates extra fringes due to the change in the distance between the FOP tip and the reflective test piece in addition to the change in the optical path caused by the liquid having different refractive index with respect to the air.

The beams exiting from the FOP tip follow different paths in a conical region inside the angles of $+\theta_{\text{exit}}$ and $-\theta_{\text{exit}}$. The beams following different paths have different effects on the total interference. To determine the separate and cumulative effect of the each beam, the FOP surface is discretized to generate slices. In each slice, the optical paths are determined for the beams at the far left and right. The exit angle of the beams of the FOP is known but the exit

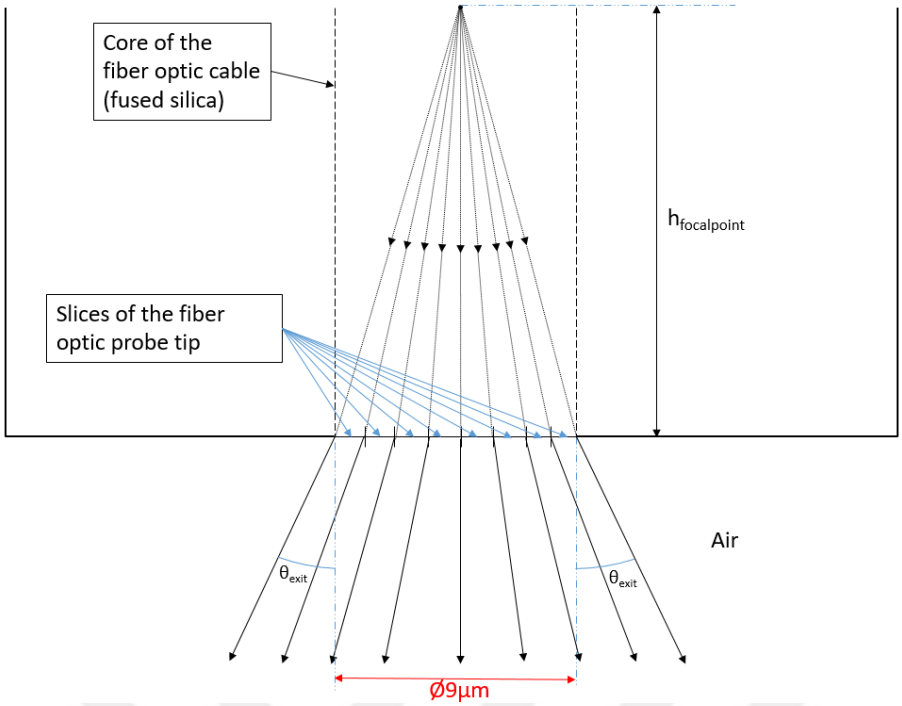

Figure 4.3: A schematic view of the beams coming out from the slices from the surface of the FOP tip in one position of the FOP

angles of the beams in the slices are need to be determined. To determine them, firstly the distance between virtual focal point and the FOP tip, $h_{\text{focal-point}}$, is calculated with the help of the beams at far left and right, whose exit angles are known. Then, the paths of the each beam emitted from the virtual focal-point and passing through the points at the far left and right in each slice are determined by applying Snell's Law using the refractive indices of the media (fused silica and air at the FOP tip). A schematic view of the beams emanating from the discretized slices on the surface of the FOP tip is shown in Figure 4.3. The number of the slices on the surface of the FOP tip affects the resolution of the total intensity of the interference simulations. More slices lead to higher resolution. In addition to the leftmost and rightmost beams coming out of each slice, one more beam is sent from the middle points of the slices, and the optical paths followed by the beams coming out of that slice are also calculated. The calculated optical path of the beam passing through the middle point of each slice is accepted as the optical path of the beam coming out from that slice while calculating its contribution to the total intensity. Moreover, it is also known that

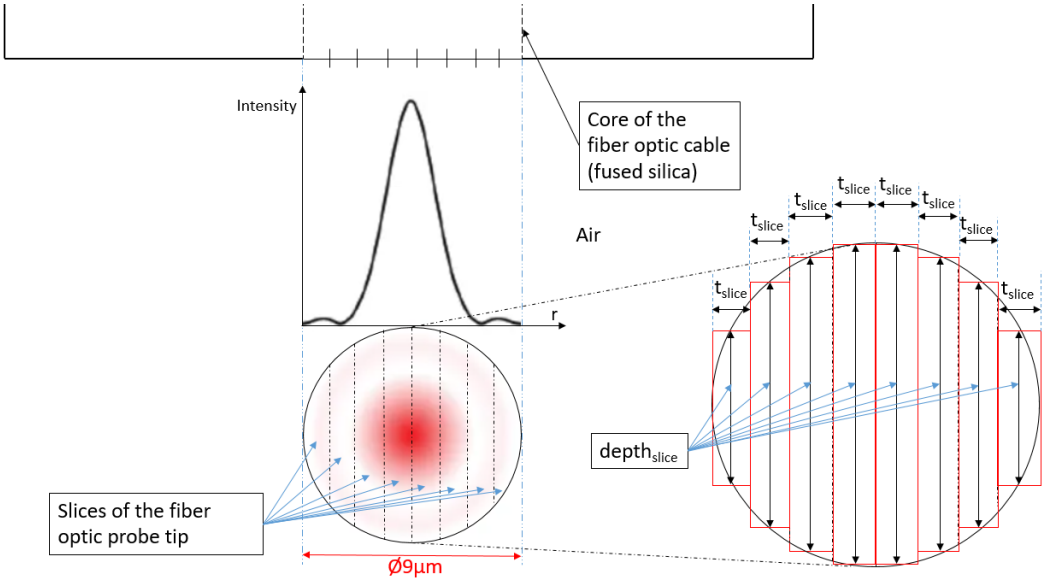

Figure 4.4: Gaussian distribution of intensity and the slices at the FOP tip [43]

the intensity of the light at the exit of the FOP has a Gaussian distribution, so the distribution of the intensities which the beams coming out have is calculated for each slice, separately.

Figure 4.4 demonstrates the Gaussian distribution on the surface of the FOP tip. As seen, the area of the slices are calculated by rectangular approach. Each slice has specified thickness according to the desired resolution level. The depth of the slices is accepted as the depth value at the mid-section of each slice. The area of slices are required in the calculation of the total intensity, and obtained by multiplying the depth and thickness of each slice. The beams exiting the FOP is refracted when they pass through the liquid. To determine the path of the refracted beams, the surface normal at the intersection point is determined by using the 4th–order polynomial fitted to the simulated thin liquid film. After the detection of the surface normal at the intersection points of the beams at the interface, Snell's Law is applied to determine the path of the beams.

The beams refracted at the liquid interface, travel through the liquid and reflect back from the surface of the reflective test piece. At this point, the angle between the incoming beam and the surface normal is calculated, and this angle is used as the angle of reflection. After the reflection from the surface of the reflective

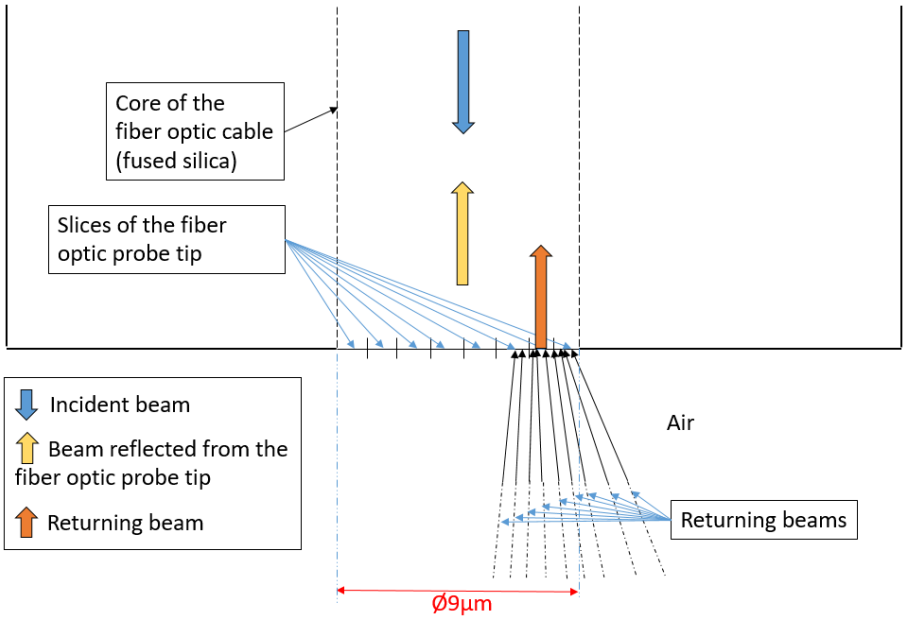

Figure 4.5: Three beams creating the interference at the FOP tip

test piece, the beams again refract at the air-liquid interface, and the angles of refraction are calculated by determining the surface normal at the intersection point on the liquid thin film. Again, the surface normal is found by using the 4th–order polynomial fitted to the simulated thin liquid film, and then with the help of Snell's Law, the path of the beams emerging from the liquid is determined. Finally, the beams emanating from the liquid reach to the level of the FOP. Each slice is checked for the returning beams that impinge, and the contribution of the returning beams to the interference is determined. Figure 4.5 shows the returning beams after passing through the liquid film and reflecting from the reflective test piece, the beam reflecting from the FOP tip and the incident beam for one position of the FOP. The interference occurs as a result of the interference of the returning beams and the beam reflecting from the FOP tip.

The returning beams may not return to all of the slices at the FOP surface as shown in Figure 4.5. In the each position of the FOP, each slice is investigated separately to control how many beams return, and the contribution of the individual beams returning to the slices are accounted for in the calculation of the total intensity. In each slice, the intensity is determined by the following

interference equation. In the slices where no returning beam is incident, Equation 4.15 is still valid and in these slices, the intensity is only created by the intensity of the beam reflected from the FOP tip. For all slices, the intensity of the beam reflected from the FOP tip is constant, and its optical path does not change in any case. Therefore, the beam reflecting from the FOP tip is the reference beam and its phase is evaluated as zero. The total intensity values for each slice in each step of the FOP are calculated by using Equation 4.15.

$$\begin{aligned} I_{\text{slice}} =& I_{\text{tip}} + I_{\text{rtn1}} + I_{\text{rtn2}} + I_{\text{rtn3}} + ... + I_{\text{rtnN}} \\ &+ 2\sqrt{I_{\text{tip}} I_{\text{rtn1}}}\cos(-\phi_1) + 2\sqrt{I_{\text{tip}} I_{\text{rtn2}}}\cos(-\phi_2) + 2\sqrt{I_{\text{tip}} I_{\text{rtnN}}}\cos(-\phi_N) \\ &+ 2\sqrt{I_{\text{rtn1}} I_{\text{rtn2}}}\cos(\phi_1 - \phi_2) + 2\sqrt{I_{\text{rtn1}} I_{\text{rtn3}}}\cos(\phi_1 - \phi_3) + ... \\ &+ 2\sqrt{I_{\text{rtn1}} I_{\text{rtnN}}}\cos(\phi_1 - \phi_N) \\ &+ 2\sqrt{I_{\text{rtn2}} I_{\text{rtn3}}}\cos(\phi_2 - \phi_3) + 2\sqrt{I_{\text{rtn2}} I_{\text{rtn4}}}\cos(\phi_2 - \phi_4) + ... \\ &+ 2\sqrt{I_{\text{rtn2}} I_{\text{rtnN}}}\cos(\phi_2 - \phi_N) + ... \\ &+ 2\sqrt{I_{\text{rtnN}-1} I_{\text{rtnN}}}\cos(\phi_{N-1} - \phi_N) \end{aligned} \tag{4.15}$$

where I_{slice} is the total intensity created due to the interference of the beams returning to the FOP and reflected from the tip of the FOP, I_{tip} is the intensity of the beam reflecting from the FOP tip, I_{rtn} is the intensity of the returning beam and N is the number of the beams returning to the FOP. The phase angle, ϕ, terms are $-2\pi r/\lambda$ as explained in Equation 2.1. It should be noted that the optical path is not the physical distance travelled by the beam. The optical path can be calculated by using the following relation [44]:

$$OPL = n \times d \tag{4.16}$$

where OPL is the optical path length, n is the refractive index of the medium through which the beam passes and d is the physical length of the path followed by the beam in the medium. In different media the optical path length is evaluated with this relation.

The intensity for each slice is numerically integrated over the probe surface to

calculate the total light power measured by the photodetector. Figure 4.4 shows how the area of each slice is handled. The intensities of the beams are affected by the difference between the refractive indices of the media through which the beams pass, reflect and the expand. The effects of the refractive indices of the media are calculated by using Fresnel equation given in Equation 2.10. For example, when the incident beam coming through the fiber optic cable reaches the tip of the FOP, the medium through which the beam passes changes from the fused silica to air. The incident beam impinges on the surface of the FOP tip with zero angle with respect to the surface normal, so the angle of the transmitted beam with respect to the surface normal becomes zero according to Snell's Law given in Equation 2.9. As a result, the reflectance can be obtained by using Equation 2.10 ($n_1 = 1.444$ for fused silica) and $n_2 = 1.000$ for air) as 3.3%. This means that the beam reflected from the FOP tip has an intensity equal to 3.3% of the intensity of the incident beam. The beam coming out from the FOP tip has the remaining part of the intensity that is 96.7% of the intensity of the incident beam. Similar calculations are performed when the light travels through the interface between any two media.

The beams reflect from reflective test pieces with smooth metallic surfaces, and the reflectance values assumed in the simulations of these surfaces are adjusted according to the comparison between the intensity results in simulations and experiment beacuse reflectance depends on various factors such as the material, surface roughness, quality of coating, cleanliness of the surface, etc., which can be challenging to detect. The decrease in the intensity of the beams due to the expansion is inversely proportional to the distance from the center of a hypothetical sphere located in the tip of the FOP. This effect is accounted for in the simulations. In addition, in the simulations a correction factor is defined to take into account the uncertainties in the reflectance value as well as the beam expansion loss to match the simulation and experimental results. Finally, the total power of the light which is detected by the photodetector is obtained by summing the powers of the returning beams calculated for each slice. The calculated power is only for one position of the FOP. In each step of the FOP all calculation process is repeated, and the power of the light occurring due to

the interference of the beams during the motion of the FOP is obtained. As expected, smaller steps improves the resolution of the results at the expense of increased computational time.

CHAPTER 5

DATA ANALYSIS AND RESULTS

In this chapter, data obtained from the experiments conducted by moving the FOP over the liquid film located on the reflective rectangular test piece in the direction parallel to its short side are investigated and analyzed. The method for comparing the simulations performed for the given FOP height, the liquid height, and the liquid width, with the experimental data taken for the liquid film under the same conditions, is explained.

During the experiments, liquid-air interference is detected as intensity data and recorded on the computer. Simultaneously, photographs of the test section in the lateral direction are taken. The information about the liquid film's geometry is obtained from the photographs by using parametric drawing tools. The parametric drawing tool enables the determination of the height of the FOP, as well as the height and width of the liquid film within a specific range. The width of the reflective test piece, measured by a caliper, serves as the reference dimension. A micro-lens equipped camera is used to obtain a clear side view of the liquid profile, and the measurement of the variation of the liquid-air interface is determined within a certain range on the photograph. The micro-lens camera is arranged to a position in the same direction with the top surface of the reflective test piece and the image on the near vertical surface of the reflective test piece is focused. The aim is to detect the height of the liquid on the reflective test piece with the best accuracy from photographs. Although the optical axes of the camera and the horizontal plane of the reflective test piece are aligned, due to the uncertainty of the difference between positioning of the camera relative to the reflective test piece, the optical axis of the camera can only be aligned

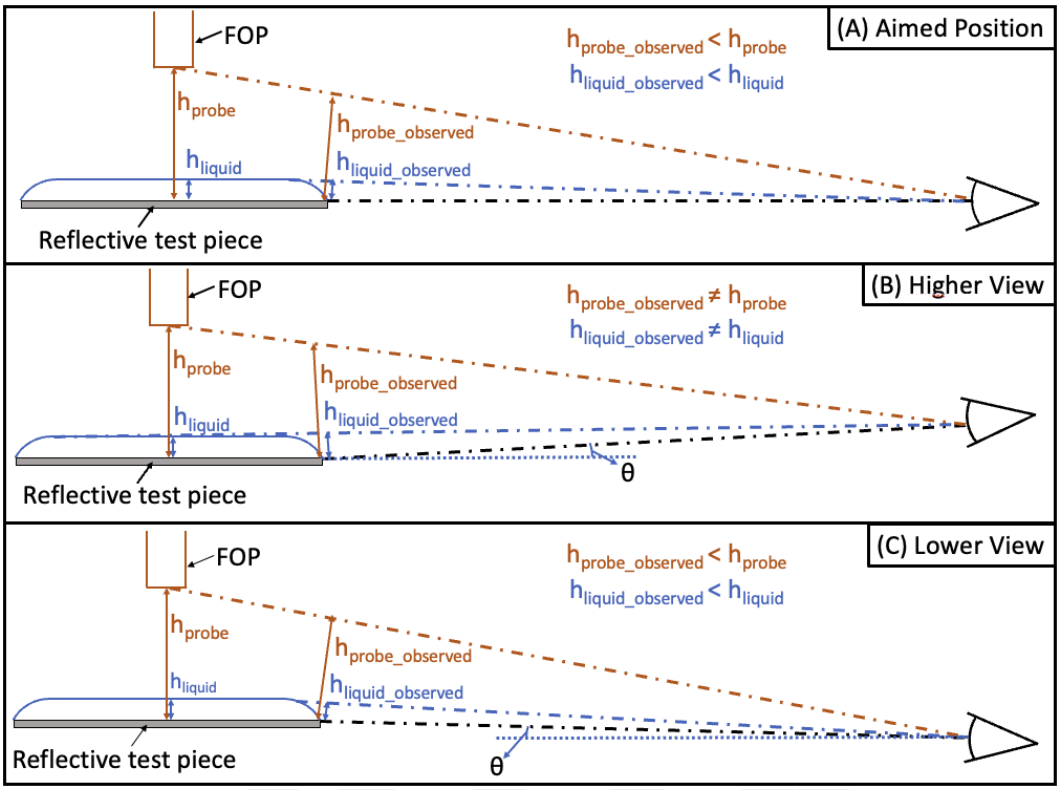

Figure 5.1: (A) Schematic view of aimed position of the observation by the camera. Perspective view may cause a deviation between the actual and observed dimensions. Schematic view of the position deviated from the aimed position of the camera. Positioning the camera (B) above or (C) below the targeted position causes an extra difference between the observed and actual values of the FOP and liquid heights.

within a tolerance, resulting in a higher or lower camera position [Figure 5.1]. This results in two sources for error. The first one is an error due to perspective, even if the camera is perfectly located at the aimed position [Figure 5.1A]; and the second one due to the camera being positioned on a higher or lower plane [Figure 5.1B and C]. Therefore, the dimensions of the FOP and liquid heights measured from the photographs and the actual values differ, due to the incurred error. Moreover the incorrect positioning of the micro-lens camera in the horizontal direction causes the width of the reflective test piece—which determines the liquid width—to be observed larger than its actual value as shown in Figure 5.2.

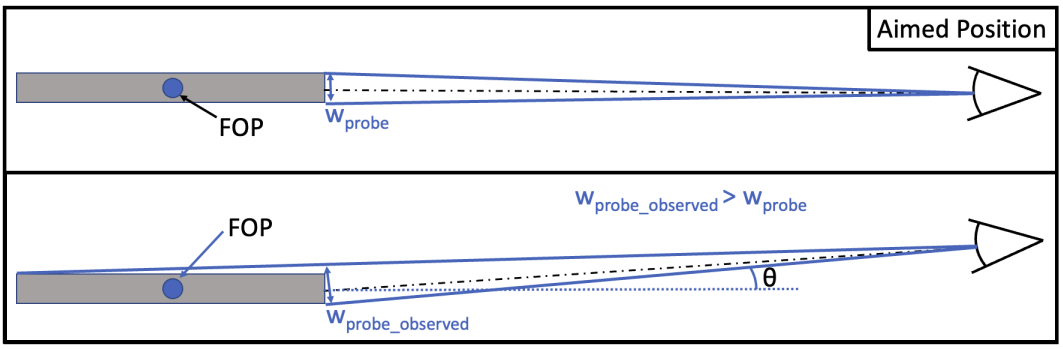

Figure 5.2: Schematic view of the incorrect positioning of the micro-lens camera in the horizontal direction. This case causes the width of the reflective test piece which determines the liquid width, being observed larger than the actual value.

In addition to the perspective view and the incorrect positioning of the micro-lens camera which causes the test parameters to be observed different than the real ones—since the camera focuses only on a single plane and the narrow depth of field of a micro-lens—the fine details in the depths of the images used to determine the test parameters are blurred. For these reasons, the dimensional test parameters obtained from the photographs taken by the camera are used to determine only the values close to the actual dimensions.

There are many parameters affecting the intensity of the interference. Mainly three geometrical parameters which are the height of the FOP, which is the distance between the FOP tip and the top surface of the reflective piece, the height and the width of the liquid film affect the intensity of the interference. Some of the other parameters affecting the results are the refractive indices of the mediums though which the beams pass, reflectance of the reflective test pieces on which the liquid is put, the sensitivity of the photodetector, the surface tension of the liquid, temperature and humidity of the air.

Intensity data include fringes in the specific range of the movement of the FOP over the liquid. In order to take a measurement, the beams reflected from the reflective test piece must pass through the liquid and return to the FOP. If a beam does not return back to the FOP, interference does not occur. In cases where the slope of the liquid surface is above a certain angle, the rays do not return to the FOP. Therefore, interferometric measurement takes place in a

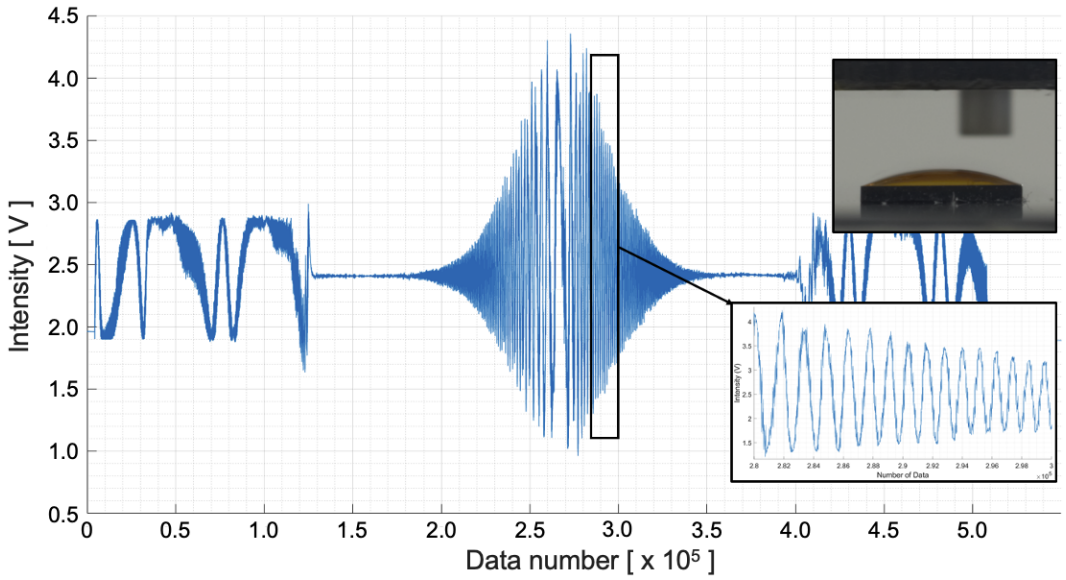

Figure 5.3: Experimental data of the engine oil on the gold-coated silicon wafer

certain range close to the peak of the liquid where the slope is low.

Now let us look at the experimental data taken over the engine oil (Shell Risella X430) on the gold-coated silicon wafer which is used as a reflective test piece.

Figure 5.3 shows the experimental data with numerous fringes. The photograph of the test section is also shown on the plot. As it is seen there is almost a symmetric plot due to the symmetric geometry of the liquid film along the direction of the probe motion. Fringe frequency decreases around the middle point due to the slow change of the slope of the air-liquid interface around that region in the direction of the FOP. However the intensity increases up to the middle point since the number of beams returning to the FOP increases at that region again due to low slope of the air-liquid interface.

After the experimental intensity data are obtained, in order to determine the liquid geometry along the direction in which the FOP moves, simulation trials are needed to find the experimentally measured parameters such as the probe height and the height of the liquid film. The best fit of the simulation result to the experimental data determines the conditions in which the experiment was performed.

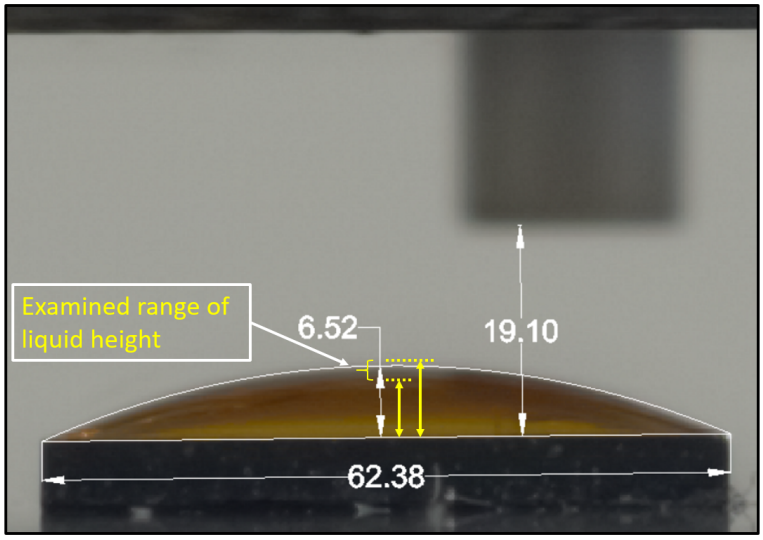

Figure 5.4: Dimensions of the test section covering the probe height, the height and the width of the liquid film

Firstly to validate the simulations, the dimensions of the test section are determined by using the photograph of the test section taken in the lateral direction. As reference, the width of the gold-coated silicon wafer which is measured by a vernier caliper is used. Figure 5.4 shows the dimensions on the photograph of the test section, which are obtained by using the parametric drawing tool. The measured value of the width of the test piece on the drawing is 62.38 drawing units and the width measured by the caliper is 5.04 mm. Therefore 0.0808 mm (5.04 mm/62.38) is used as the scale to determine the other dimensions on the photograph. For example the dimension of the probe height is 19.10 drawing units on the photograph. The corresponding metric dimension is calculated as 1.54 mm (19.10×0.0808).

Due to the fact that the interface line appears blurred, the largest and smallest possible values of the parameters are determined on the photograph. Figure 5.4 shows rough estimates to the possible dimensions on the photograph.

By using the possible limits of the dimensions, the interference simulations are made in the range determined for the parameters. Additionally other parameters needed in the simulation such as the refractive indices of the media, the reflectance of the reflective surface and the surface tension of the liquid are de-

termined from the studies in the literature and the technical data sheets of the suppliers.

The significant uncertainties in the dimensions on the photograph are for the width and the height of the liquid film. Uncertainty in the height of the FOP is not a source of a major uncertainty in the experiments because, as explained in subsection 3.2.1, the probe height can be adjusted with high accuracy with the help of micrometers. Considering the case given in Figure 5.4, the maximum and minimum values determined for the width of the liquid film are 5.35 mm and 4.77 mm, respectively. Additionally the maximum and minimum values determined for the height of the liquid film are 0.62 mm and 0.45 mm, respectively and also the maximum and minimum values determined for the height of the FOP are 1.57 mm and 1.47 mm, respectively. However, the measurement by the caliper of the width of the gold-coated silicon wafer gives the true value as 5.04 mm and the reflective test piece has very sharp edges so the liquid wets the entire surface. As a result the width of the liquid is taken to be 5.04 mm in the simulations. Moreover, the height of the FOP, controlled by the micrometers, is measured as 1.50±0.01 mm. The simulations are performed in the specific ranges of the height of the liquid film and the height of the FOP to find the best fit to the experimental data. For this case the height of the FOP was simulated for three values namely, 1.49 mm, 1.50 mm and 1.51 mm. The simulations were made for twelve values spaced equally between 0.40 mm and 0.62 mm for the height of the liquid film. In the range of simulations, a minimum value of the liquid height less than the minimum value measured from the photographs was used to account for the possible incorrect positioning of the micro-lens camera. The maximum value of was taken as the value detected on the photograph because the micro-lens camera was placed by ensuring that it is not below the top surface of the reflective test piece. The aim of the simulations is to find the best fit to the experimental data among the parameters in the determined ranges for them.

5.1 Comparison of Experimental and Simulated Data

5.1.1 FFT

While comparing the simulated and experimental results, firstly FFT of the both data are analyzed in specific ranges of the data, since the frequency of the intensity data is strictly related to the shape of the liquid film. To determine the shape of the liquid film by performing simulations, the simulation case which fits the experimental data the best in terms of frequency needs to be found. FFT determines the entire range of frequencies in the data together with their amplitudes. The experimental data show a continuous increase in the values of the frequencies towards the sides of the liquid film. To compare the simulated and the experimental data, FFT is applied in incrementally, in discrete sections of the experimental and simulation data. FFT analyses were investigated for only one half of the liquid film due to its symmetric shape. The dominant frequencies in each range were determined and used for comparison.

The discrete sections individually analyzed by FFT are wider near the center of

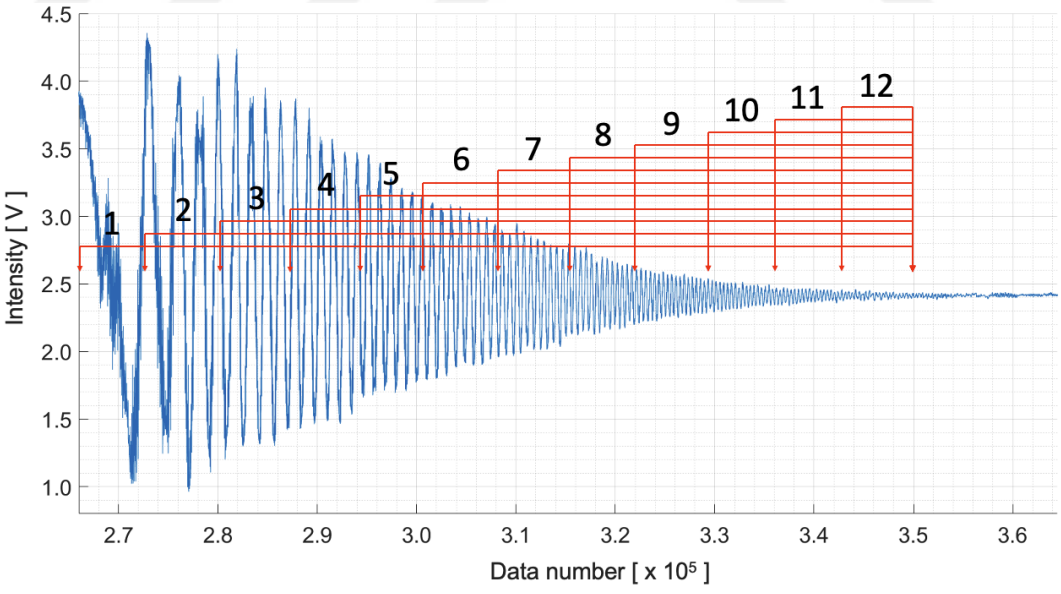

Figure 5.5: The variable width slices used in FFT analysis for the right side of the experimental data collected with the engine oil on the gold-coated silicon wafer

the liquid film and are gradually reduced in width towards the liquid-air-solid triple line where the liquid film ends. This is needed, since around the middle of the symmetric shape of the liquid the dominant frequencies of the interference fringes are low and therefore, higher resolutions for frequencies are needed in this range. To be able to increase the resolution of the frequencies determined by FFT, the discrete data slices around the data with low frequencies are kept wider. As an example Figure 5.5 shows twelve variable width slices used in FFT analysis of a sample case.

To determine the deviation of the simulation data from the experimental data, a criterion based on the difference between the simulated and experimentally observed frequencies of interference fringes was devised. In this criterion, the values obtained by adding the multiplication of the squares of the ratios of the differences between the most dominant experimental and simulated frequencies were scaled by the ratio of the individual amplitude in each slice to the highest amplitude in the first slice were used Equation 5.1. The least deviated cases are evaluated as the ones having the most similar parameters with the experimental conditions. The width of the slices is selected to ensure that the most dominant frequencies present in each slice are not duplicated in successive slices. The criterion devised for FFT comparison is,

$$\text{FFT Comparison criterion} = \epsilon^2_{\text{FFT}} \equiv \sum_{j=1}^{n} \left(\frac{f_{\text{exp},\,j} - f_{\text{sim},\,j}}{f_{\text{exp},\,j}} \right)^2 \left(\frac{A_j}{A_1} \right)^2 \qquad (5.1)$$

where f_{exp} is the frequency of the experimental data having the highest amplitude in the data slice, f_{sim} is the frequency of the simulation data having the highest amplitude in the data slice, A is the highest amplitude belonging the frequencies detected in the data slice, A_1 is the highest amplitude belonging the frequencies detected in the first data slice, n is the number of frequencies at different points and j is the index number. The reason of the $(A_j/A_1)^2$ term is to increase the weight of the high-amplitude and low-frequency region on the criterion by reducing the effect of the data carrying optical signals close to the noise level in the data in terms of amplitude. In addition, the purpose of squaring the terms is to make the difference between simulation results more distinctive.

The case having the lowest FFT Comparison Criteria value is the best fit to the experimental case. The application of the FFT Anlaysis for comparison of the experimental and the simulation data is shown in subsection 5.1.3 in detail for determination of the optimum resolution for the simulations.

5.1.2 Zero Crossing Method

In addition to the FFT analysis, a second method is also implemented to compare the experimental and simulated data. Zero Crossing Method basically determines the locations where the data cross zero. Before finding zero crossing values, first the specific regions of the data covering the optical signal are selected. Then by determining the amplitude value which the data oscillates around and reducing this amplitude value to zero, both of the experimental and simulation data are normalized. For the experimental data firstly moving average which is a type of filtering method is applied to the data and the frequencies higher than the ones which the optical signal has, including the noise are filtered. Moving Average Method creates a new data set averaging the data points in a specified range of data. The experiments are conducted with a sampling

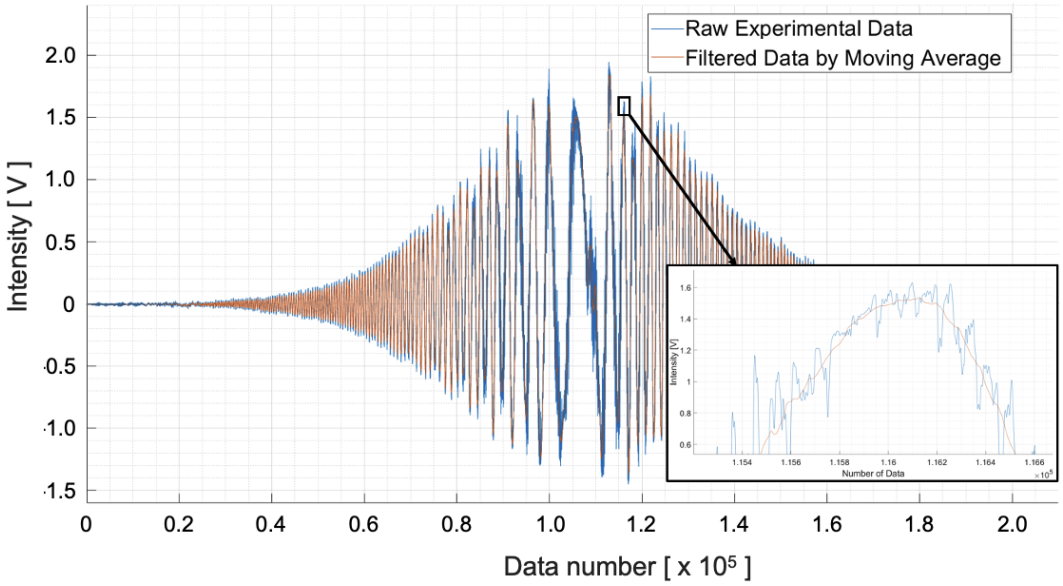

Figure 5.6: Data filtered using Moving Average Method with the window size of 150 on the normalized raw experimental data

rate of 10 000 Hz and it is known that the optical signal has frequencies lower than 50 Hz. So the window size of the Moving Average Method is selected 150 which is a value lower than 200 (10 000/50). In Figure 5.6 the data filtered using Moving Average Method is shown on the raw experimental data. After the filtering process the whole procedures are applied to both of the experimental and simulation data in the same way.

For both experimental and simulation data, the points which the data having zero amplitude are determined. By employing the data sampling rate for the experimental data and an equivalent sampling rate for the simulation data, the average frequency values are calculated for each data interval between the consecutive zero amplitude points, and these frequencies are accepted as belonging to the middle point of each interval. As an example the frequencies obtained from the zero crossing points of the filtered experimental data shown in Figure 5.6 is given in Figure 5.7. As it is seen there is a noise on the side parts of the data having the high frequencies. Also while the data have low frequencies in the middle section, the frequencies which the data have increases towards the side parts of the optical signal as expected.

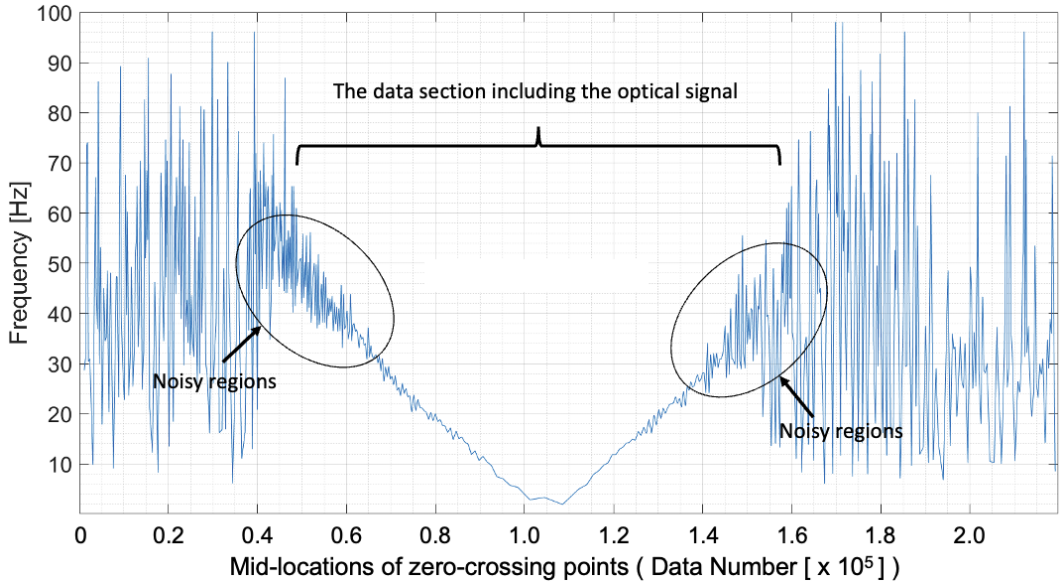

Figure 5.7: Frequencies obtained from zero crossing points of the filtered experimental data

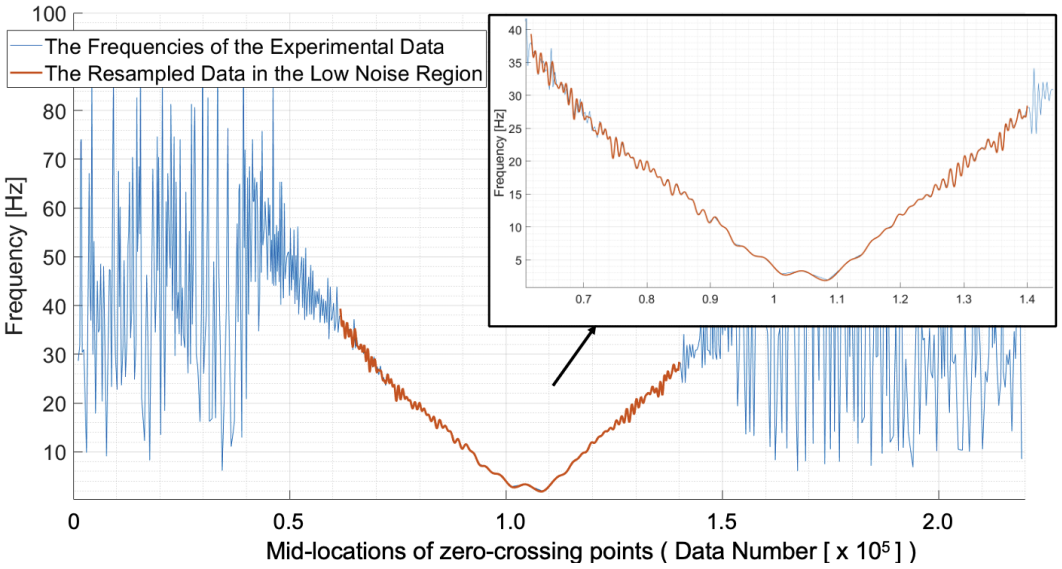

Figure 5.8: Data section with low noise level used in the analysis to compare the experimental and simulation data in terms of frequencies

To be able to use the frequencies in comparison of the experimental and simulation cases, only the section which does not have noises in a comparable level with the optical signal are used in the analysis. Also it is needed the frequencies in the same points to be able to compare the experimental data and the simulation data. For this reason the data handled in low noise region are resampled by using spline function to equalize the numbers of frequency data of the experiment and the simulation. The section and the resampled data used in the analysis are shown in Figure 5.8.

Next, both of the middle points of the frequency locations of the experimental and the simulation data are determined so the midpoints of the frequencies are overlapped and the frequencies at the same location are compared according to the determined matching criteria. The midpoints determined for the frequencies is also the midpoints of the experimental and the simulation data. The experimental and the simulation data overlapped with respect to their midpoints are shown in Figure 5.9.

Figure 5.10 shows the frequencies of the experimental and the simulation data. As it is seen, the frequency ranges are different for the experimental and the simulation data so to be able to compare them the limits of the frequencies are

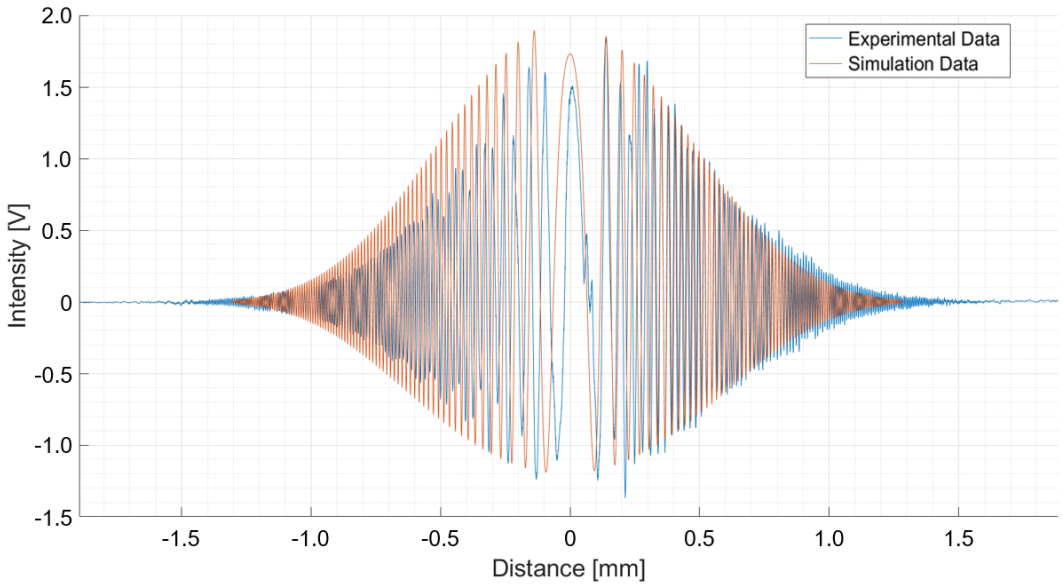

Figure 5.9: Experimental and simulation data overlapped by their midpoints

equalized by cropping the frequency ranges of both of the data. The frequencies in the equalized range are shown in Figure 5.11.

The third measure for compares the frequencies of the experimental and the simulated data in the equalized range by using two matching criteria which are

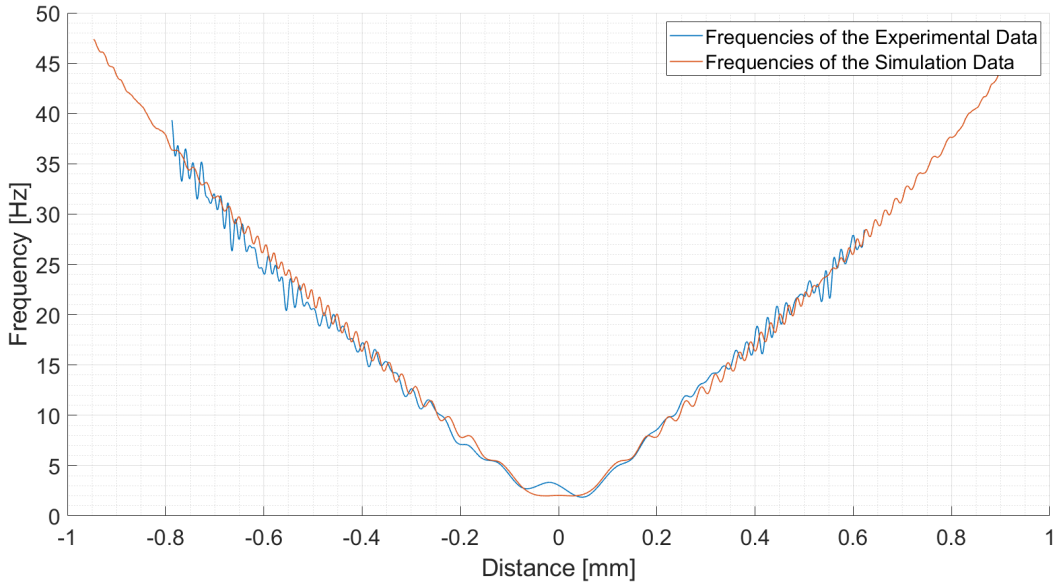

Figure 5.10: Frequency distributions of the experimental and the simulation data

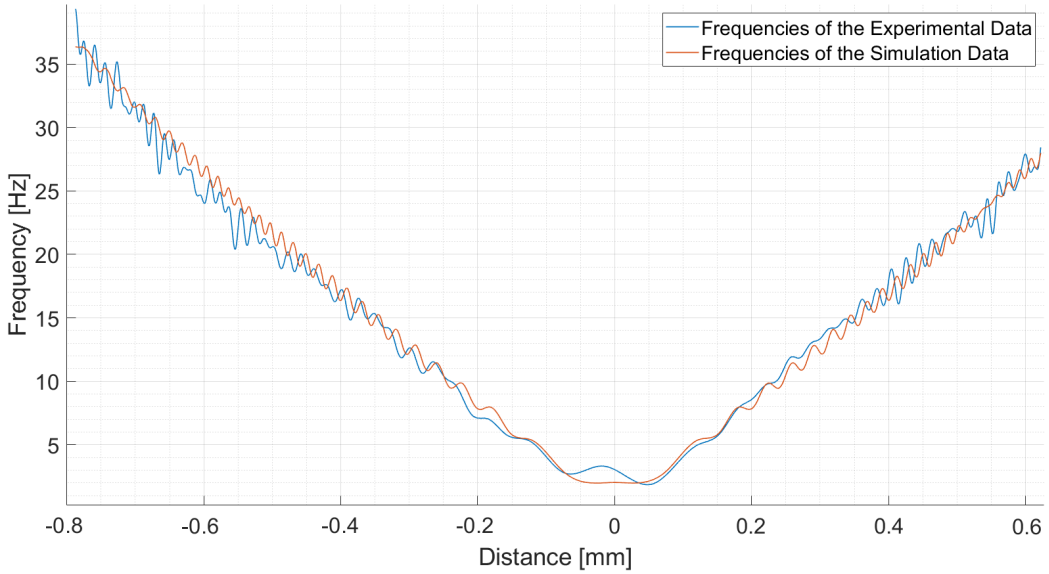

Figure 5.11: Frequencies of the experimental and the simulation data in the equalized range

the Mean Squared Error and The Coefficient of Determination or R-squared. These criteria are given in Equation 5.2.

$$\begin{aligned} \mathrm{MSE} &= \frac{1}{n}\sum_{j=1}^{n}\left(f_{\mathrm{exp},\,j} - f_{\mathrm{sim},\,j}\right)^2 \\ R^2 &= 1 - \frac{\sum_{j=1}^{n}\left(f_{\mathrm{exp},\,j} - f_{\mathrm{sim},\,j}\right)^2}{\sum_{j=1}^{n} {f_{\mathrm{exp},\,j}}^2} \end{aligned} \tag{5.2}$$

where f_{exp} is the frequency of the experimental data having the highest amplitude in the data slice, f_{sim} is the frequency of the simulation data having the highest amplitude in the data slice, n is the number of frequencies at different points and j is the index number. While the case having the lowest MSE value is the best fit to the experimental case, the case having the highest R^2-value (recall that maximum value being the unity) is the best fit best to the experimental data.

5.1.3 Optimum Resolution for FFT Analysis

Before the simulations were performed for the comparison, the resolution of the simulations needs to be determined. The resolution of the simulations increases by increasing the number of the beams coming out from the FOP and decreasing the step size of the FOP along its movement in the simulations. The resolution analysis was performed for constant values of the FOP height of 1.49 mm, the width of the liquid film of 5.04 mm and the height of the liquid film of 0.62 mm which are the parameters selected in the determined ranges on the photograph of the test section. The increase in resolution brings with it an increase in duration of the solution process. For this reason, working with an optimum resolution prevents time loss.

At the beginning of the simulation the first process is to determine the middle point of the experimental data so that the middle point of the simulation data are positioned as coincident with the middle point of the experimental data. Determination of the middle point of the experimental data is made by finding the arithmetic mean of the first two bottom and top peaks of the fringes at the left and right side of the symmetry axis of the experimental data. The selected

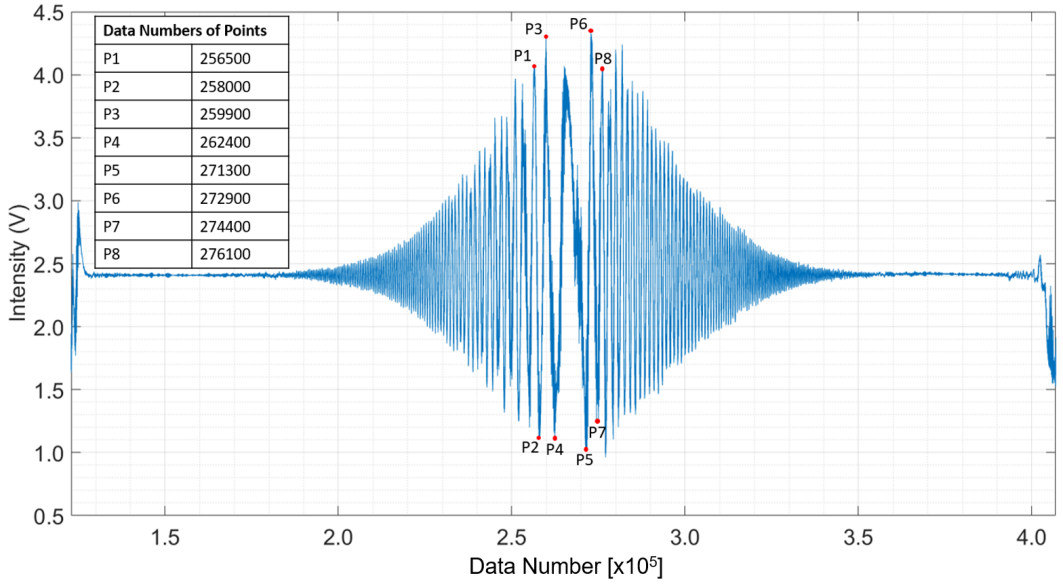

Figure 5.12: Data points to determine the midpoint of the experimental data for the engine oil on the gold-coated silicon wafer

eight data points to determine the middle point of the experimental data are shown in Figure 5.12. The arithmetic mean of the data numbers of these data points, 266 438, gives the middle of the experimental data.

The simulation data are superimposed on the experimental data so that the midpoints of the experimental and the simulation data overlap. Figure 5.13 shows simulation data and the experimental data placed so that their midpoints overlap. The simulation data were collected for the liquid film width of 8.36 mm, the probe height of 4.49 mm, and the liquid film height of 0.42 mm. Also in Figure 5.13 the cross-sectional shape of the simulated liquid film in the direction of the FOP is shown with yellow. At this time the distance values corresponding the number of data are given in horizontal axis. Zero point of the horizontal axis is the middle point of the liquid film.

In order to determine the width and the number of the slices to which FFT is applied, the boundaries of the data including optical signal in the given region must first be determined. The intensity of the fringes on the experimental data decrease towards the left and right corners of the liquid film. In case of

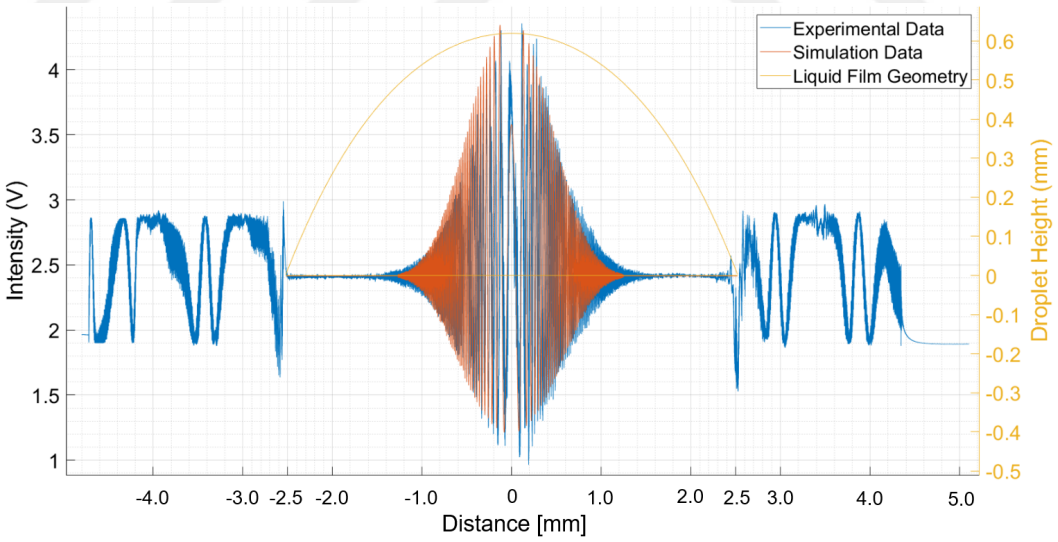

Figure 5.13: Simulation data for the liquid film with a width of 5.04 mm, probe height of 1.49 mm, and height of 0.62 mm fitted on the experimental data by overlapping the midpoints of them. Simulated liquid film shape is shown with yellow.

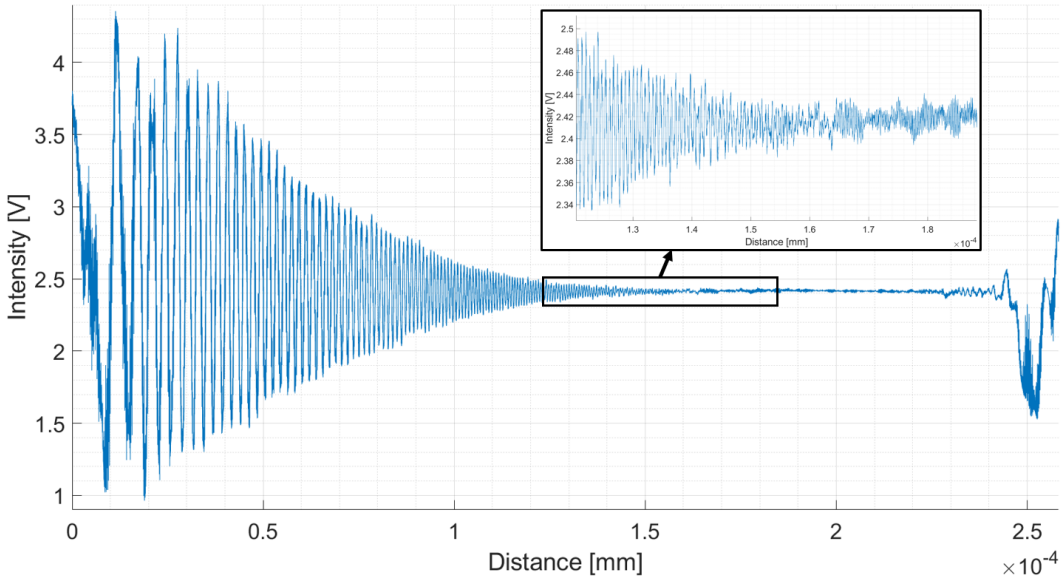

Figure 5.14: Right side of the experimental data for the engine oil on the gold-coated silicon wafer

stationary FOP, the experimental data has an almost constant intensity. But there is always a certain level of noise on the experimental data. The location where the intensity value is close to the noise is examined to find the rightmost or leftmost location where interference can be measured. Figure 5.14 shows only the right side of the experimental data to investigate the rightmost end of the range where the measurement is taken. After a point the intensity of experimental data becomes comparable with the noise on the data so at that point determination of the end of the optical signal becomes very difficult.

FFT of the right part of the experimental data for different size of slices gives an idea about the end point of fringes due to the optical signal. FFT analysis is performed by dividing this interval into different number of slices. For example, Figure 5.15A shows FFT analysis for 4000 data in each slices in a total of 23 slices. The resolution of the FFT analyses increases with the number of the data handled. Also we know that in the right side of the experimental data while the frequency increases the amplitude decreases towards the right. So if the whole right side of the data including the optical signal is used in the FFT analysis, the frequency having the highest amplitude which is the middle region of the whole data in the result would be the frequency of the most left part of the data

handled.

As shown in Figure 5.15A there are repetitive frequencies. By increasing the number of data in the slices step by step, the number of data needed to obtain a non-repetitive frequency in a slice is found. The number of the slices is arranged to cover almost all of the data. It is seen that increasing frequency changes suddenly after 21st slice. This means that the optical signal ends after that point. That point corresponds to 350 540th (266 540 + 21 × 4 000) data point.

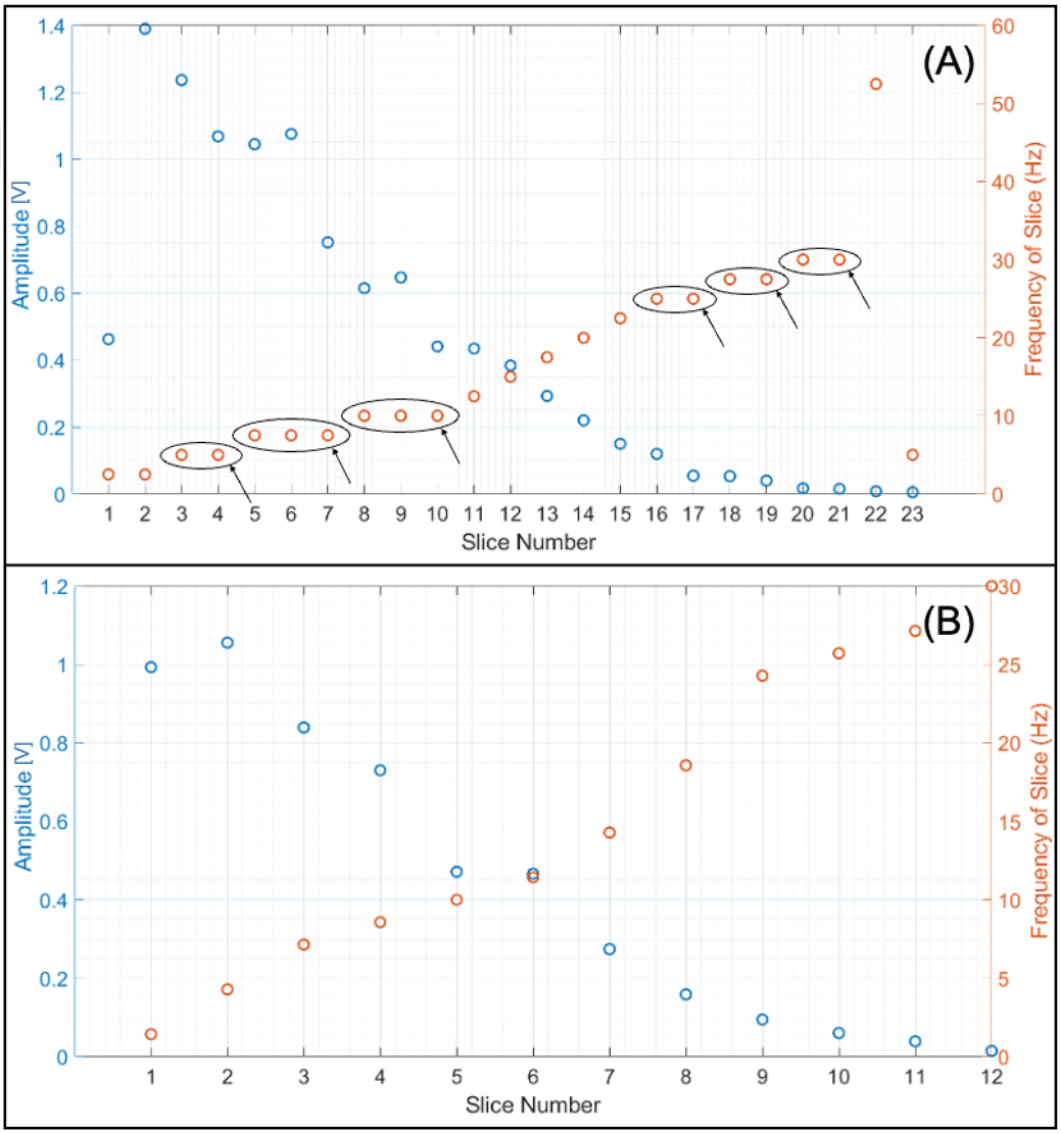

Figure 5.15: FFT analysis of the right part of the experimental data: (A) Slices of 4000 data points and (B) slices of 7000 points data

After that point and also in 20th and 21th slices the data have low amplitudes which are comparable with the noise on the data. Therefore it is noted that 20th and 21th slices which have amplitudes of frequencies comparable to the noise amplitude might not show an effective criteria to compare the simulations with the experiment.

Figure 5.15B shows FFT analysis for slices of 7 000 data in a total of 12 slices. This range is determined by the point where the frequency has a sudden change in Figure 5.15A. That is, the analysis was made up to the point where the optical signal ended ($266\,540 + 12 \times 7\,000 = 350\,540$). Up to the end of 12th slice, the frequencies increase continuously. There is no repetitive frequency in consecutive slices. Therefore slices of 7000 data and totally 12 slices are accepted as suitable to use in comparison of the experimental and simulation data.

Next, to determine the resolution of the simulation, simulations for different number of beams and step sizes are compared for the case covering the data of the engine oil having width of 5.04 mm, height of 0.62 mm, and the FOP having the height of 3.50 mm. For example, firstly to decide the number of beams coming out from the FOP to be used in the simulations, simulations were performed and FFT analyses were realized for different number of beams. The simulations were made with the step size of 0.9 μm for the number of beams of 100, 200, 400, 600 and 800, respectively. The results of FFT analyses of the experimental and simulation data in the 14 slices covering variable sizes of 7 000 data and its multiplies for the number of beams of 100, 200, 400, 600 and 800 are shown in Figure 5.16.

The FFT results of the simulation with 100 beams differ substantially from the experimental one in the last 4 slices according to the FFT analyses given in Figure 5.16A. The FFT results with 200 beams do have only observable deviation in 9th slice compared to the ones with more beams. However the FFT results with 400 beams do not have any significant changes with respect to the results with 600 and 800 beams. Therefore, 400 beams are accepted to be sufficient for use in the simulations. However for more accurate results, the beam number at each point is kept as 800 in the simulations.

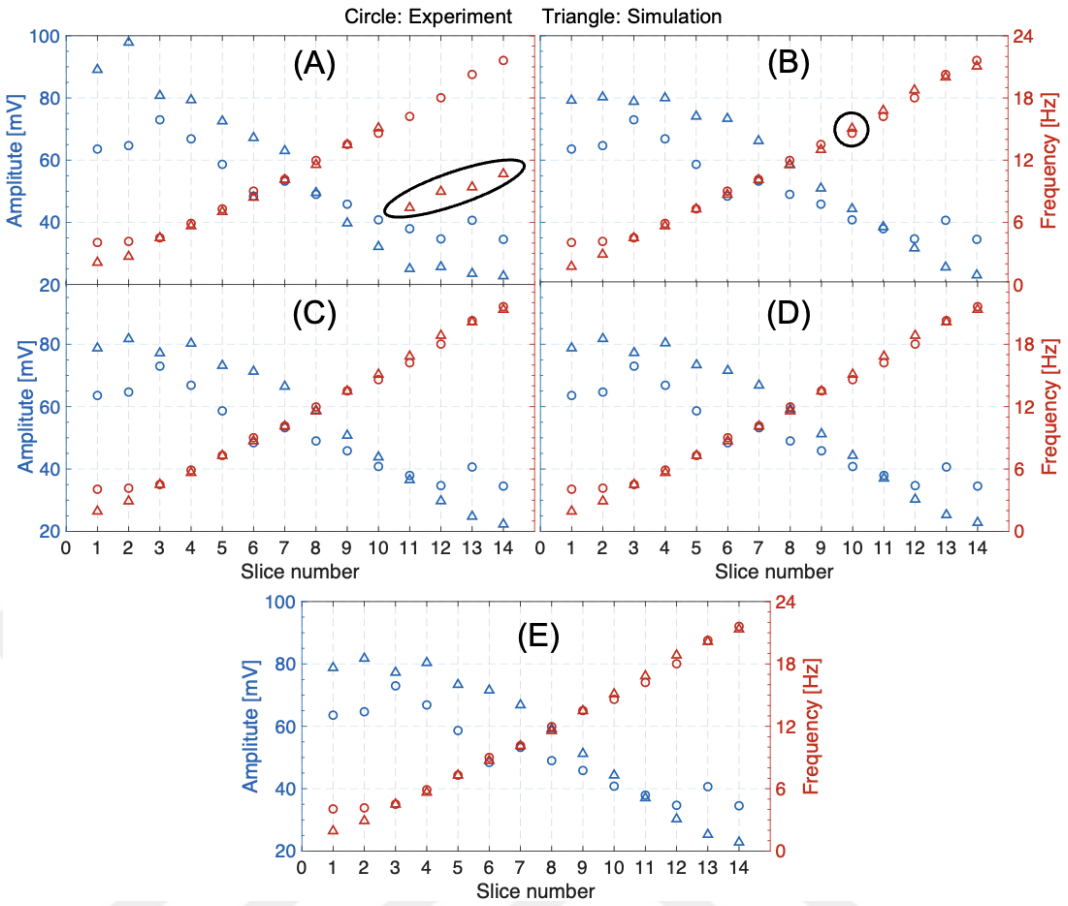

Figure 5.16: FFT analysis the experimental and simulation data with a step size of 0.9 µm: (A) 100 beams, (B) 200 beams, (C) 400 beams, (D) 600 beams and (E) 800 beams.

The effect of the step size is investigated to determine the sufficient resolution. Five step sizes which are 4.5 µm, 3.6 µm, 2.7 µm, 1.8 µm and 0.9 µm are evaluated in the same way with the evaluation of the number of beams for 800 beams FFT analysis results of these five cases are shown in Figure 5.17.

When Figure 5.17 is investigated, decreasing the step size to increase the resolution from 0.45 µm to 0.9 µm causes some changes in the frequencies in the slices. In Figure 5.17 the changes determined in the frequencies in the slices are shown with respect to the case with the step size 0.9 µm.

It should be noted that a decrease in the step size increases the computational load substantially. For example the simulations with 800 beams for the step sizes

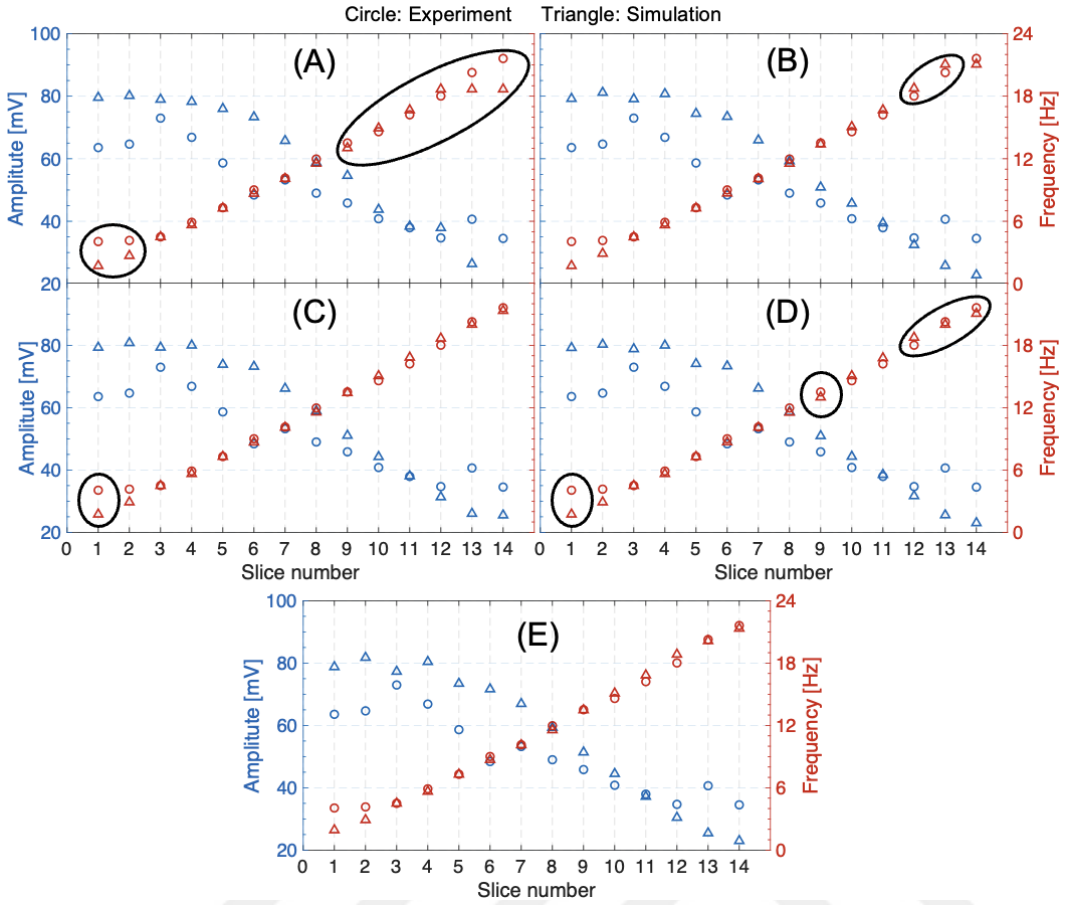

Figure 5.17: FFT analysis the experimental and simulation data for 800 beams with a step size of (A) 4.5 µm, (B) 3.6 µm, (C) 2.7 µm, (D) 1.8 µm and (E) 0.9 µm.

of 4.5 µm, 3.6 µm, 2.7 µm, 1.8 µm and 0.9 µm take about 25 min, 55 min, 180 min, 270 min and 360 min respectively by using a computer with the processor of Intel(R) Core(TM) i7-4800MQ CPU @2.70GHz. Therefore, considering the few and small changes in the slices in FFT analysis performed for different step sizes, to save time the step size of 1.8 µm is chosen and used in the simulations.

As a result of the resolution analysis, the number of beams coming out from the FOP and the step size of the FOP along its movement over the liquid film to be used in the simulations are determined as 800 and 1.8 µm, respectively.

5.2 Determination of Liquid Film Profile

In this section, based on the determined resolution parameters, the liquid film, which is the engine oil (Shell Risella X430), on the gold-coated silicon wafer, whose dimensions were delimited within a specific range as illustrated in Figure 5.4, underwent simulation to determine the cross sectional shape of the liquid film. However, in this instance, the height of the FOP was set at 3.50±0.01 mm. The simulations were performed in for 12 variations in the height of the liquid film and 3 variations in the height of the FOP, ranging between the identified maximum and minimum values as stated before. The simulated and experimental data obtained for the shape of the liquid film shown in Figure 5.18 were analysed by using both FFT analysis and Zero Crossing Methods.

While for FFT analysis the set of data obtained from the right half of the liquid film is used, for Zero Crossing Method the low noise region of the entire data

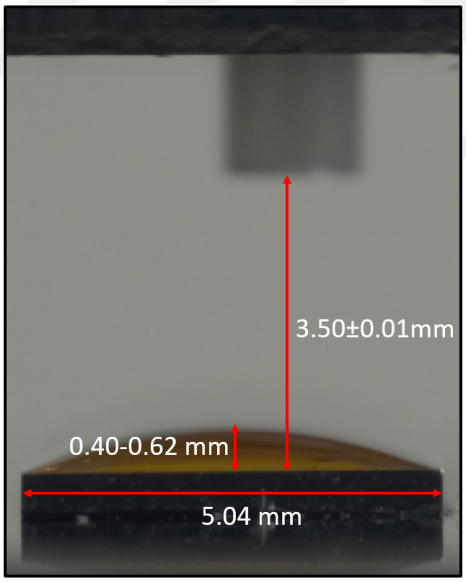

Figure 5.18: The dimensions of the test section. The range of the height of the liquid film is obtained by using the dimensions read on the photograph with the help of the parametric drawing tool. The width of the liquid film is the width measured by a caliper of the gold-coated silicon wafer on which the liquid film is placed. The height of the FOP is arranged by using the micrometers in the experimental setup with an accuracy of ±0.01 mm.

range including the optical signal is used.

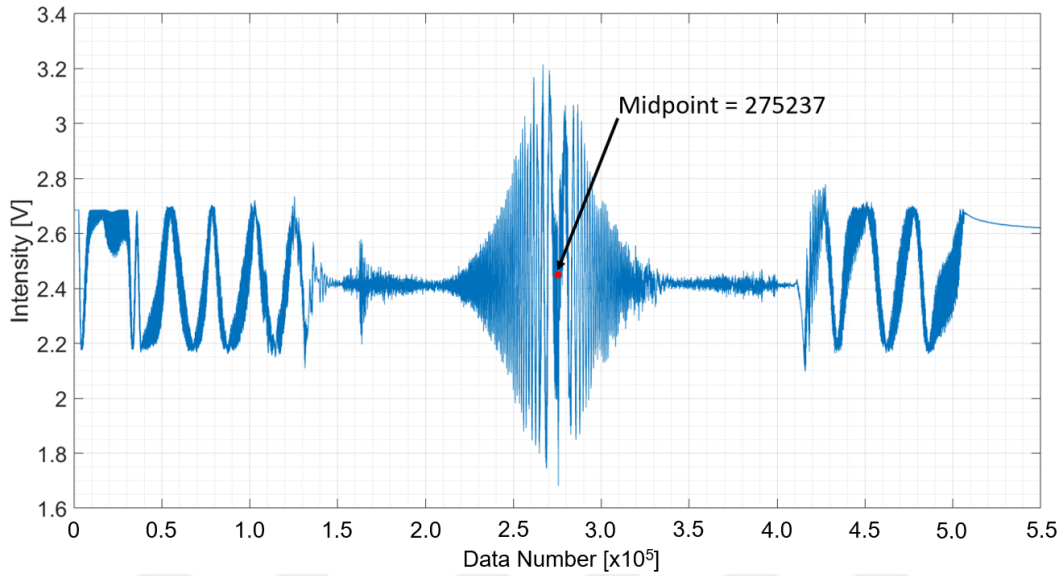

(a) The raw experimental data belonging to the case where the height of the FOP is 3.5 mm, the width of the engine oil on the gold-coated silicon wafer is 5.04 mm.

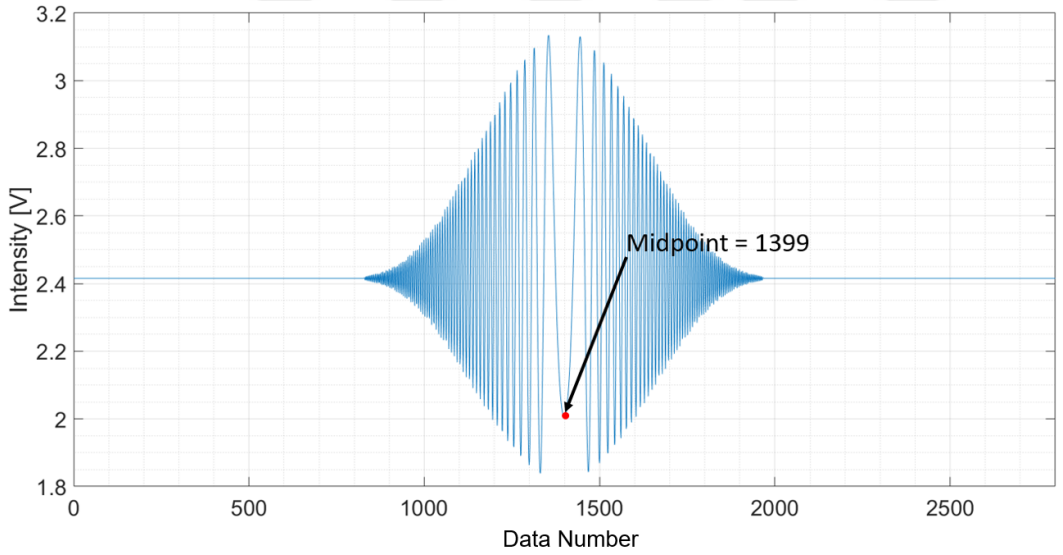

(b) The simulation data performed for the height of the FOP of 3.5 mm, the width of the liquid of 5.04 mm ad the height of the liquid film of 0.62 mm with the step size of 1.8 μm and the number of beams of 800.

Figure 5.19: Comparison of FFT of the experimental and simulation data for different step sizes

Firstly both of the experimental and the simulated data were analyzed by FFT. The middle points of the experimental and the simulated data were detected by averaging the local top intensity values in the data as 275 237 and 1399, respectively as shown in Figure 5.19.

Following this, FFT analyses were performed by dividing this interval into different number of slices in the experimental data. The results were evaluated for the end location of the optical signal and obtaining no repetitive frequencies in consecutive slices. As a result the number of the slices where FFT will be made and the size of the slices i.e. the number of data points in a slice were selected as 14 and 3700, respectively. The determined number of the slices and the determined size of the slices were used for the simulated data, too. The frequencies obtained in the slices are shown in Figure 5.20 for the experimental and the simulated data performed for the height of the FOP of 3.50 mm and the height of the liquid film of 0.62 mm.

The frequencies in the slices were used to calculate the FFT Comparison Criteria which is given in Equation 5.2 to compare the experimental and simulation data.

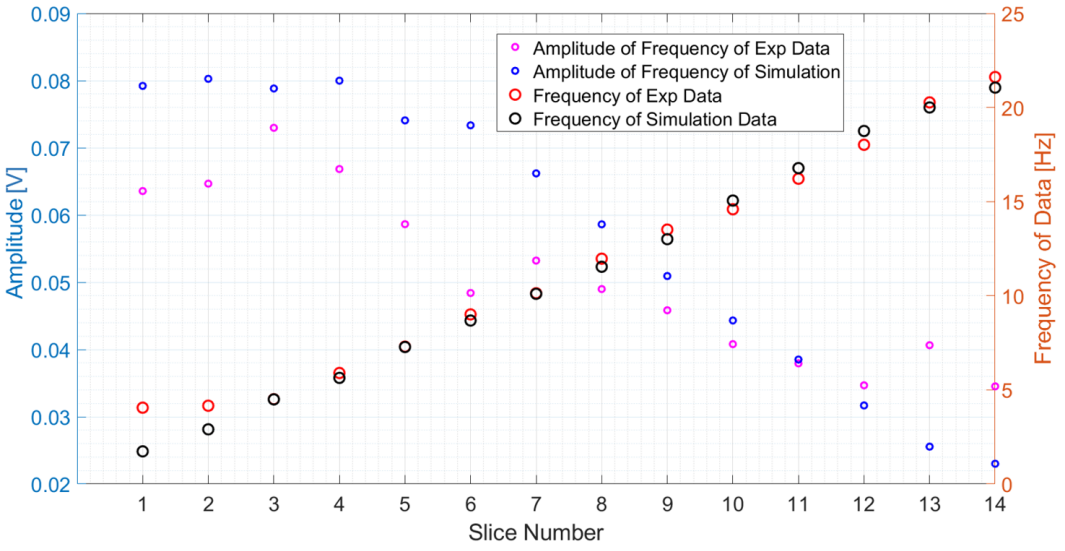

Figure 5.20: The frequencies obtained in the slices for the experimental and the simulation data with the number of the slices of 14 and the size of the slices of 3700

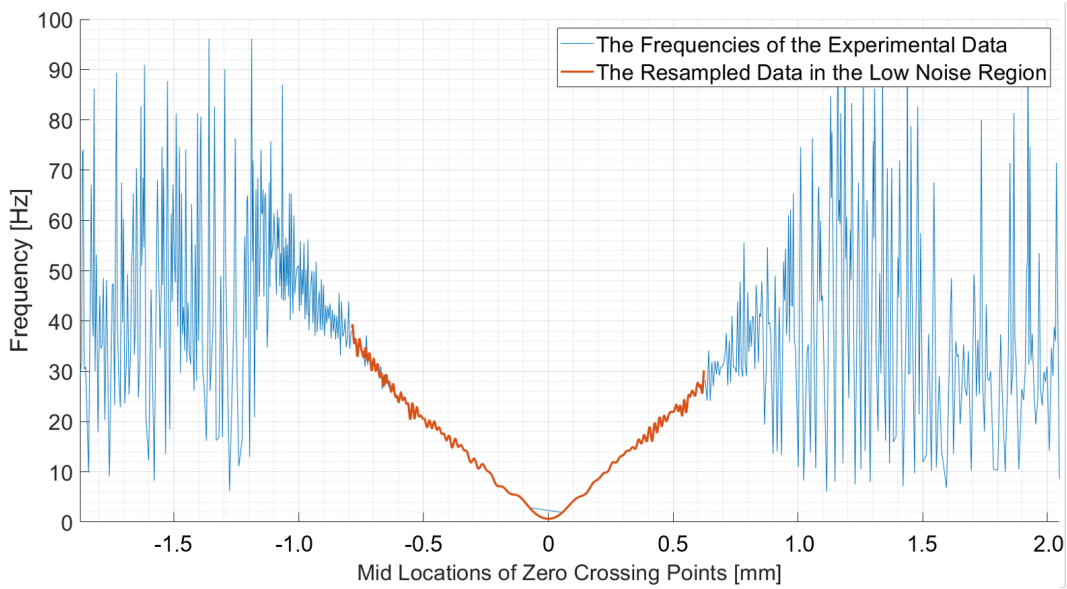

Figure 5.21: The low noise region of the frequencies of the experimental data

Next, as a second method to compare the experimental and simulation data Zero Crossing Method was applied. Firstly, the experimental and the simulation data were normalized by reducing the amplitude value which the data oscillate around to zero. Then Moving Average filtering was applied to the experimental data. The frequencies of both of data were calculated in the middle points of each interval between the zero crossing points. The low noise region of the frequencies of the experimental data which would be used in comparison with the simulation data was determined as shown in Figure 5.21. Then the midpoints of both of the data were determined and overlapped with respect to their midpoints. Finally as it is shown in Figure 5.22 the frequency data of both the experiment and the simulation were cropped to equalize the limits of the frequency ranges to be able to make comparison between them.

In the frequency ranges with the equalized limits, the frequencies were compared by using MSE and R^2 values given in Equation 5.2. The summary of the comparison results of the simulations which were performed for the height of the FOP of 3.49 mm, 3.50 mm and 3.51 mm, the height of the liquid film of twelve values equally spaced between 0.40 mm and 0.62 mm and the width of the liquid film of 5.04 mm were listed in Table 5.1 as mentioned in the previous sections. The simulations were made with the number of the beams of 800 and the step

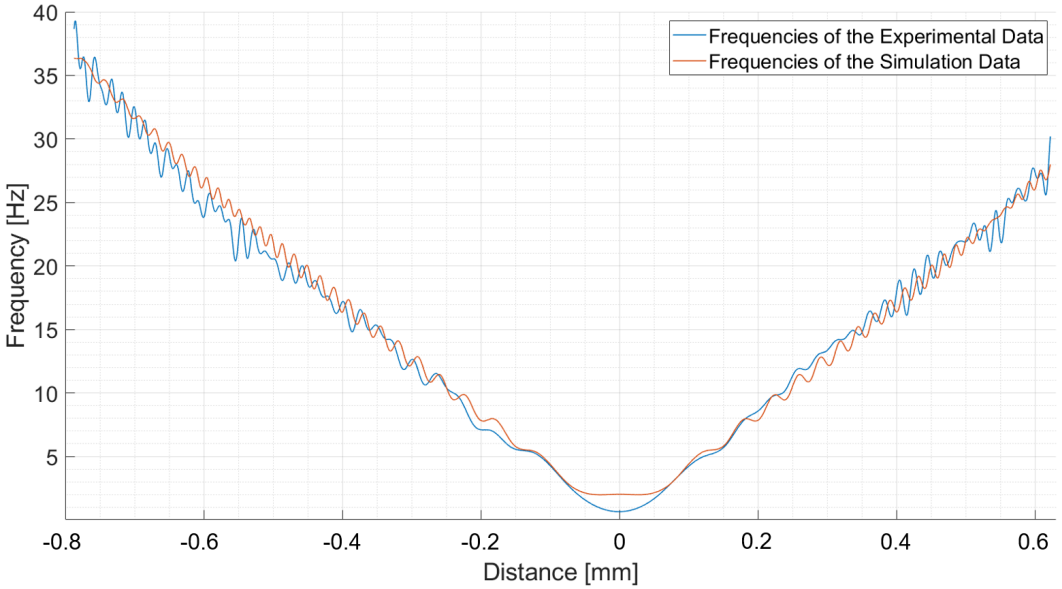

Figure 5.22: The frequency ranges with the equalized limits for the experimental and the simulation data

size of the FOP of 1.8 μm. In addition to the three values of the height of the FOP, the heights of 0.45 mm and 0.55 mm which are out of the determined range are simulated and compared with the experimental data to see the precision of the analysis. All comparison results of the simulations which were performed for the height of the FOP of 3.45 mm, 3.49 mm, 3.50 mm, 3.51 mm and 3.55 mm, for the height of the liquid film of twelve values equally spaced between 0.40 mm and 0.62 mm and the width of the liquid film of 5.04 mm. Additionally the simulation results covers the cases with the height of the liquid film of 0.64 mm for different probe heights can be seen in Table B.1 in Appendix B. Moreover for the simulation cases whose comparison criteria is in the limit of the determined range of the height of the liquid film the cases having the height of the liquid film of 0.64 mm are also investigated. In Table 5.1 Radius of Curvature ($\mathcal{R}$) at the middle point of the cross sectional shape of the liquid film is given as well.

In Table 5.1, the red color shows the case fitting best to the experimental data for the heights of the FOP of 3.45mm, 3.49 mm, 3.50 mm, 3.51 mm and 3.55 mm according to all three comparison criteria. The blue color specifies the criteria which show the best fitting cases in the measured range of the experiment where the height of the FOP is between 3.49 mm and 3.51 mm. The yellow color is

used for criteria that show the simulation cases that are not the best among all cases, but are the best for each probe height.

Table 5.1: Summary table for comparison of the height of the FOP of 3.45 mm, 3.49 mm, 3.50 mm, 3.51 mm and 3.55 mm

Liquid Width [mm]	**Probe Height [mm]**	**Liquid Height [mm]**	$\mathcal{R}$ **@midpoint [mm]**	**FFT Comp. Criteria**	**MSE**	**R2**
5.04	3.45	0.62	6.51	0.364	0.882	0.990
5.04	3.49	0.58	6.87	0.450	1.813	0.979
5.04	3.49	0.60	6.68	0.644	1.067	0.988
5.04	3.50	0.60	6.68	0.531	0.970	0.989
5.04	3.50	0.62	6.51	0.426	1.057	0.988
5.04	3.51	0.60	6.68	0.492	0.941	0.989
5.04	3.51	0.62	6.51	0.429	1.195	0.986
5.04	3.55	0.62	6.51	0.405	1.034	0.988

Basically the experiment with convergence values for different parameters is given in Table 5.1 was performed within a range of the height of the FOP between 3.49 mm and 3.51 mm. Firstly when the comparison criteria given in Table 5.1 for these three height of the FOP are investigated, it is seen that the cases fitting best the experimental case are the one with the height of the FOP of 3.50 mm and the liquid height of 0.62 mm for FFT Comparison Criteria and the one with the height of the FOP of 3.51 mm and the liquid height of 0.60 mm for MSE and R2 criteria obtained by Zero Crossing Method. When Table B.1 in Appendix B is investigated to be able to see the convergence situation of the simulations with the heights of FOP of 3.45 mm and 3.55 mm, it is seen that a better fit is obtained by the height of the FOP of 3.45 mm and the liquid height of 0.62 mm. However a better fit is obtained by a simulation case with the height of the FOP which is not in the measured range of the experiment (0.49 mm-0.51 mm), the height of the liquid, 0.62 mm, which is converged to is not different than the simulation cases with the parameters in the measured range of the experiment. As a result of these simulations the height of the liquid film is estimated as between 0.60 mm and 0.62 mm covering the information

of the cross sectional shape of the liquid for different comparison criteria. The corresponding ROC values at the top of the liquid of these two values of the height of the liquid film are 6.68 mm and 6.51 mm. As a result, the simulation data examined according to three different comparison criteria can detect a maximum range of 0.02 mm (3.3%) for a liquid film height of at least 0.60 mm, even though the probe height exceeds the range determined in the experiment. This detection range is equivalent to detecting a 0.17 mm range (2.6%) for a minimum ROC value of 6.51 mm at the peak of the liquid film.

5.2.1 Effect of the Height of the FOP

To understand the effect of the height of the FOP on determination of cross sectional shape of liquid film, interferometric experiments were performed for four different heights of the FOP while keeping the shape of liquid film. The heights of the FOP set in the experiments are 1.5 mm, 3.5 mm, 5.5 mm and 7.5 mm. The experiments were performed by moving the FOP over the engine oil (Shell Risella X430) put on the gold-coated silicon wafer. The width of the gold-coated silicon wafer is 5.04 mm, hence the width of the liquid. The rough data obtained from the experiments with 4 different heights of the FOP is shown in Figure 5.23. As expected the intensity of the experimental data decreases with the increasing distance between the FOP tip and the reflective surface. Also the intensity of the noise on the data becomes comparable with the optical signal with increasing height of the FOP. The increase in the height of the FOP results in a narrowing of the distances at which the optical signal is detected. In addition, the number of fringes in the part where the optical signal is received decreases.

According to the dimensions determined from the photographs taken during each experiments, the investigation range of the height of the liquid film is decided as between 0.4 mm and 0.62 mm. In this range twelve heights of the FOP at equal distances was analyzed in the simulations. The procedure of the simulation and the comparison with the experimental case was explained in the previous sections. FFT analyses were conducted using varying numbers of slices

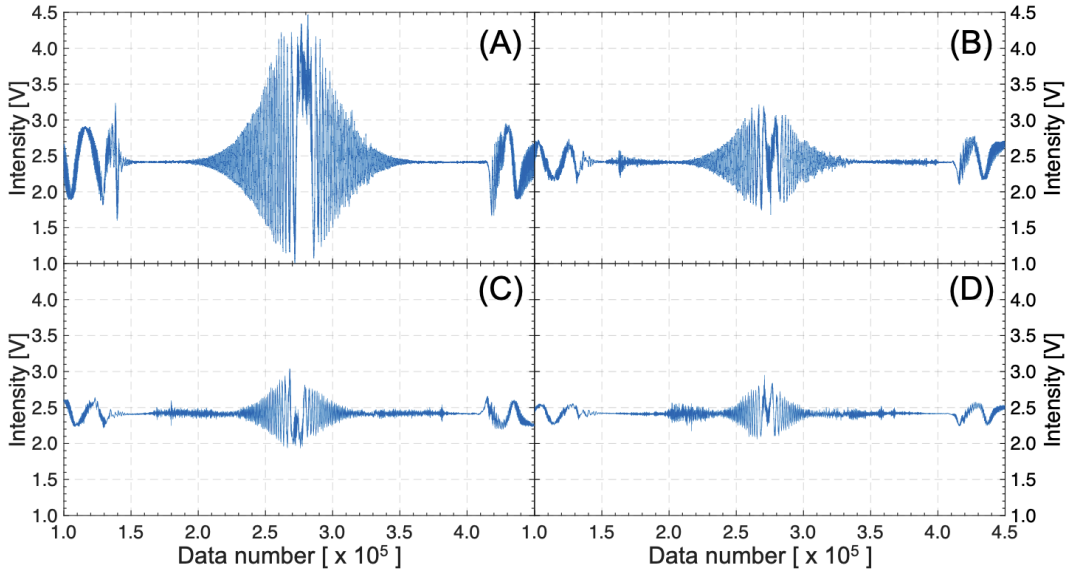

Figure 5.23: Rough experimental data for different FOP height (liquid width: 5.04 mm): (A) 1.5 mm, (B) 3.5 mm, (C) 5.5 mm and (D) 7.5 mm.

suitable for each height of the FOP. The simulations were realized with the resolution (the number of beams of 800 and the step size of the FOP of 1.8 µm) determined in subsection 5.1.3. The parameter sets that were found to be most compatible with the experimental data according to the 3 comparison criteria are shown in the Table 5.2 for the two analysis types. With the Zero Crossing Method, one liquid height value of 0.62 mm is indicated for each of four FOP heights. The results obtained by FFT analysis with variable slices showed the most compatible parameters for the liquid height of 0.60 mm and 0.62 mm.

Table 5.2: The simulation results for the experiments which is performed with the engine oil on the gold-coated silicon wafer for different heights of the FOP

							FFT Analysis with Variable Slices	Zero Crossing Method	
Experimental Probe Height [mm]	**Liquid Width [mm]**	**Probe Height [mm]**	**Liquid Height [mm]**	**$\mathcal{R}$ @midpoint [mm]**	**Slice Number for FFT**	**Number of Data in Each Slice for FFT**	**FFT Comp. Criteria**	**MSE**	**R2**
1.50±0.01	5.04	1.49	0.62	6.51	12	7000	0.759	4.973	0.946
1.50±0.01	5.04	1.51	0.6	6.68	12	7000	1.182	4.612	0.950
3.50±0.01	5.04	3.5	0.62	6.51	14	3700	0.426	1.057	0.988
3.50±0.01	5.04	3.51	0.60	6.68	14	3700	0.492	0.941	0.989
5.50±0.01	5.04	5.51	0.60	6.68	17	2600	0.261	1.493	0.982
5.50±0.01	5.04	5.51	0.6	6.68	17	2600	0.261	1.493	0.982
7.50±0.01	5.04	7.49	0.62	6.51	12	2700	0.054	4.313	0.951
7.50±0.01	5.04	7.50	0.6	6.68	12	2700	0.113	3.363	0.961

By using the values of the slice number of FFT and the number of data in each slices for FFT given in Table 5.2, the numbers of the data which include the optical signal can be calculated as 84000 (12×7000) data for $h_{probe} = 1.5$ mm, 51800 (14×3700) data for $h_{probe} = 3.5$ mm, 44200 (17×2600) data for $h_{probe} = 5.5$ mm, 32400 (12×2700) data for $h_{probe} = 7.5$ mm. Although the noise level is comparable with the intensity of the optical signal in high heights of the FOP, the comparison analysis achieves to detect the height of the liquid film in the maximum range of 0.02 mm. Especially the zero crossing method determines the shape of the liquid film in a range lower than this value.

5.2.2 Effect of Height of Liquid

5.2.2.1 Engine oil on gold-coated silicon wafer

In this section the engine oil put on the gold-coated silicon wafer was used under the FOP. In four different cases by adding liquid between the experiments, 4 different heights of the liquid was obtained while the width of the liquid stays the same which i the width of the gold-coated silicon wafer. By moving the FOP over the liquid placed on the reflective surface interferometric measurements

Table 5.3: The simulation results that best fit the experimental data with different heights of the engine oil on the gold-coated silicon wafer

							FFT Analysis with Variable Slices	**Zero Crossing Method**	
Liquid Shape Number	**Liquid Width [mm]**	**Probe Height [mm]**	**Liquid Height [mm]**	**$\mathcal{R}$ @midpoint [mm]**	**Slice Number for FFT**	**Number of Data in Each Slice for FFT**	**FFT Comp. Criteria**	**MSE**	**R2**
1	5.04	3.5	0.62	6.51	14	3700	0.426	1.057	0.988
1	5.04	3.51	0.60	6.68	14	3700	0.492	0.941	0.989
2	5.04	3.49	0.85	5.20	17	2400	0.480	3.189	0.969
2	5.04	3.50	0.89	5.07	17	2400	1.785	1.993	0.981
3	5.04	3.49	1.14	4.60	18	2200	0.130	6.048	0.952
3	5.04	3.50	1.14	4.60	18	2200	0.224	5.880	0.954
4	5.04	3.49	1.21	4.57	12	3000	0.181	14.659	0.893
4	5.04	3.51	1.23	4.56	12	3000	0.228	14.161	0.897

were taken. During all of the experiments the distance between the FOP tip and the reflective surface was 3.50±0.1 mm. The interferometric experiments carried out for liquids at 4 different heights were considered for 3 different cases where the probe height was 3.49 mm, 3.50 mm and 3.51 mm. For each probe height, analyzes were made within the possible range of the height of the FOP obtained from the photographs taken during the experiments. These ranges are 0.40 mm - 0.62 mm for the 1st liquid shape, 0.71 mm - 0.89 mm for the 2nd liquid shape, 0.94 mm - 1.14 mm for the 3rd liquid shape and finally 1.19 mm - 1.51 mm for the 4th liquid shape. In each interval, liquid heights were analyzed with 0.02 mm intervals. The analysis results were evaluated with the criteria determined for FFT analysis with variable slices and 2 criteria determined for the Zero Crossing Method. For each liquid shape, the simulation results that best match the experimental data according to these 2 methods are presented in Table 5.3. The criterion values indicated in red indicate the situation most compatible with the experimental data for that liquid form, determined by the methods under which they are included. The difference in the liquid height values determined by the two methods for the second liquid form, where the two methods converged furthest from each other, was 0.04 mm. The percentage rate in the ROC values in the middle of the cross-section geometry of the liquid

corresponding to these height values was calculated as 2.67%. In other liquid shapes, the convergence values of these two methods in liquid height could not exceed 0.02 mm.

5.2.2.2 IPA on gold-coated silicon wafer

Interferometric experiments were repeated, this time by placing IPA on the gold mirror. Since IPA has high volatility, the experiments were started by placing liquid close to the upper amount it could carry on the gold mirror. Since the amount of liquid decreases every time the FOP passes over the IPA, experiments for different liquid heights can be carried out quite easily. At the beginning of the experiments the height of the FOP was arranged as 3.50±0.01 mm. Therefore the simulations were performed for the three heights of the FOP of 3.49 mm, 3.50 mm and 3.51 mm. Four cases which have different liquid heights were selected to analyze. The simulations were carried on in the range of the height of the liquid determined from the photograps taken during the experiments. The simulation results obtained by the two comparison methods as a result of the analyses performed to find the best matching parameter set with the

Table 5.4: The simulation results that best fit the experimental data with different heights of IPA on the gold-coated silicon wafer

							FFT Analysis with Variable Slices	**Zero Crossing Method**	
Liquid Shape Number	**Liquid Width [mm]**	**Probe Height [mm]**	**Liquid Height [mm]**	**$\mathcal{R}$ @midpoint [mm]**	**Slice Number for FFT**	**Number of Data in Each Slice for FFT**	**FFT Comp. Criteria**	**MSE**	**R2**
1	5.04	3.49	0.45	3.85	18	5600	1.213	10.261	0.910
1	5.04	3.49	0.41	4.24	18	5600	1.774	3.739	0.975
2	5.04	3.51	0.54	3.21	13	6500	1.157	39.621	0.787
2	5.04	3.51	0.56	3.10	13	6500	1.195	33.751	0.819
3	5.04	3.51	0.74	2.36	14	5300	0.273	4.870	0.962
3	5.04	3.49	0.70	2.49	14	5300	0.279	3.630	0.974
4	5.04	3.51	0.87	2.03	16	3900	0.471	13.587	0.874
4	5.04	3.51	0.87	2.03	16	3900	0.471	13.587	0.874

experimental data are shown in Table 5.4.

The results in Table 5.4 shows that the maximum difference in the liquid height determined by the two comparison methods is 0.04 mm. This value stands out as a maximum of 9.9% difference in the ROC value for the liquid profile determined at low liquid heights, for example 0.41 mm and 0.45 mm. As the liquid height increases, the difference between the criteria in ROC detection decreases according to the liquid height.

5.2.2.3 Engine oil on gauge block

In this section, the results of the simulations carried out for the experiments in which engine oil was placed on a gauge block with a surface roughness of less than 20 μm are discussed. Since the corners on the edge of the gauge block were not sharp, it was necessary to examine the liquid width considered in the simulation with different values. Caliper measurement shows the gauge block width as 9.0 mm. The rounds in the corners suggested that the width of the liquid would be smaller than 9.0 mm, and from the photographs taken during the experiments, it was determined that the width value of the liquid should be

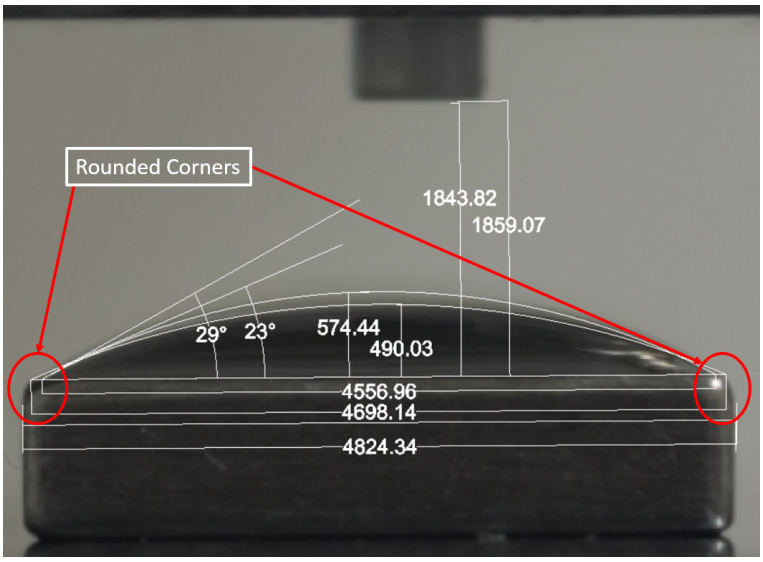

Figure 5.24: Photograph of the test section with engine oil on gauge block with rounded corners

examined between 8.4 mm and 9.0 mm. The investigation of the photograph of the test section is shown in Figure 5.24. In this determined width range, four equally spaced width values f the liquid were used in the simulations. For each liquid width value, the height of the FOP, which was set as 3.50±0.01 mm with a micrometer in the experiments, was handled as 3.49 mm, 3.50 mm and 3.51 mm in the simulations. Simulations were made by taking liquid height values at 0.02 mm intervals in the liquid height range of 0.85 mm–1.11 mm, determined from the photograph, at each width value of the liquid and the height of the FOP. The simulation results are shown in Table 5.5. The simulations of the experiments performed with the gauge block took longer than those performed with the gold mirror due to the larger liquid width.

According to the simulation results obtained with two comparison methods, the simulation data most compatible with the experimental data is obtained with a liquid width of 0.84 mm and a liquid height between 0.91 mm and 0.95 mm. The simulation results show that the liquid width value could be determined with a maximum resolution of 0.20 mm. Similar to the gold mirror experiments described previously, it can be seen that the two different comparison methods

Table 5.5: Simulation results for the experiments with the engine oil on the gauge block analyzed for different widths of the liquid film

						FFT Analysis with Variable Slices	**Zero Crossing Method**	
Liquid Width [mm]	**Probe Height [mm]**	**Liquid Height [mm]**	**$\mathcal{R}$ @midpoint [mm]**	**Slice Number for FFT**	**Number of Data in Each Slice for FFT**	**FFT Comp. Criteria**	**MSE**	**R2**
8.4	3.49	0.95	3.17	35	4000	0.715	3.176	0.971
8.4	3.49	0.91	3.31	35	4000	0.944	2.699	0.975
8.6	3.50	1.11	2.76	35	4000	1.104	10.601	0.902
8.6	3.51	1.01	3.02	35	4000	1.740	2.870	0.973
8.8	3.49	1.11	2.79	35	4000	1.886	3.006	0.972
8.8	3.49	1.09	2.84	35	4000	2.792	2.898	0.973
9.0	3.49	1.11	2.82	35	4000	2.780	4.631	0.957
9.0	3.51	1.11	2.82	35	4000	4.540	4.594	0.958

considered estimate the liquid height with a difference of at most 0.04 mm.

5.2.3 Effect of Inclination of Reflective Surface

The effect of the deviation of the reflective surface carrying the liquid film from the horizontal position was investigated. Especially in the cases including high height of the liquid film with respect to its width which has low ROC values, the numbers of the fringes which are used to detection of the frequency change in the optical signal may be very low and this causes obtaining low number of frequency locations along the range of the optical signal. It is known that in the cases where only the reflective part without liquid on it, the increasing amount of the deviation from its horizontal position causing the change in the distance between the tip of the FOP and the reflective surface increases the number of the fringes in the optical signal during the horizontal movement of the FOP over it. For the purpose of increasing numbers of the fringes in the optical signal, the cases created some deviations from the horizontal position of the reflective surface in case of the reflective part with the liquid on it were investigated .

By adjusting the height of the micrometers that carry the reflective part at different distances from both sides, the reflective surface was allowed to deviate from the horizontal position. By changing the height of the micrometers proportionally, the rotation point of the slope was provided at the middle point of

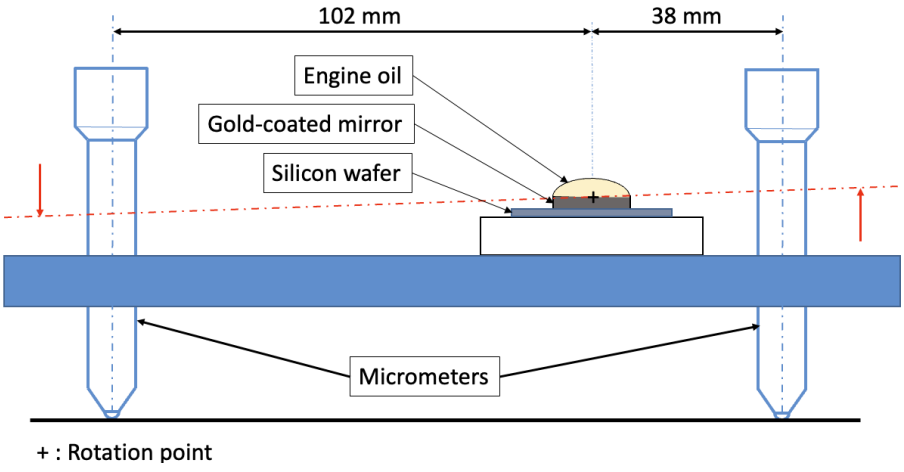

Figure 5.25: Schematic view of the situation with inclined reflective surface

the liquid film in the lateral cross sectional view. The schematic view of the inclined case of the reflective surface is given in Figure 5.25. As it is seen in Figure 5.25 the reflective part which is the gold-coated silicon wafer whose width is 5,04 mm was placed on the silicon wafer which has also a reflective surface. The engine oil was used in the experiments with the inclined reflective part as the liquid placed on the reflective part. During the interferometric experiments optical signals were also collected from the positions where the FOP passed over the silicone wafer. The optical signal collected from the positions where the FOP passed over the silicone wafer gives information about the change of the slope of the reflective surface.

The height of the micrometers was changed proportionally to the limit allowed by the experimental setup, so that the position of the rotation point in Figure 5.25 did not change, and the reflective part was tilted at an angle of 0.0025° between each interferometric experiment. To observe the effect of inclination of

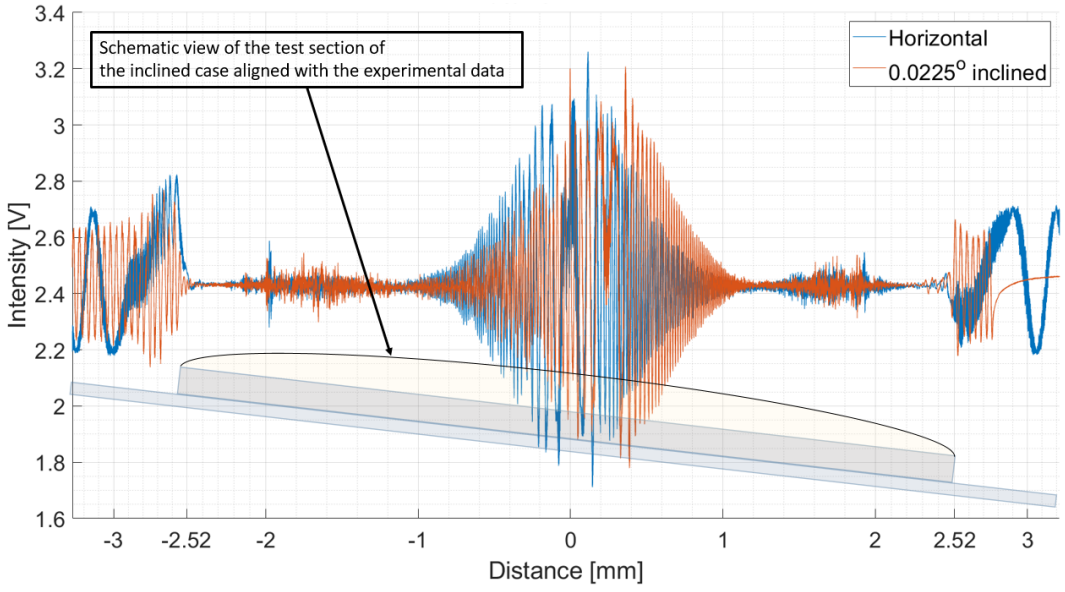

Figure 5.26: Experimental raw data of the cases in the horizontal position and the position inclined with 0.0225°. The zero point of the horizontal axis is aligned with the midpoint of the experimental data of the case in the horizontal position. Also the schematic view of the test section of the inclined case aligned with the is shown with an exaggerated angle.

the reflective part on the optical signal in a more observable way, the experimental raw data of the cases in the horizontal position and the position inclined with 0.0225° which is the limit angle the experimental setup allows is given in Figure 5.26. The experimental data given in Figure 5.26 were collected during the movement of the FOP from the right side to the left side in the horizontal direction. It can be said that the increase in the number of fringes in the optical data in the inclined case taken from the silicon wafer, seen in the far right and left parts of Figure 5.26, is an indicator of the inclined surface.

In Figure 5.27 showing the the experimental raw data of the cases in the horizontal position and the position inclined with 0.0225° focused on the region with the optical signal, it is seen that the midpoint of the optical signal moved towards the right. Because of the inclination, the shape of the droplet changes and the highest point of the liquid film slides towards the side where the height of the reflective part is reduced. The region where the optical signal is collected does not change in observable amount at this given tilt angle.

The amplitude changes of the fringes in the data of the inclined case are clearly observed due to the change in the shape of the liquid film. Although the liquid

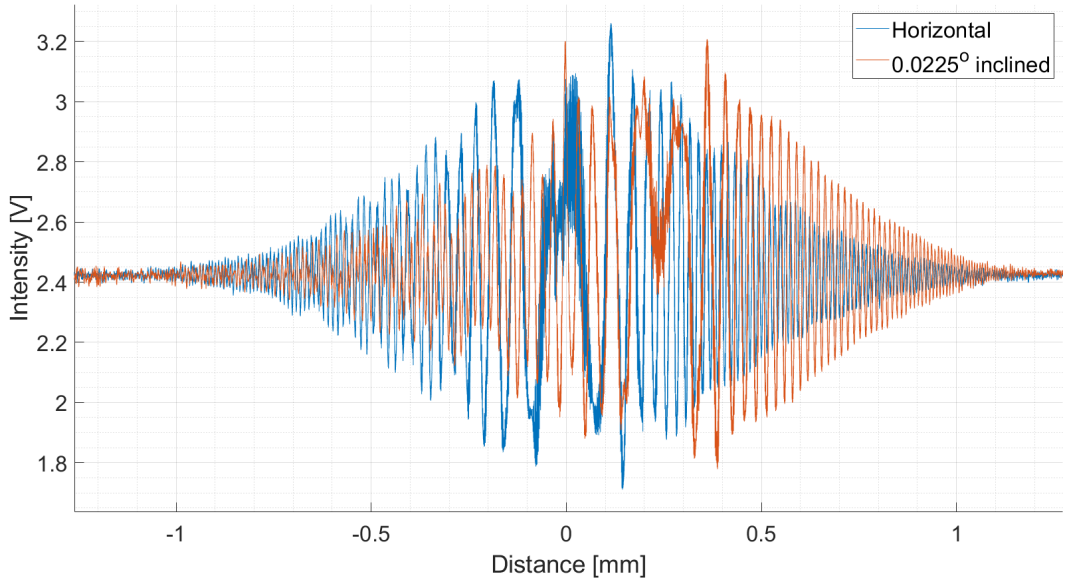

Figure 5.27: Experimental raw data of the cases in the horizontal position and the position inclined with 0.0225° focused on the region with the optical signal

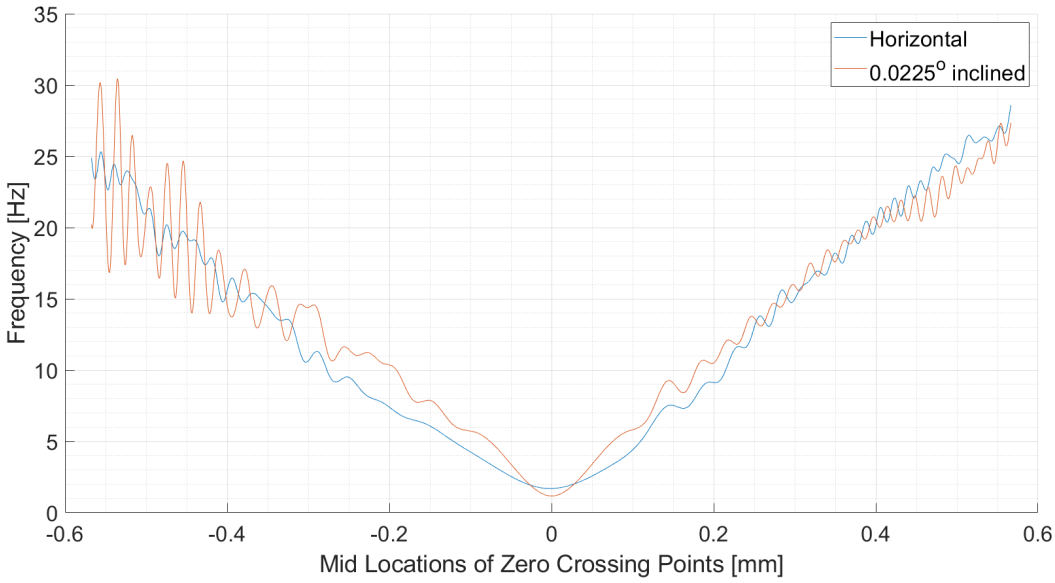

Figure 5.28: Frequency distribution graph obtained by superimposing the midpoints determined from the experimental data of the horizontal and the inclined cases

shape is noticeably inclined to the reflective part on the experimental data, when the experimental data were examined in terms of the number of fringes in the inclined and horizontal cases, it is seen that there is no increase in the number of fringes in the inclined case in the range where the optical signal was received.

When we look at the frequency distribution graph given in Figure 5.28 obtained by superimposing the midpoints determined from the experimental data, it is seen that the liquid film shape has an effect on the frequency distribution. The frequencies of the data of the experiment performed in the horizontal position have more clear in terms of noise.

As a result, it can be said that inclination of the reflective piece carrying the liquid film causes a shape deviation from the symmetric case and does not provide an increase in the numbers of the fringes in the same region which the optical signal is collected. Moreover, the case of the horizontal reflective piece provides low noisy interferometric data which is convenient for further data analysis. Therefore it can be concluded that keeping the reflective surface as horizontal as possible is essential for interferometric experiments.

5.3 Determination of Height of Liquid Film for Validation

The FOP can be placed on the reflective surface while adding liquid to detect the height of the liquid film. First of all, the reflective surface is brought to a fully horizontal position. Afterwards, data is collected with a FOP during the process of adding liquid to the reflective surface and by counting the number of fringes in the data the height at the center of the liquid film can be determined. What needs to be taken into consideration here is that the FOP is positioned exactly on the top point of the liquid film section, corresponding to the center of the film, whose profile is measured. Before the liquid is added, the beams coming out of the FOP only travel through the air between the FOP and the reflective surface, while the beams also travel through the liquid when the liquid is added. In this case, the beams coming out of the FOP are reflected from the reflective surface and pass through the liquid as well as the gas (air) during the path of the beams until they return back to the FOP tip. Since the medium with a different refractive index changes the optical path of the beams, fringes are seen in the collected data because of the increased optical path experienced by the light rays. The process of liquid addition and the corresponding change in the height of gas and air under the probe is shown in Figure 5.29 schematically.

In an experiment conducted with engine oil on a gold-coated silicone wafer, the FOP is initially positioned in the middle of the reflective surface. Afterwards,

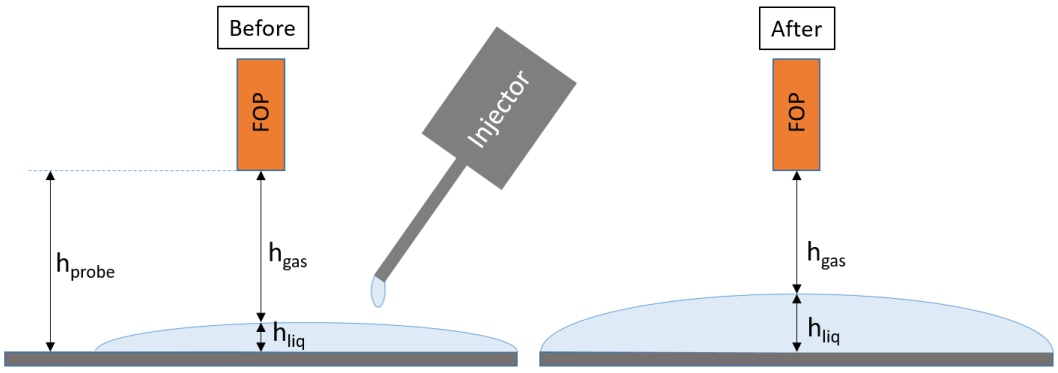

Figure 5.29: Schematic view of liquid addition on the reflective surface and change of the height of liquid (engine oil) and gas (air) under the probe

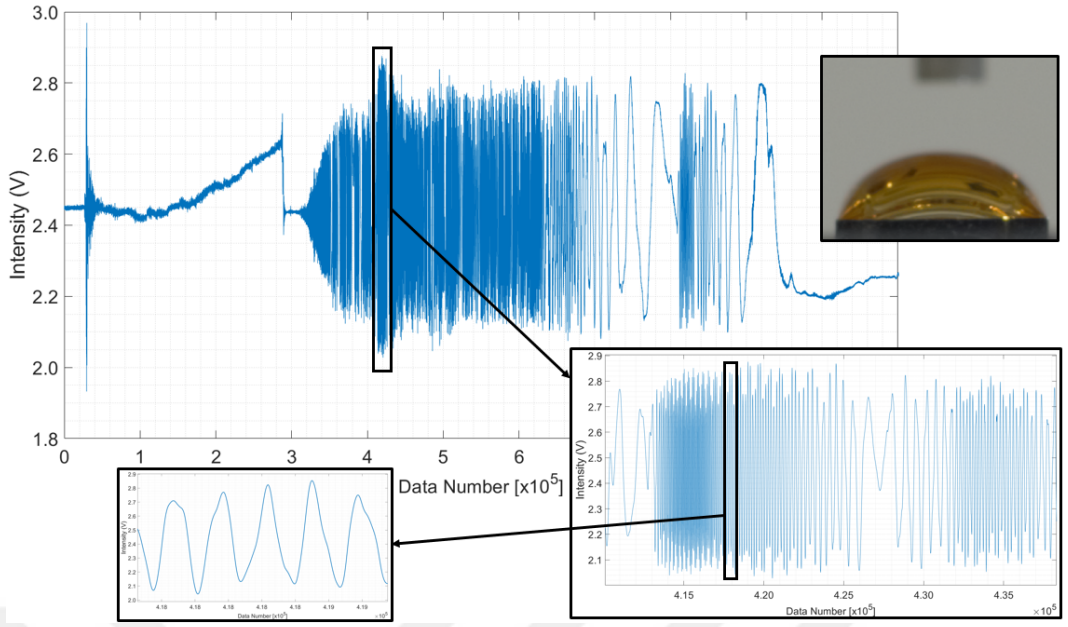

Figure 5.30: Raw experimental data collected during adding liquid on the reflective surface

liquid is added, and data is collected throughout the liquid addition process with the FOP. The collected raw experimental data and the lateral photograph of the final liquid film are given in Figure 5.30. The fringes in the experimental data are clearly visible. In the case of no liquid on the reflective surface, the optical path of the beams until they return back to the tip of the FOP is given as:

$$\mathrm{OPL_{w/o\ liq}} = n_{\mathrm{air}} \times 2\mathrm{h_{probe}} \tag{5.3}$$

When a second medium with a different refractive index, in this case engine oil, is added on the reflective surface replacing air, the optical path length of the beams is calculated as:

$$\mathrm{OPL_{liq}} = n_{\mathrm{gas}} \times 2\mathrm{h_{gas}} + n_{liq} \times 2\mathrm{h_{liquid}} \tag{5.4}$$

where $\mathrm{h_{gas}}+\mathrm{h_{liq}} = \mathrm{h_{probe}}$. The number of the fringes in the experimental data are directly related to the change in the optical path of the beams as:

$$N_{\mathrm{fringes}} = \frac{\mathrm{OPL_{liq}} - \mathrm{OPL_{w/o\ liq}}}{\lambda} \tag{5.5}$$

By substituting Equation 5.4 into Equation 5.5, the height of the liqud film is

calculated as:

$$\mathrm{h_{liquid}} = \frac{N_{\mathrm{fringes}}\lambda}{2\left(\frac{n_{liq}}{n_{gas}} - 1\right)} \tag{5.6}$$

The number of fringes in this experiment is 790. The wavelength of the laser source in the experiment is 1550 nm, and substituting the refractive index of air and engine oil in Equation 5.6, the height of the liquid film in the experiment can be calculated as 1.33 mm. The possible range of the height of the liquid film from the acquired photograph is between 1.14–1.66 mm. The simulations have performed for the liquid heights in this range with 0.01 mm intervals. According to the comparison criteria obtained with zero crossing method, the best fitted simulation to the experimental data in terms of frequencies was for 1.25 mm. This result shows that the error in the analysis performed for the liquid profile is about 6% for the liquid height of 1.33 mm. This preliminary study for determination of the height of the liquid film is promising for validation of the analyses performed in the scope of the thesis.

CHAPTER 6

CONCLUDING REMARKS

In this thesis work, a method was developed to determine the shape of the air-liquid interface of a liquid film placed on a reflective surface by using fiber optic interferometry.

Experiments were carried out by moving the fiber optic probe horizontally over a liquid that could spread on the surface, placed on a metal piece with a reflective surface positioned exactly parallel to the horizontal plane. In the experiments, the engine oil (Shell Risella X430) and IPA were used as liquids, a 5.04 mm wide gold-plated mirror and a 9 mm wide gauge block were used as metal parts with a reflective surface. In all the experiments the photographs of the test section in the lateral view were taken to get an information about the geometric parameters of the test section.

Evaluation of the experimental data to determine the liquid film shape was investigated and firstly FFT analyses for sufficient number of variable slices of one half of the experimental data were decided to apply. As a second investigation method Zero Crossing Method was decided to apply. For FFT analysis with variable slices, 1 comparison criterion was determined that prioritizes the low resolution match between the experimental data and the simulation data, while for the Zero Crossing Method, 2 comparison criteria were determined that consider the amount of deviation of the experimental data from the frequency distribution. While FFT analysis with variable slices considers only the part of the experimental data that reaches one half of the liquid, assuming the symmetrical shape of the liquid film, Zero Crossing Method offers an approach that includes both halves of the liquid, where the noise level in the frequency distri-

bution of the experimental data is evaluated as low.

Before the simulation of the experimental conditions, the optimal resolution of the simulations were detected by making simulations with different resolution values. Usage of the number of the beams exiting the tip of the fiber optic probe of 800 and the step size of the fiber optic probe of 1,8 µm was decided.

Firstly, how the detection of the cross sectional shape of the liquid film is realized by detecting the best match between the experimental data and the simulation data among many results of the simulation cases performed with many different test parameters was described. Then, the effects of the different fiber optic probe heights on determination of the cross sectional shape of the liquid were elucidated by making experiments and simulations with the different heights of the fiber optic probe for the same height of the liquid. Also the cases with different types of the liquid and the reflective test piece were handled for different shapes of the liquid. In addition, different values of liquid width were also examined to determine the liquid profile in the simulations.

According to the simulation results obtained, it has been determined that the liquid height can be determined with a difference of at most 0.04 mm by two different test-simulation comparison methods, regardless of the type of liquid whose cross-sectional shape is evaluated and the metal part with the reflective surface. This difference between the methods in determination of the liquid height brings about a greater percentage difference in the radius of curvature value compared to its nominal value at low liquid heights compared to high ones. In cases where the liquid width is not known clearly, that is, the metal piece on which the liquid is placed does not have sharp edges, this method can determine the liquid width up to 0.2 mm at most.

The situations that can be considered as future work can be listed as follows.

- The simulation code can be optimized to obtain faster results for the cases with the determined optimum resolution.
- Improvements can be made to the experimental setup to reduce the noise on the optical data collected during the horizontal movement of the fiber

optic probe in the test setup. Reducing the noise on the experimental data will reduce the margin of error in the liquid profile predictions given by the simulations.

- The validation method of the simulation is taking high-resolution photographs of the test section in the lateral direction at the moment of the experiment as much as possible. Under current conditions this is the best way to validate the simulations. The accuracy of this validation method may be increased. Additionally, in order to verify the simulations in the best possible way, simulation results can be evaluated by performing interferometric experiments on semi-cylindrical solid test pieces of different sizes, with precisely known dimensions, suitable for interferometric experiments, made of uniform transparent materials, with outer surfaces of high optical quality.

- For the validation of the results of the anaysis, determination of the height of the liquid film by placing the fiber optic probe over the reflective part during the process of liquid addition can be improved in terms of counting of the fringes on the experimental data and positioning of the fiber optic probe over the middle of the reflective part for more accurate results.

  This preliminary study for determination of the height of the liquid film is promising for validation of the analyses performed in the scope of the thesis.

REFERENCES

[1] S. Khan, S. Le Calvé, and D. Newport. "A review of optical interferometry techniques for VOC detection". In: *Sensors and Actuators A: Physical* 2020 (302), page 111782. DOI: https://doi.org/10.1016/j.sna.2019.111782.

[2] J. Park, J.-A. Kim, H. Ahn, and J. Bae. "A Review of Thickness Measurements of Thick Transparent Layers Using Optical Interferometry". In: *International Journal of Precision Engineering and Manufacturing* 2019 (20/5), pages 799–812. DOI: 10.1007/s12541-019-00105-0.

[3] C. Tibiricça, F. Nascimento, and G. Ribatski. "Film thickness measurement techniques applied to micro-scale two-phase flow systems". In: *Experimental Thermal and Fluid Science* 2010 (34/4), pages 463–473.

[4] J. N. Israelachvili. "Thin Film Studies Using Multiple-Beam Interferometry". In: *Journal of Colloid and Interface Science* 1973 (44/2), pages 302–313.

[5] W. M. Nozhat and D. B. Stewart. "Measurement of liquid-film thickness by laser interferometry". In: *Applied Optics* 1997 (36/30), pages 703–706.

[6] H. Shabana. "Determination of film thickness and refractive index by interferometry". In: *Polymer Testing* 2004 (23/6), pages 695–702.

[7] N. Borgetto, C. Galizzi, F. André, and D. Escudié. "A thickness measurement technique based on low-coherence interferometry applied to a liquid film with thermal gradient". In: *Experimental Thermal and Fluid Science* 2010 (34/8), pages 1242–1246.

[8] N. Borgetto, F. Andre, C. Galizzi, and D. Escudie. "Simultaneous film thickness measurement and wall temperature assessment by Low-Coherence

Interferometry". In: *Experimental Thermal and Fluid Science* 2013 (44/0), pages 512–519.

[9] F. Kossivas and A. Kyprianou. "Measurement of liquid crystal film thickness using interferometry". In: *Measurement Science and Technology* 2010 (21/10), page 105707.

[10] F. Gao, H. Muhamedsalih, and X. Jiang. "Surface and thickness measurement of a transparent film using wavelength scanning interferometry". In: *Optics Express* 2012 (20/19), pages 21451–21456. DOI: 10.1364/OE.20.021451.

[11] W. Shang and J. Chen. "A Partial Coherent Interferometry for measuring the thickness of a dynamic liquid sheet". In: *International Journal of Multiphase Flow* 2019 (116), pages 15–25.

[12] R. P. Glovnea, A. K. Forrest, A. V. Olver, and H. Spikes. "Measurement of sub-nanometer lubricant films using ultra-thin film interferometry". In: *Tribology Transactions* 1991 (34/4), pages 187–193.

[13] D. Dipresa. "Optical thin film measurement by interferometric fringe projection and fluorescence stimulated emission". PhD thesis. The University of Leeds School of Mechanical Engineering, 2013.

[14] R. Beisswanger, M. Weckerle, C. Pruss, and S. Reichelt. "Interferometric radius of curvature measurements: an environmental error treatment". In: *Optics Express* July 2022 (30/14), page 25803. DOI: 10.1364/OE.461972.

[15] S.-T. Lin and H.-Q. Le. "Common-path tandem interferometer for thin-film thickness measurements". In: *Measurement* 2023 (214), page 112780.

[16] C. Buffone, A. Glushchuk, C. S. Iorio, and F. Dubois. "Measurement of Film Thickness on a Curved Surface by Fiber Optic Probe". In: *Journal of Electronics Cooling and Thermal Control* 2013 (3), pages 22–26.

[17] S. Alekseenko, A. Bobylev, A. Evseev, V. Karsten, D. Markovich, and B. Tarasov. "Measurements of the Liquid-Film Thickness by a Fiber-

Optic Probe". In: *Instruments and Experimental Techniques* 2003 (46/2), pages 260–264.

[18] Y. W. Huang, J. Tao, and X. G. Huang. "Research Progress on F-P Interference—Based Fiber-Optic Sensors". In: *Sensors* 2016 (16/9). DOI: 10.3390/s16091424.

[19] B. Author, J. Author, J. Author, S. Author, T. Author, and J. Author. "Ultrahigh Resolution Thickness Measurement Technique Based on a Hollow Core Optical Fiber Structure". In: *Sensors* 2020 (20/7). DOI: 10.3390/s20072035.

[20] Y. Mizushima. "A New Ray-Tracing-Assisted Calibration Method of a Fiber-Optic Thickness Probe for Measuring Liquid Film Flows". In: *IEEE Transactions on Instrumentation and Measurement* 2021 (70). DOI: 10.1109/TIM.2021.3101577.

[21] T. A. Shedd and T. A. Newell. "Automated optical liquid film thickness measurement method". In: *Review of Scientific Instruments* 1998 (69/12), pages 4205–4209.

[22] M. Wang and et al. "A new method for liquid film thickness measurement based on ultrasonic echo resonance technique in gas-liquid flow". In: *Measurement* 2019 (146), pages 447–457.

[23] B. Wang, B. Ke, B. Chen, R. Li, and R. Tian. "A technical review of research progress on thin liquid film thickness measurement". In: *Journal Name* 2019 (Volume/Number), Page Range. DOI: DOI.

[24] A. Cherdantsev, A. Bobylev, V. Guzanov, A. Kvon, and S. Kharlamov. "Measuring liquid film thickness based on the brightness level of the fluorescence". In: *International Journal of Multiphase Flow* 2023 (168), page 104570. DOI: 10.1016/j.ijmultiphaseflow.2023.104570.

[25] D. C. Deisenroth. "Thickness measurement of dynamic thin liquid films generated by plug-annular flow in non-wetting microchannels". Master's thesis. Michigan Technology University, 2014.

[26] *Olympus - Life Science Solutions*. [Online]. 2023. URL: https://www.olympus-lifescience.com/en/microscope-resource/primer/lightandcolor/interference/#:~:text=Interference%20of%20light%20is%20the,to%20either%20increase%20or%20decrease.. (Accessed: 24.07.2023).

[27] P. Hariharan. *Basics of interferometry*. Elsevier Academic Press, 2007.

[28] R. Paschotta. *Interferometers*. RP Photonics Encyclopedia. Available online at https://www.rp-photonics.com/interferometers.html, url = https://www.rp-photonics.com/interferometers.html, doi = 10.61835/kva, urldate = 2024-03-27, keywords = interferometers, types, operation principle, Mach–Zehnder, Michelson, Fabry–Pérot. Feb. 2005.

[29] *Building a Mach-Zehnder Interferometer | Edmund Optics*. [Online]. 2021. URL: https://www.edmundoptics.com/knowledge-center/application-notes/optomechanics/building-a-mach-zehnder-interferometer/. (Accessed: 24.07.2023).

[30] *Michelson – Morley Interferometer*. [Online]. 2020. URL: https://physicsopenlab.org/2020/05/16/michelson-morley-interferometer/. (Accessed: 25.07.2023).

[31] *Optical Resonators and Interferometers*. [Online]. 2018. URL: https://acikders.ankara.edu.tr/mod/resource/view.php?id=101731. (Accessed: 25.07.2023).

[32] H.-y. Zhou, G.-m. Ma, Y. Wang, W.-q. Qin, J. Jiang, C. Yan, and C.-r. Li. "Optical sensing in condition monitoring of gas insulated apparatus: a review". In: *High Voltage* 2019 (4/4), pages 259–270. DOI: https://doi.org/10.1049/hve.2019.0128. eprint: https://ietresearch.onlinelibrary.wiley.com/doi/pdf/10.1049/hve.2019.0128.

[33] A. R. Bahrampour, S. Tofighi, M. Bathaee, and F. Farman. "Optical Fiber Interferometers and Their Applications". In: *Interferometry*. Edited by I. Padron. Rijeka: IntechOpen, 2012. Chapter 1. DOI: 10.5772/34346.

[34] *Fiber Optic Cable vs Twisted Pair Cable vs Coaxial Cable*. [Online]. 2021. URL: https://community.fs.com/blog/the-difference-between-fiber-optic-cable-twisted-pair-and-cable.html. (Accessed: 29.07.2023).

[35] *What is Fiber Optic?* [Online]. 2020. URL: https://telecom.samm.com/what-is-fiber-optic. (Accessed: 29.07.2023).

[36] *Single Mode vs. Multi-Mode Fiber Optic Cable*. [Online]. 2022. URL: https://www.multicominc.com/training/technical-resources/single-mode-vs-multi-mode-fiber-optic-cable/#:~:text=Single%20Mode%20fiber%20optic%20cable%20has%20a%20small%20diametral%20core,the%20signal%20to%20travel%20further.. (Accessed: 29.07.2023).

[37] A. Tolosa, N. Alcon, S. F., and O. Ruiz. "Method of determining the optical properties of ceramics and ceramic pigments : Measurement of the refractive index". In: 2011.

[38] M. Yıldırım. "Design and construction of an experimental apparatus for the interferometric measurement of micrometer level clearances". Master's thesis. Middle East Technical University, 2009.

[39] S. Maiti. *What is Six Sigma? Principles, Methodologies, Certification, PDF*. [Online]. 2021. URL: https://educationleaves.com/what-is-six-sigma-6%CF%83-principles-methodologies-certification-pdf/. (Accessed: 22.03.2024).

[40] Y. B. Erkan. "Numerical simulation of coalescence of micron-submicron sized droplets and thin films". Master's thesis. Middle East Technical University, 2021.

[41] *Does NA provide a good estimate of beam divergence from a single mode fiber?* [Online]. 2020. URL: https://www.thorlabs.com/newgrouppage9.cfm?objectgroup_id=14204. (Accessed: 29.07.2023).

[42] I. H. Malitson. “Interspecimen Comparison of the Refractive Index of Fused Silica∗,†”. In: *J. Opt. Soc. Am.* Oct. 1965 (55/10), pages 1205–1209. DOI: 10.1364/JOSA.55.001205.

[43] *Transforming Gaussian Beams into Uniform, Rectangular Intensity Distributions*. [Online]. 2012. URL: https://www.techbriefs.com/component/content/article/tb/supplements/ptb/features/articles/12683. (Accessed: 01.08.2023).

[44] R. Paschotta. *Optical Path Length*. RP Photonics Encyclopedia. Available online at https://www.rp-photonics.com/optical_path_length.html, url = https://www.rp-photonics.com/optical$_p ath_l ength.html, doi = 10.61835/2m5, urldate = 2024 − 03 − 28, keywords = opticalpathlength, opticalphase, Fermat's
May 2023.

APPENDIX A

SPECIFICATIONS OF EXPERIMENTAL DEVICES AND TOOLS

Table A.1: Specifications of the laser source [38]

Wavelength [nm]	1550
Wavelength accuracy [nm]	±20 (nominal)
Bandwidth [nm]	1.5
Optical Power [mW]	0.8—1.0 (standard)
Optical Power Stability [dB]	±0.004
Fiber Optic Cable End	FC/APC
Fiber Optic Cable Type	Single-mode
Power Source	110/220 V AC 60/50 Hz
Dimensions (W×L×H) [mm]	260×209×90
Operating Temperature Range [°C]	0 – +50
Storing Temperature Range [°C]	-40 – +70
Humidity [%]	<70

Table A.2: Specifications of the fiber optic isolator [38]

Wavelength [nm]	1550
Bandwidth [nm]	±10
Maximum Isolation [dB]	45
Minimum Isolation [dB]	40
Typical Insertion Loss [dB]	0.5
Maximum Insertion Loss [dB]	0.6
Return Loss [dB]	55
Fiber Type	Single-mode
Operating Temperature Range [°C]	0 – +70
Storing Temperature Range [°C]	-40 – +85

Table A.3: Specifications of the fiber 0ptic beam splitter [38]

Wavelength [nm]	1550
Bandwidth (nm)	±10
Maximum Isolation [dB]	45
Minimum Isolation [dB]	40
Typical Insertion Loss [dB]	0.5
Maximum Insertion Loss [dB]	0.6
Return Loss [dB]	55
Fiber Type	Single-mode
Split Ratio	1:4
Storing Temperature Range [°C]	-40 – +85

Table A.4: Specifications of the circulator [38]

Wavelength [nm]	1550
Extinction Ratio [dB]	30
Insertion Loss, Forward Direction [dB]	60
Insertion Loss, Reverse Direction [dB]	60
Peak Isolation [dB]	30
Power Handling [mW]	250
Fiber Type	Single Mode
Return Loss [dB]	60

Table A.5: Specifications of the photo detector [38]

Detector	Ge PIN
Active Area	⌀5mm(19.6 mm^2)
Surface Depth [mm]	5.1
Wavelength Range [nm]	800–1800
Peak Wavelength (λ_p) [nm]	1550
Peak Response	0.85 A/W @λ_p
Output Voltage [V]	0–10
Output Impedance [Ω]	50
Maximum Output Current [mA]	100
Load Impedance [Ω]	50
Gain Range [dB]	70
Gain Steps [dB]	8×10
Gain Switch	8 pos rotary
On/Off Button	Slide
Output	BNC
Optical Head Size [mm]	70.1×52.8×21.1
Weight [kg]	0.15

Table A.6: Specifications of the fiber optic cable [38]

Wavelength [nm]	1550
Bandwidth [nm]	±50
Length [m]	1
Outer Diameter [mm]	1.8
Inner Diameter [µm]	9/125
Fiber Type	Single-mode
Fiber Ends	FC/APC

Table A.7: Specifications of step motor [38]

Phase	2
Step Angle [°/step]	1.8±%
Inertia [gcm^2]	1600
Current [A/phase]	4.5
Resistance [Ω/phase]	0.7±10%
Inductance [mH/phase]	6.7±20%
Holding Torque [N·m]	4.5
Detent Torque	2 NCM
Insulation Class	B

APPENDIX B

COMPARISON TABLE FOR DIFFERENT HEIGHTS OF THE FOP

Table B.1: The comparison table for the height of the FOP of 3.45 mm, 3.49 mm, 3.50 mm, 3.51 mm and 3.55 mm, the height of the liquid film of twelve values equally spaced between 0.40 mm and 0.62 mm and the width of the liquid film of 5.04 mm. Additionally the simulation results covers the cases with the height of the liquid film of 0.64 mm for different probe heights.

Liquid Width [mm]	**Probe Height [mm]**	**Liquid Height [mm]**	$\mathcal{R}$ **@midpoint [mm]**	**FFT Comp. Criteria**	**MSE**	**R2**
5.04	3.45	0.40	9.526	5.631	45.023	0.478
5.04	3.45	0.42	9.110	2.784	37.075	0.570
5.04	3.45	0.44	8.733	2.158	29.825	0.654
5.04	3.45	0.46	8.391	2.518	23.518	0.727
5.04	3.45	0.48	8.080	1.205	17.989	0.791
5.04	3.45	0.50	7.795	0.953	13.250	0.846
5.04	3.45	0.52	7.534	0.968	9.405	0.891
5.04	3.45	0.54	7.295	0.734	6.004	0.930
5.04	3.45	0.56	7.074	0.576	3.540	0.959
5.04	3.45	0.58	6.871	0.734	2.029	0.976
5.04	3.45	0.60	6.682	0.513	1.209	0.986
5.04	3.45	0.62	6.508	0.364	0.882	0.990
5.04	3.45	0.64	6.347	0.542	1.849	0.979
5.04	3.49	0.40	9.526	4.730	44.337	0.486
5.04	3.49	0.42	9.110	3.331	36.620	0.575
5.04	3.49	0.44	8.733	1.783	29.497	0.658

Table B.1 continued from previous page

Liquid Width [mm]	Probe Height [mm]	Liquid Height [mm]	$\mathcal{R}$ @midpoint [mm]	FFT Comp. Criteria	MSE	R2
5.04	3.49	0.46	8.391	1.751	23.226	0.731
5.04	3.49	0.48	8.080	1.765	17.804	0.794
5.04	3.49	0.50	7.795	0.967	12.881	0.851
5.04	3.49	0.52	7.534	0.819	8.772	0.898
5.04	3.49	0.54	7.295	0.892	5.903	0.932
5.04	3.49	0.56	7.074	0.593	3.364	0.961
5.04	3.49	0.58	6.871	0.450	1.813	0.979
5.04	3.49	0.60	6.682	0.644	1.067	0.988
5.04	3.49	0.62	6.508	0.459	1.106	0.987
5.04	3.50	0.40	9.526	5.759	44.427	0.485
5.04	3.50	0.42	9.110	2.545	36.549	0.576
5.04	3.50	0.44	8.733	1.899	29.405	0.658964933
5.04	3.50	0.46	8.391	2.225	23.801	0.724
5.04	3.50	0.48	8.080	1.335	17.657	0.795
5.04	3.50	0.50	7.795	0.969	12.735	0.852
5.04	3.50	0.52	7.534	1.080	8.879	0.897
5.04	3.50	0.54	7.295	0.752	5.746	0.933
5.04	3.50	0.56	7.074	0.504	3.320	0.961
5.04	3.50	0.58	6.871	0.477	30.115	0.651
5.04	3.50	0.60	6.682	0.531	0.970	0.989
5.04	3.50	0.62	6.508	0.426	1.057	0.988
5.04	3.50	0.64	6.346	0.606	1.924	0.978
5.04	3.51	0.40	9.526	3.787	44.331	0.486
5.04	3.51	0.42	9.110	2.395	36.430	0.577
5.04	3.51	0.44	8.733	2.181	29.260	0.661
5.04	3.51	0.46	8.391	2.004	23.176	0.731
5.04	3.51	0.48	8.080	1.171	17.534	0.797
5.04	3.51	0.50	7.795	1.138	12.573	0.854
5.04	3.51	0.52	7.534	0.927	8.785	0.898
5.04	3.51	0.54	7.295	0.589	5.667	0.934
5.04	3.51	0.56	7.074	0.521	3.561	0.960
5.04	3.51	0.58	6.871	0.672	1.915	0.978

Table B.1 continued from previous page

Liquid Width [mm]	Probe Height [mm]	Liquid Height [mm]	$\mathcal{R}$ @midpoint [mm]	FFT Comp. Criteria	MSE	R2
5.04	3.51	0.60	6.682	0.492	0.941	0.989
5.04	3.51	0.62	6.508	0.429	1.195	0.986
5.04	3.51	0.64	6.347	0.502	1.936	0.978
5.04	3.55	0.40	9.526	5.528	44.074	0.489
5.04	3.55	0.42	9.110	2.832	36.106	0.581
5.04	3.55	0.44	8.733	1.839	28.917	0.666
5.04	3.55	0.46	8.391	2.295	22.581	0.738
5.04	3.55	0.48	8.080	1.230	17.125	0.801
5.04	3.55	0.50	7.795	0.892	12.383	0.856
5.04	3.55	0.52	7.534	0.839	8.514	0.901
5.04	3.55	0.54	7.295	0.777	5.446	0.936
5.04	3.55	0.56	7.074	0.569	3.070	0.964
5.04	3.55	0.58	6.87	0.597	1.645	0.9814
5.04	3.55	0.60	6.682	0.507	1.187	0.986
5.04	3.55	0.62	6.508	0.405	1.034	0.988

CURRICULUM VITAE

PERSONAL INFORMATION

Surname, Name: Ağartan, Yiğit Ata
Nationality: Turkish (TC)

EDUCATION

Degree	Institution	Year of Graduation
M.Sc.	METU Mechanical Engineering	2012
B.Sc.	METU Mechanical Engineering	2009
High School	Isparta Süleyman Demirel Science High School	2004

PROFESSIONAL EXPERIENCE

Year	Place	Enrollment
2009-2012	METU Mech.Eng.Dept., Ankara	Research Assistant
2012-Present	ASELSAN Inc., Ankara	Senior Lead Engineer